Development of a Fatigue Testing System for CFRP Under Combined Cyclic and Impact Load

By:

Christian Bärnthaler

Department Product Engineering
University of Leoben
A-8700 Leoben
Austria

Supervisor:
Univ.-Prof. Dipl-Ing. Dr.mont. Florian Grün
Dipl.-Ing. Andreas Mösenbacher
Dipl.-Ing. ETH Lukas Weiss

February 2015

Eidesstattliche Erklärung

Ich erkläre an Eides statt, dass ich diese Arbeit selbstständing verfasst, andere als die angegebenen Quellen und Hilfsmittel nicht benutzt und mich auch sonst keiner unerlaubten Hilfsmittel bedient habe.

Affidavit

I declare in lieu of oath, that I wrote this thesis and performed the associated research myself, using only literature cited in this volume.

(Datum) (Christian Bärnthaler)

Abstract

The working speed of stamping machines or similar devices is often not high enough. To increase the working speed of high speed stamping machines, it is necessary to reduce the masses of the moving parts. Due to their high stiffness and strength, carbon fibre reinforced composites seem to be ideal for this application. Typically the components are used for 20 000 h of operation. To validate the material's fatigue strength for up to 1.5×10^9 cycles, a suitable testing facility is designed. Various problems like a high testing frequency, heating of the specimen and an accurate measuring system have to be considered. In the end a high frequency testing machine is designed and put into action. The functionality of the testing device is examined and reported.

Contents

Chapter 1

Introduction

Stamping presses generate, depending on various process parameters, very high forces. The tool is mounted to the ram, which is an important element to ensure the quality and stability of the process. High stiffness as well as excellent fatigue resistance of the ram is demanded. Additional mass forces and the required high accuracy make building high speed presses and stamping machines extremely challenging.
Applying Carbon Fibre Reinforced Plastics (CFRPs) as a material for machine tooling is a suitable concept since the weight saving is remarkable and the reachable stiffness is adequately high. However, the fatigue behaviour of these materials under such specific loads is an important issue especially considering such a large number of cycles. To guarantee best quality through the whole life of the machine, tests must be executed to evaluate the functionality of CFRP as a usable material in machine building. The specific machine examined is the BRUDERER® BSTA 200 with a nominal force of 200 kN. During its lifetime of 20 000 h the ram must withstand up to 3×10^9 loading cycles. The aim of this thesis is to investigate the occurring stresses during operation in the ram. With this information a suitable testing machine will be designed which can both adequately represent the loads and reach a high number of cycles in a reasonable amount of time.

1.1 Problem Definition

A major concern in applying CFRP in machine tools is the fatigue behaviour and the change in material properties with increasing stress cycles. Depending on the arrangement of fibres and matrix system the material shows different behaviours. A typical stiffness drop of approximately $10 - 30\,\%$ at the beginning of the life span of CFRP has to be considered as well as the particular reactions of different material systems on strain rates [1] [2]. This is the reason the characteristics of CFRP and its answer to distinctive loadings has to be studied and understood. The specific challenge when examining the material's behaviour lies in the specific load conditions and the high number of cycles. To test up to 3×10^9 cycles an usual servo hydraulic testing machine would need over three years at 30 Hz. Therefore, the testing machine has to be able to test at high frequencies to reduce the testing time to a reasonable limit. High testing frequencies on the other hand comport various problems such as overheating of the specimen or the exciting system, material dependency on strain rates and fatigue life of the testing facility itself. Due to the complex material behaviour of CFRP, it is important to represent the crucial damage mechanisms in the testing stand.

1.2 Aim

The aim of this thesis is to develop a suitable method to test CFRP for its fatigue behaviour for this specific load case. To begin with, a fundamental research of the fatigue and impact behaviour of this material has to be conducted to understand the occurring damage mechanisms and represent them in a test. Furthermore, the load case and its characteristics will be examined closely. In the end a testing machine should be presented which is able to reproduce those damage mechanisms and reduce the testing time compared to an ordinary fatigue testing device significantly. Furthermore the testing device will be put in operation and its quality and functionality validated. The testing device concluding its measuring system should be compared to the results from the preliminary simulations.

Chapter 2

Fundamentals: Material Properties of Carbon Fibre Reinforced Composites (CFRP)

In this section the state of the art regarding material properties and behaviour of CFRPs will be discussed and examined. This is a crucial part of the thesis, for it is important to understand the behaviour of the tested material to produce repeatable and valuable results. The decisive mechanisms are reviewed to recreate the actual loading conditions in a justifiable and simple way. This thesis deals with the mechanical behaviour of CFRP when exposed to a high number of stress cycles and impacts. This section shall give an overview of the behaviour of CFRP under fatigue and impact like loadings and address the characteristics which have to be considered particularly. In the examined case, more precisely, the applied component should withstand cyclic loads up to the very high cycle fatigue (VHCF) regime which begins at approximately 10^7 cycles. Usually the results are represented in a S\N diagram where the bearable cycles in a logarithmic scale are plotted over the according stress. A typical S\N curve for a carbon fibre composite with a thermoplastic matrix according to Michel et al. is shown in figure 2.1. [3]

It is shown for various materials that they do not have an unlimited fatigue strength. The fatigue over circa 1×10^9 cycles is usually limited by failures which are initiated in the interior of the material [4]. Compared to metallic materials, fibre reinforced materials generally show a much better fatigue behaviour. However, the investigations of fatigue behaviour continues to be a crucial factor and the mechanisms which underlay the failure are numerous and complicated. The fatigue strength for CFRP is well known for up to 2×10^6 cycles, namely the high cycle fatigue (HCF), for various loading conditions [4] [5].
To acquire a general understanding of the problems and damages which can occur in CFRP, this section will work through different damage mechanisms and give an overview of the typical material properties. This shall help to decide whether or not it is necessary to reproduce the cyclic load in combination with the impact load. When applying CFRP for rams in stamping machines it has to withstand very high loading cycles, relatively high strain rates and compression- as well as tension stresses [6].
The mechanisms in composites which stand behind the high cycle fatigue are generally more complex than in homogeneous materials. Each geometrical arrangement of fibres and matrix can be seen as a new material and with that, the damage mechanisms vary [7]. Unidirectional composites

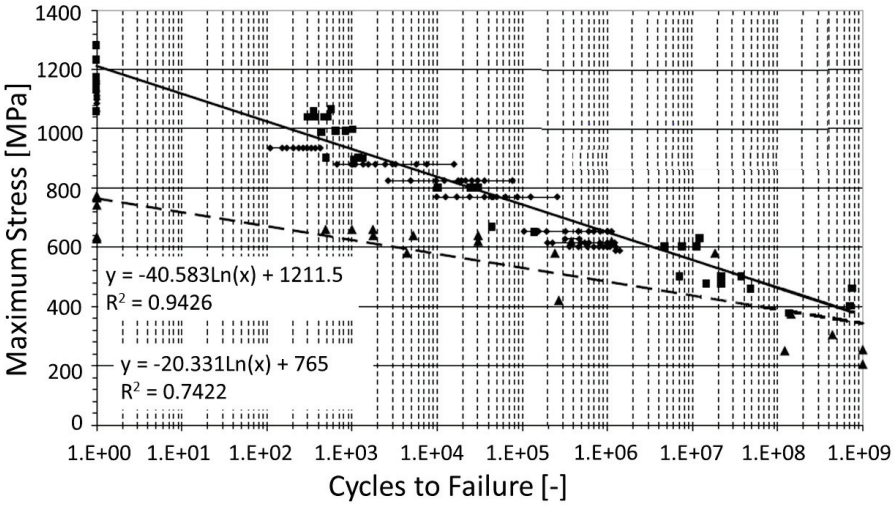

Figure 2.1: S\N curve for CFRP up to the gigacycle regime [3]

generally behave in a brittle and linear manner under load and show sudden failures without prior indications when loaded in fibre direction. The investigation of the behaviour of these materials under fatigue loading is therefore a noteworthy issue in order to make general statements about the safe application of composite structures.
Fibre reinforced composites consist basically of fibres, matrix and the interphase region, which is responsible for the bonding between fibre and matrix. Therefore the active damage mechanism largely depends on those three components and their mechanical and chemical properties [8].
Furthermore there are various forms of fibres which are used in composites. In this thesis though, the main focus will stay on unidirectional endless fibres. When speaking of fibres, one dimension of the fibre is at least one order larger than the others which results in long thin cylinders [9].

2.1 Material Properties

Basically composites are material combinations which intend to combine the different material properties in an optimal way. Usually the fibre has a diameter between 5 µm and 200 µm [10]. A typical CFRP composite can be described as following [9]:

- A reinforcing fibre is embedded in a continuous matrix.
- The fibre and the matrix are initially two separate materials which are then united.
- The size of the reinforcing fibre is approximately a few micrometers.
- The reinforcing fibre takes up more than 10 % in volume of the composite.

The appropriate combination of matrix and fibre largely depends on the ambient conditions, the occurring stresses and the intended use. E.g. considering an endless fibre reinforced composite, the forces are usually not induced directly into the fibres but are brought by the matrix into the fibre. This means that the connection between the matrix and the fibres is responsible for the transfer

of the stresses from the matrix into the much stiffer fibre and is therefore a significant parameter. Due to the remarkable difference in stiffness of the matrix and the fibre, the strain of the matrix is generally larger in the regions in front and behind of the fibres than lateral to the fibre. This means that the strain in the matrix can locally be significantly larger than the global strain. [9].

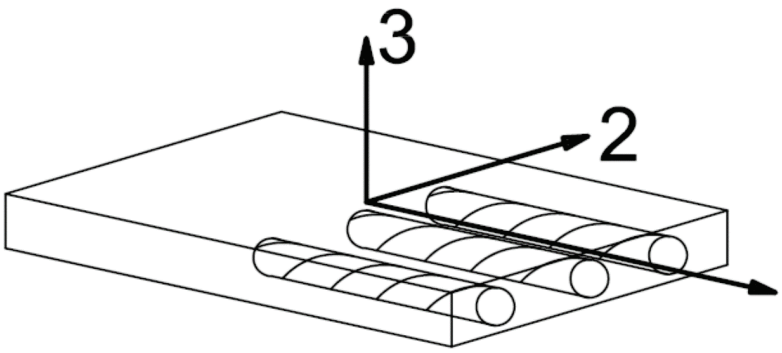

Figure 2.2: Schematic unidirectional layer of a composite

2.1.1 Material Compositions and their Properties

Normally materials like metals, polymers or ceramics are isotropic, at least in a global sense. Fibre reinforced materials are either:

- Homogeneously orthotropic
- Homogeneously an-isotropic
- Heterogeneous orthotropic
- Heterogeneous an-isotropic
- Quasi isotropic

Orthotropic is a combination of orthogonal and isotropic. A homogeneous material has the same properties in every point and direction [10]. The material properties are independent of location and orientation. An orthotropic material has three symmetrical planes regarding material properties. And an-isotropic material has no symmetrical planes at all [10]. This means that the material properties change with alteration of the coordinate system in an orthotropic or an-isotropic material. In figure 2.2 an unidirectional layer of a composite is shown which is an orthotropic material system. A fibre reinforced material is usually built up of several layers in a surrounding matrix. These layers are called tapes. Figure 2.3a shows an unidirectional composite built up of several layers. The tapes are layered in one direction and the material is therefore also an orthotropic material system. 0° thereby means the fibre orientation is along the loading direction, whereas 90° is in transverse direction to the fibres.

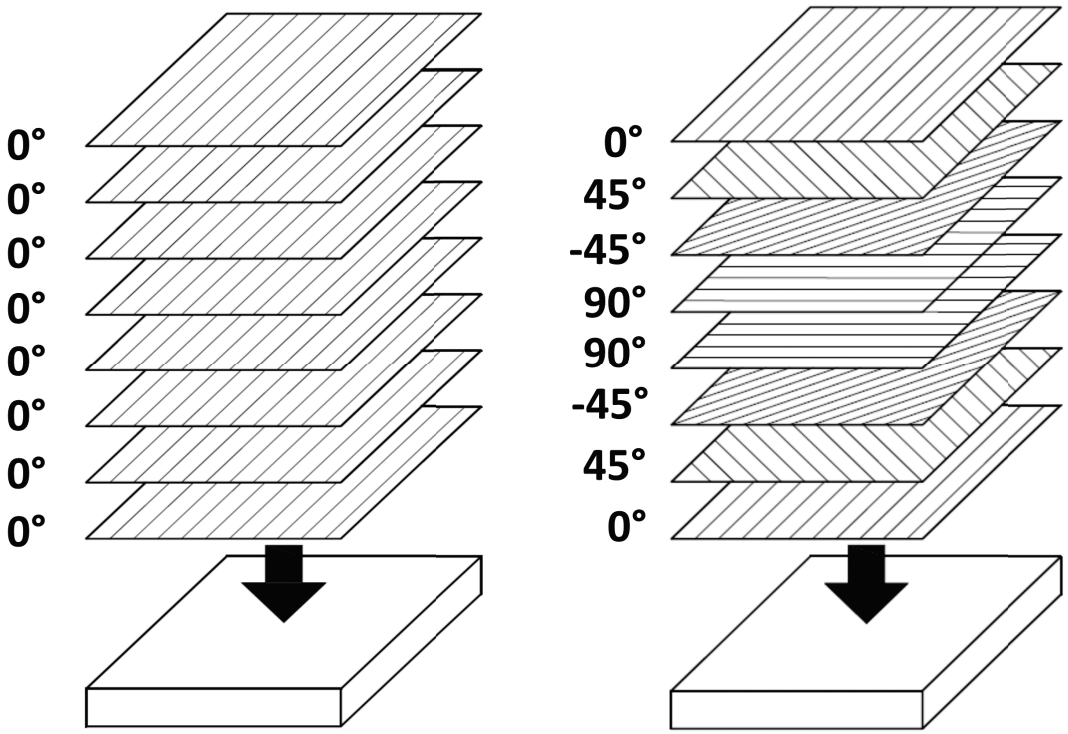

(a) Unidirectional Composite (b) Multidirectional Composite

Figure 2.3: Schematic composites consisting of several layers

On the contrary, the tapes of a multi-directional composite are layered in different directions as seen in figure 2.3b. This indicated composite is layered in a way so that a quasi isotropic material system is generated [10].

The most important characteristic parameters of a fibre reinforced composite are ultimate uniaxial longitudinal, and transverse tensile and compressive strength, ultimate uniaxial in-plane shear strength, and ultimate strains in the longitudinal, transverse and shear direction. Furthermore the uniaxial tensile and compressive moduli in the longitudinal and transverse directions, in-plane shear modulus and Poisson's ratios are required for characterizing the material. Therefore more than one test with different specimens has to be carried out to fully specify the mechanical material behaviour of a composite lamina [11].

2.1.2 Visco-Elasticity

Fibre reinforced plastics can develop a significant visco-elastic behaviour due to their polymeric matrix. These effects not only depend on the type of material but also on the environmental circumstances like humidity, temperature and frequency. The visco-elastic effect describes the behaviour of materials with time-dependency and memory effects. This means that the response of a visco-elastic material on a certain amount of stress, not only depends on the current applied stress, but is also determined by all past states of stresses [12]. Figure 2.4 shows a strain stress development of a visco-elastic material. The phase lag implies a dependency of the velocity in the stress-strain relation [13]. The relation between loss factor η and phase lag ϕ is stated in equation (2.1). Furthermore this behaviour can be described with equation (2.2) where E is the

Young's modulus and η is the loss factor. The storage moduli G' and E', shear modulus and young's modulus respectively, are representatives for the stiffness of the material and G'' and E'' are a criterion for the dissipated energy which is not transformed into elastic strain energy and are therefore called loss moduli.

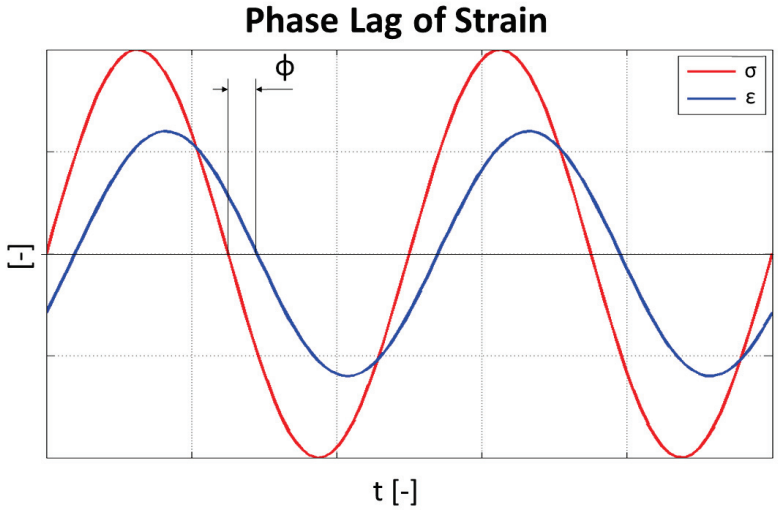

Figure 2.4: Harmonic excitation and strain response of a visco-elastic solid

$$\eta = \tan\phi \tag{2.1}$$

$$\sigma = E\varepsilon + \frac{E\eta}{|\omega|}\frac{d\varepsilon(t)}{dt} \tag{2.2}$$

Usually the complex version of equation (2.2) is used for easier handling and is shown in equation (2.3) where E^* is the complex modulus. Equation (2.3) describes the representation on the basis of storage- and loss moduli E' and E'' respectively. The same can be said for shear stresses and strains with G' and G'' [13].

$$E^* = E' + E'' = E(1 + i\eta) \tag{2.3}$$

The storage and the loss modulus can also be measured indirectly by strain, stress and phase lag. The equation stated in (2.4) for the storage modulus and in (2.5) for the loss modulus [14].

$$E' = \frac{\sigma_0}{\varepsilon_0}\cos\phi \tag{2.4}$$

$$E'' = \frac{\sigma_0}{\varepsilon_0}\sin\phi \tag{2.5}$$

The energy loss per cycle and per unit volume ΔE is given by equation (2.6) [15]. The loss factor η is defined as in equation (2.7). It has to be mentioned that the loss factor for shear strain is generally not equal but with usually small and unmeasurable differences [13]. The loss factor as defined in

equation (2.7) is according to various authors the most suitable index. Another representation of the loss factor is energy based and stated in equation (2.13).

$$\Delta E = \int_0^{\frac{2\pi}{\omega}} \sigma_{(t)}\, d\varepsilon_{(t)} = \pi E'' \varepsilon_0^2 \tag{2.6}$$

$$\eta = \frac{E''}{E'} \tag{2.7}$$

2.1.2.1 Effect of Frequency on Visco-Elastic Behaviour

The frequency dependency of the storage modulus E' and the loss modulus E'' can be divided into three regions as seen in figure 2.5. The three regions are called rubbery region, transition region and glassy region. The smallest loss factors are found in the rubbery region and the glassy region and a maximum is found in the transition region. The storage modulus increases steadily in the rubbery region and then rises steeply in the transition region to a maximum [16] [13]. The frequency is plotted in a logarithmic scale. This means that the frequency dependency is not very strong. To avoid heating, the desired working region for fatigue testing would be the glassy region. In this region most of the energy is converted into strain energy and only a small part into lost energy like heat. This region, however, depends on the chosen material system as well as fibre orientation and content.

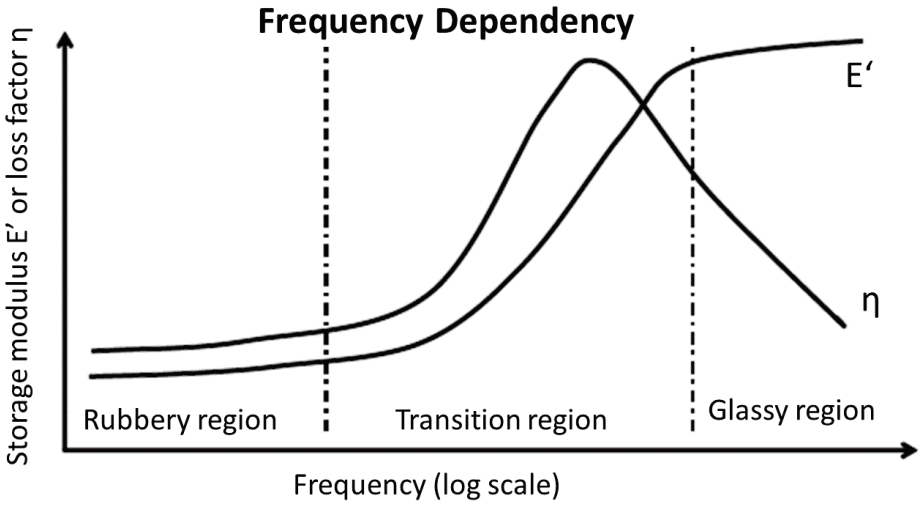

Figure 2.5: Storage modulus and loss factor versus frequency[16]

2.1.3 Damping

For various reasons the effects of damping have to be examined in this thesis. Damping is responsible for heating of the specimen under stresses. This process has to be well understood to predict overheating and to adjust the system correctly. Furthermore the required forces from the actuator

in a resonant system strongly depend on the damping. To achieve a certain stress or strain in the specimen, a stronger damped system needs more force to get excited adequately.

Damping is an energy absorbing mechanism and influences the behaviour of materials crucially. The absorbed vibration energy is transformed into another form of energy like heat in the case of visco-elastic damping. Especially when working with polymers and at high frequencies and loading velocities the damping has to be understood and taken into consideration [17]. The energy dissipation alters the vibrational properties of the system. The mode shapes will be altered referring to the undamped system [18]. However, it has been shown, that the damping of CFRP or GFRP is not particularly dependent on frequency nor temperature except near the glass transition temperature. Damping can be a desired process for example in automotive applications where damping reduces noise and conveys a smoother handling. In other applications damping can lead to serious overheating and should therefore be avoided [13] [19].

In composites, different damping mechanisms are effective compared to metals. The observed causes for the energy dissipation are according to [17] [13] following:

Visco-elastic nature of matrix and/or fibre materials: The matrix is the main component responsible for damping. Compared to other fibre systems, carbon and kevlar fibres have considerable damping properties. The viscous properties of composite materials imply a time dependent behaviour and enable the material to dissipate energy.

Damping due to interphase: The interphase region represents the adjacent surface to the fibre. This region has a considerable thickness and its properties differ from the particular properties of the fibre and the matrix. Depending on the nature of the interphase, the material properties and hence the damping is affected. The energy dissipation originates from the high shear strain in the interphase region.

Damping due to damage: Generally there are two events. One is called frictional damping and origins from the unbound regions between fibre and matrix or delaminations. The other type is caused by the energy dissipation in the regions of matrix cracks, broken fibres etc. This means that the damping capacity can be also used to determine damages.

Visco-plastic damping: Non-linear damping is caused by large amplitudes of vibration respectively high stresses. This problem occurs especially with thermoplastic composite materials. The determination of the damping is important to make appropriate estimations of the resulting displacement amplitude and to assess the heating effects. The analytical prediction of the damping is a complex issue. Adams and Bacon in [20] developed the specific damping capacity (SDC) which describes the damping properties of unidirectional composites. The specific damping capacity ψ is defined as the ratio of the dissipated energy during a cycle ΔU to the maximum strain energy U as stated in equation (2.8) [20]. The theoretical method found good experimental agreement and was approved by various authors [21][22][23].

$$\psi = \frac{\Delta U_x}{U} + \frac{\Delta U_y}{U} + \frac{\Delta U_z}{U} \tag{2.8}$$

2.1.3.1 Damping models

The easiest way to describe a dissipation of energy in a vibrational system is using an ideal viscous damper. The damping force F_d is thereby proportional to the velocity $\dot{x}_{(t)}$ [24]:

$$F_d = d\,\dot{x}_{(t)} \tag{2.9}$$

Where d is the coefficient of proportionality and is known as the viscous damping constant. A system is called linearly damped system if such a force is acting. The generated force is orientated against the direction of movement which means that the work of this force is negative and decreases the mechanical energy in the system. The differential equation for a damped oscillator, as shown in figure 2.11, is given in equation (2.10) where m is the oscillating mass and d and c are the damping factor and the spring stiffness respectively [25].

$$m\,\frac{d^2x}{dt^2} + d\,\frac{dx}{dt} + c\,x = 0 \tag{2.10}$$

This differential equation has for any damping factor a closed solution. Finally there are three cases of damping to distinguish which are easier represented using the damping ratio or damping coefficient ζ which is stated in equation (2.11). Figure 2.6 shows the effect of different damping ratios on a simple one mass oscillator. The damping ratio generates critical damping at $\zeta = 1.0$,

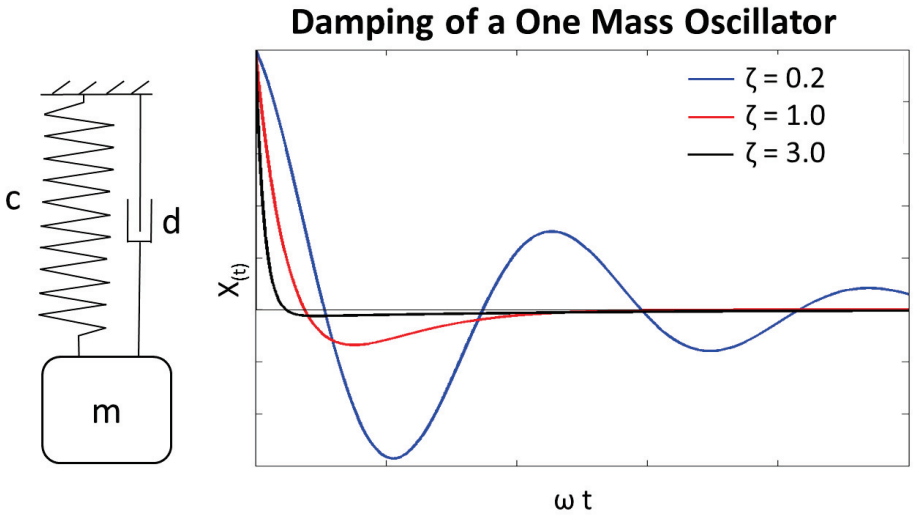

Figure 2.6: Effect of the damping ratio ζ on a one mass spring system

which means that the amplitude peak at the resonant frequency disappears. Overcritical damping takes places at values of $\zeta > 1.0$, sub critical damping at $\zeta < 1.0$ [26].

$$\zeta = \frac{d}{2\sqrt{cm}} \tag{2.11}$$

The damping ratio and the coefficient of proportionality can be related as stated in equation (2.12), where ω_n is the natural frequency and m is the mass of the system. This index is defined for a single degree of freedom system [27].

$$2\zeta\omega_n = \frac{d}{m} \tag{2.12}$$

Further the loss factor, as already mentioned in equation (2.7), is also an expression for damping and equals the energy dissipation per radian divided by the peak potential energy in the cycle and can be written as in equation (2.13).

$$\eta = \frac{D}{2\pi W} \tag{2.13}$$

where D is the energy dissipated per cycle and W stands for the energy associated to vibration. The loss factor can be applied for non linear systems. W is a term which is only defined for lightly damped systems if the total energy does not vary significantly during a cycle. For light damping ($\eta < 0.1$) the vibrational energy can be written as stated in equation (2.14) [27]:

$$W = \frac{1}{2}cX_0^2 \tag{2.14}$$

Where c is the stiffness of the system and X_0 is the oscillating amplitude. Another useful relationship is stated in equation (2.15). It is important to point out that this relation is only an approximation and applicable for $\eta << 1$ [27].

$$\eta = 2\zeta \tag{2.15}$$

The loss factor η mainly depends on the matrix system and the fibre direction and generally shows smaller values for epoxy resins and the highest values for thermoplastic matrices. Generally the damping decreases with better bonding properties of the fibre-matrix interphase [28]. In [29] a PEEK matrix showed a loss factor ranging between $10^{-4} < \eta < 5.0E-3$, where the 0° tests showed the smallest values and the 90° tests the highest damping. However, it has to be mentioned that these tests were carried out up to 120 Hz and at room temperature. Usually Dynamic Mechanical Analysis (DMA) are used to obtain the thermo-mechanical behaviour of visco elastic materials but also the frequency dependency on damping and stiffness can be observed [30].

2.1.3.2 Heating Due to Damping

As described in the sections above, visco-elastic behaviour and damping causes a loss of energy which is mainly transformed into heat. When testing at high frequencies this is a major concern since CFRP is strongly temperature sensitive and should not exceed a rise of 10 °C according to the standard ASTM D3039 [31] as mentioned in chapter 2.2.6.
The mechanical properties and the thermal properties of CFRP are anisotropic, which influence the fracture mechanisms due to the residual thermal stresses [15]. Adam et al. [33] reported the appearance of hot spots on the specimen's surface as the damage in the specimen increased.
An important part to consider is therefore the temperature rise in the specimen and how it can be influenced or predicted. Infrared sensors are used to measure the surface temperature of the specimen constantly, however the temperature throughout the specimen can not be measured. To be able to make predictions or simulations of the thermal behaviour under testing environment it is crucial to understand the damping properties of CFRP.
To determine the loss modulus of a certain material, a DMA is made. This is a test where a specimen coupon is excited with a sinusoidal force over the desired frequency range. Force, elongation and

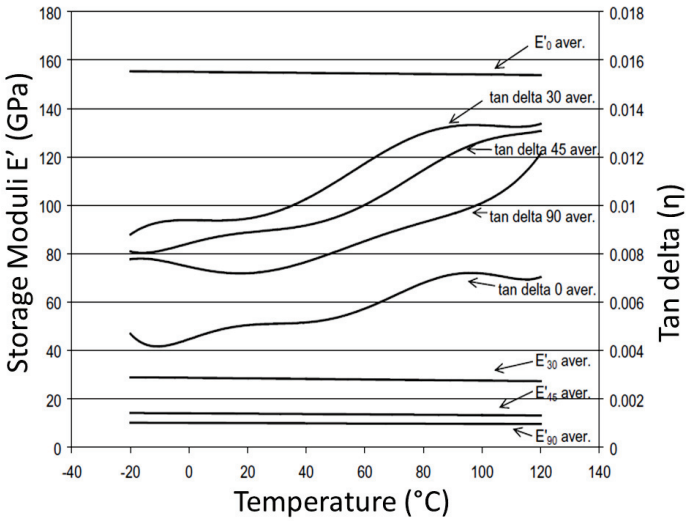

Figure 2.7: Average storage modulus and loss factor for unidirectional beams [32]

phase shift are recorded as a function of temperature or time [14]. Melo et al. [32] executed for unidirectional CFRP beams with a PEEK matrix DMAs over the typical applied temperature range. In figure 2.7 the measured average storage modulus E' and loss factor $\tan\delta$ are represented in function of the temperature. Generally for all fibre directions an increase in loss factor and a decrease in storage modulus with increasing temperature is observed. He also reported a general decrease of the loss factor with increasing frequency. However, the diagram shown in figure 2.8 is in logarithmic scale for the frequency and only shows the loss factor up to 10 Hz. The storage modulus for this frequency range was found to be practically constant.
In [34] Kishi et al. examined unidirectional CFRP with an epoxy resin. The damping properties were derived using the mechanical impedance method, in which the specimen is excited in its center. In figure 2.9 the dependency of the loss factor on the frequency is shown for different fibre directions. The damping properties behave quasi constant over the shown frequency range. As expected, the epoxy matrix generally shows smaller loss factors. This is due to the chemical structure. Also the highest damping properties are found under 45° fibre loading and can be attributed to the internal friction losses between matrix and fibre. Generally the loss factors for most CFRP systems do not exceed $\eta = 0.01$. Depending on temperature and applied frequency the loss factor can increase up to $\eta = 0.05$.
The resulting internal heat generation $\dot{q}$ is stated in equation (2.16) and increases with the frequency f and with the square of the applied strain ε_0. ΔE stands for the dissipated energy due to the loss factor E''. This leads to the conclusion that the temperature change in the specimen may be significant at high testing frequencies and must therefore be treated carefully.

$$\dot{q} = \pi E'' \varepsilon_0^2 f = \Delta E\, f \tag{2.16}$$

2.1.3.3 Temperature Distribution in the Specimen

Another problem is that temperature measurements can only be taken on the specimen's surface. However, depending on the thermal conductivities and the geometrical dimensions of the speci-

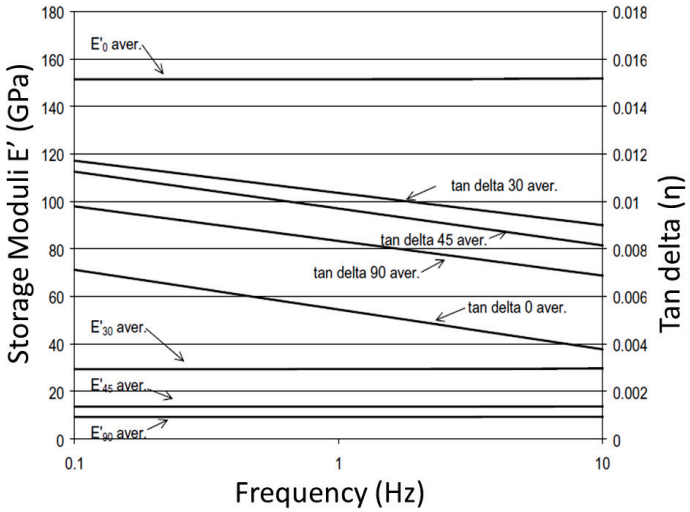

Figure 2.8: Loss factor in function of the frequency [32]

men, the core temperature can substantially differ from the surface temperature. Hosoi et al. [15] predicted the temperature distribution in coupon specimens using an one-dimensional steady state heat conduction equation. Additionally the thermal properties were assumed to be isotropic. According to [15], these assumptions can be made for a specimen which is adequately long and wide compared to its thickness.

The thermal distribution inside a coupon specimen can be calculated using the heat conduction equation for orthotropic materials in a Cartesian coordinate system represented in equation (2.17). Assumed that the thermal conductivities in the respective directions λ_1, λ_2 and λ_3 are constant.

$$\lambda_1 \frac{\delta^2 T}{\delta x^2} + \lambda_2 \frac{\delta^2 T}{\delta y^2} + \lambda_3 \frac{\delta^2 T}{\delta z^2} + \dot{q} = 0 \tag{2.17}$$

2.2 Fatigue and Damage Mechanisms

Fatigue damage and failure are a result of repetitive loading leading to degradation of the material properties due to various effects like micro damage or macro crack propagation [2]. First fatigue testing on fibre reinforced polymers with tension alternating loading resulted in S\N curves with a high endurance strength. However, further investigations showed that these composites are more damageable under compression [10]. Fatigue in fibre reinforced plastics is mostly influenced by local effects mainly at the bonding surface between fibre and matrix. Various imperfections like cracks, cavities, delaminations, fibre breakage or embedded foreign particles e.g. fats, dust, paper leftovers can cause damage or losses in stiffness. The start of the damage and the occurring mechanisms are mainly dependent on the ratio of failure strain of fibre and matrix. [10].
Generally it can be said that the fatigue resistance of the composite is higher than of the separate matrix material for loading in fibre direction. Assuming a higher stiffness of the fibre, the matrix is less loaded which results in a higher fatigue strength when loaded stress controlled [9]. This can even lower the thermal stresses especially in fibre direction due to their high conductivity. When using a strain controlled mode, the higher stiffness of the fibre increases the stresses which might

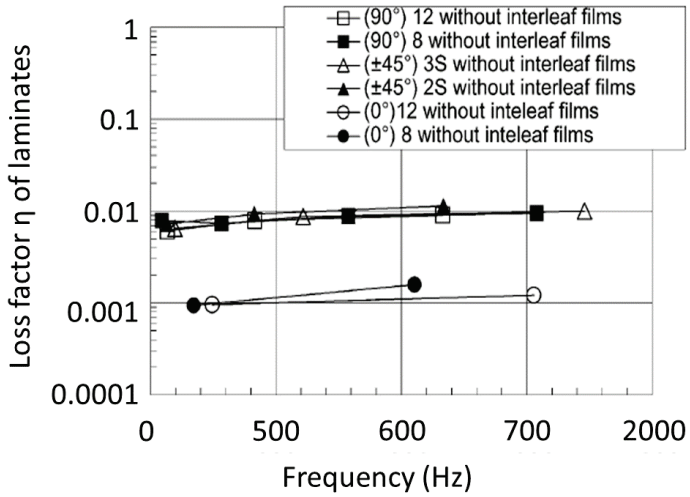

Figure 2.9: Loss factor in function of the frequency [34]

lower the fatigue strength of the composite [35]. Normally fatigue can result in change of the material properties like stiffness, strength or in worst case in fracture [36].
In reality the stresses vary in a more or less complex way. This would lead to complicated systems to reproduce these exact cases. For this reason representative cycles are chosen to fit the real case [9]. E.g. sinusoidal or triangle tests are shown in figure 2.10.

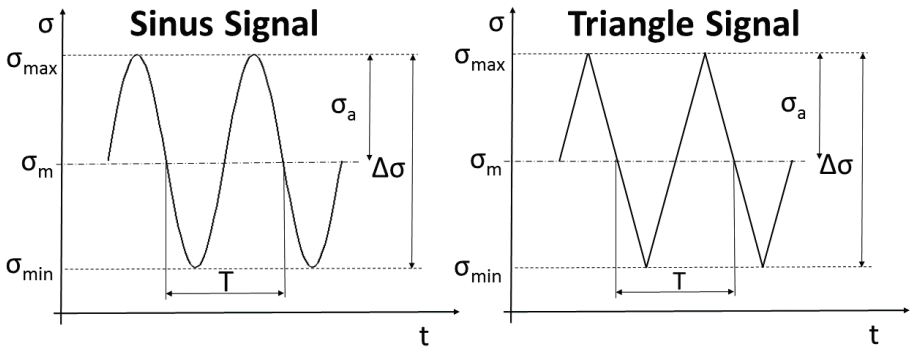

Figure 2.10: Signal of sinusoidal and triangle loading for example in fatigue tests

The representing parameters which can be seen in the diagram are the maximum and minimum stresses, amplitude and the mean value of the stress, expressed in formulas (2.18) and (2.19):

$$\sigma_m = \frac{\sigma_{max} + \sigma_{min}}{2} \tag{2.18}$$

$$\sigma_a = \frac{\sigma_{max} - \sigma_{min}}{2} \tag{2.19}$$

Further important parameters are the stress range, the stress ratio and the applied frequency expressed in formula (2.20), (2.21) and (2.22).

$$\Delta\sigma = \sigma_{max} - \sigma_{min} \tag{2.20}$$

$$R = \frac{\sigma_{min}}{\sigma_{max}} \tag{2.21}$$

$$f = \frac{1}{T} \tag{2.22}$$

The stress ratio R indicates how the specimen is loaded i.e. if only tension or compression appears or both [9]. The load case is determined with at least two parameters, e.g.:

- σ_a and R
- σ_a and σ_m
- σ_{max} and σ_{min}

The listed parameters apply for stress based testing. The analogous parameters are used for strain based testing. In this thesis the fatigue strength of CFRP shall be tested well into the very high cycle fatigue, i.e. up to $1.5 * 10^9$. Fatigue data is usually evaluated on a S\N curve. According to [36] these diagrams do not represent the multitude of the effective damage mechanism for composites. Therefore a good approach of representing a fatigue diagram of CFRP is presented by Talreja [7], called fatigue life diagram. The diagram shows the peak strain of a constant-amplitude load-controlled test against number of cycles until failure. According to Talreja there are three distinguished regions based on the occurring damage mechanism. In figure 2.11 these regions are displayed.

Region I in this diagram shows that with relatively high loads a horizontal scatter is derived. In this region the failure is due to static forces. Region II corresponds with the fatigue life of the composite and begins with a descending behaviour. According to [7] the progressive underlying mechanism for this region are fibre bridged matrix cracking and fibre/matrix debonding [7]. In Region III the mechanism of the very high cycle fatigue regime begins.

2.2.1 Mechanisms of Damage

In this section the fatigue damages which occur in CFRP due to cyclic stress will be observed. Various influences like the heterogeneous micro structure, the large difference between constituent properties, the presence of interfaces and the directionality of the reinforcement determine the characteristics of the induced damage [37]. The damage mechanisms described from various authors are:

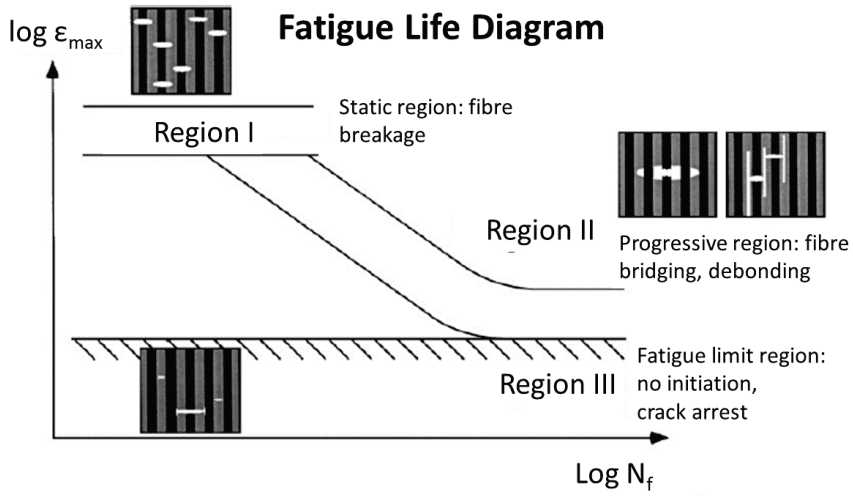

Figure 2.11: Fatigue diagram by Talreja [7]

Interfacial Debonding: As already mentioned, one of the most crucial parameters in fatigue manners for CFRPs are the properties of the interface between fibre and matrix. A crack is induced into the composite at low stresses, if the interfacial bond is weak. A stronger bonding delays crack growth and eventually a catastrophic failure occurs due to fibre breakage. The debonding occurs at the interface between fibre and matrix. Longitudinal interfacial debonding results in fibre pull-out [37]. Assuming a higher fracture strain of the fibre than the matrix, a growing crack is either halted by the fibre or it passes around the fibre without destroying the interfacial bond. With increasing load, local stresses appear in the matrix due to various deformations of the fibre and the matrix which finally results in debonding [37].

Matrix Microcracking / Intralaminar Cracking: As commonly known, fibre reinforced plastics (FRPs) have high strength and stiffness in fibre direction but have lower strength and stiffness in the transverse direction. This may result in cracks along the fibres. These cracks can be observed early in the fatigue process. Tensile loading, fatigue loading or thermal loading are typical causes for these types of cracks. The usual origins are fibre/matrix debonds or defects from manufacturing. Matrix cracking eventually leads to significant degradation of stiffness and is responsible for the initiation of several other damage mechanisms like delamination and fibre breakage [37].

Interfacial Sliding: This effect origins from the differential displacement of composite constituents. This is typical for composite systems where the fibres and the matrix are bonded through shrinking. Under thermo-mechanical loading the shrink-fit is reversed which leads to a relative displacement of fibre and matrix [37].

Delamination / Interlaminar Cracking: The separation of plies is caused by cracking in the interfacial plane of two neighbouring laminates. This effect is often observed at cut free edges, e.g. holes or an exposed surface through the thickness. The cracks are caused by normal and shear stresses which are induced at the traction free surface. It is also a typical result of low

velocity impact. The consequences of growing delamination cracks due to external loads lead to a rapid degradation of mechanical properties and can result in a catastrophic failure. The properties mainly determine the resistance against delamination [37].

Fibre Breakage: Fibre breakage is finally responsible for the ultimate failure. When a single fibre breaks at its weakest point, loaded tensionally in fibre direction, it also affects the fibres in close proximity. The stresses which were carried by the broken fibre are transferred to the adjacent fibres, eventually generating stress peaks at certain points. This process is of statistical nature. Cracks generate an increase of stress on the fibres, causing them to break [37].

Fibre Micro Buckling: This effect is a result of compressive loading of unidirectional composites. Two idealized modes are distinguished, namely extensional and shear modes, depending on whether the fibres are bent in or out of phase [37].

Void Growth: Voids are defects in the matrix induced by manufacturing. Vacuum pressure, cure temperature, cure pressure and resin viscosity amongst others affect the formation of voids. Flexural, transverse and shear properties are significantly affected by the presence of voids. However, the influence of voids is a complex issue since shape, size and distribution can change the outcome. Local inelastic deformations are a result of voids and induce other damage processes, e.g. crazing, shear yielding, fibrillation or local fracture [37].
Another way to classify damage mechanisms is the criterion of failure according to Puck [38]. Orth et al. [1] used this criterion initially for static failure and further extended it for fatigue stress. Generally it describes the occurring damage mechanisms depending on the type of stress. Interfacial debonding develops in three different types, depending on the combination of active shear stresses and tension stresses orthogonal to the fibre. Tension stresses parallel to the fibres generate fibre breakage.

2.2.2 Effects of Cyclic stress

Polymers under cyclic load can also suffer from cyclic creep and thermal failure. Cyclic creep occurs when the material is loaded with relatively high loads and low frequency. Thermal failure appears at high frequencies which generates a high temperature increase due to internal energy losses. Eventually this leads to thermal softening and loss of mechanical properties [39]. The fatigue strength for simple loads mainly depends on maximum stress respectively the maximum load. As seen in figure 2.11 the maximal bearable strain decreases linearly with the logarithm of the number of cycles.
As mentioned in chapter 2.2 the fatigue damage is mainly due to the debonding of fibre and matrix and often occurs after the first few cycles. As a result, the damage in the matrix increases and eventually causes a decrease in stiffness of the composite. In contrast to homogeneous materials such as metals, the heterogeneous internal structure of composites leads to formation of multiple cracks [37]. However, the fibres hardly show any fatigue. This would suggest that a superior matrix material would also lead to a better fatigue behaviour. In figure 2.12 two different composites are compared. Although the polyether ether ketone (PEEK) matrix shows much better static properties than the epoxy matrix, the PEEK matrix has a steeper fatigue degradation [7]. This leads Gamsted et al. [7] to the conclusion that other fatigue mechanisms in the matrix or the interface region must be active.

At the beginning of the cyclic stress in a multi-layered composite, cross-cracks initiate at the edge of the layers which are loaded in 90° direction respective to the fibre orientation. At first no growth in length is observed but the cracks grow in number. In further progress the cross-cracks grow into the middle and first delaminations between the 0° and 90° layer are recognizable. These delaminations fuse and grow in longitudinal direction until they form a continuous crack. Also in the 45° layers, cracks begin to grow in an angle of 45° from the edge on into the middle of the specimen, which leads to delaminations between adjacent layers. The final breakage depends on the type of loading. Pulsating tension load causes a fatigue breakage due to a growing number of fibre breakage, which were isolated by cracks. In tension compression loading delaminated single layers may buckle, if the delaminated area is bigger than a critical value. [10][9].

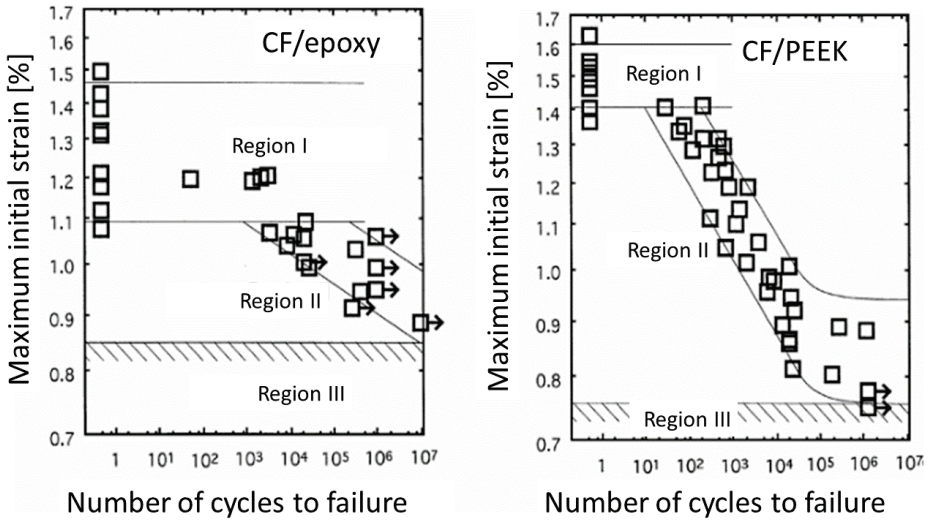

Figure 2.12: Comparison of fatigue behaviour of carbon fibre CF/epoxy and CF/PEEK composites [7]

Imperfections during manufacturing can cause micro cracks or delaminations. These imperfections can be caused by the difference in thermal expansion of fibre and matrix. Initial damages induce the growth of the cracks in the matrix through the fibre. Generally the fibre has a low strength to prevent the growth of those cracks. In figure 2.13 a schematic representation of a crack is shown. These damages can cause stress peaks. Furthermore the development of the damage is difficult to determine, even though the physical effects are measurable, e.g. [10]:

- Change in stiffness
- Higher absorbing capability of moisture
- Change in residual strength
- Change of strain-stress behaviour
- Change in damping behaviour

The orientation of the fibres to the direction of loading has also to be considered. Jen et al. [36] investigated carbon fibres AS4 with an PEEK matrix in various configurations. The failure mechanism of unidirectional composites, loaded with pulsating tension stresses in fibre direction, begins

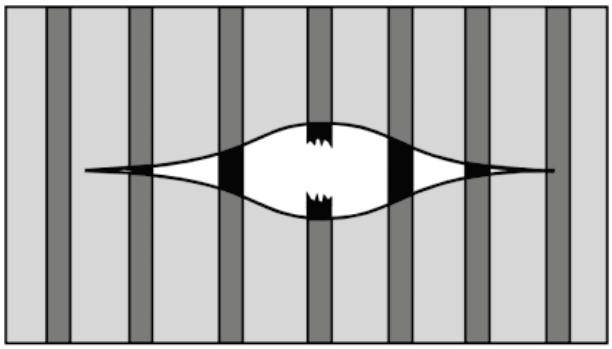

Figure 2.13: Schematic growth of a crack through matrix and fibres [7]

with matrix cracking perpendicular to the fibres and goes on with the debonding of the fibre and the matrix which leads finally to the breakage of the fibres. Considering the same configuration with compressive cyclic stress, the initial damage is inter-facial debonding and the crucial mechanism is then the buckling of the fibres, if not laterally supported.
According to Jen et al. in [36] the decisive factor is the inter-facial bonding between matrix and fibre. In figure 2.14 the results of a cyclic tension test for various loading configurations are shown. A crack initiates parallel to the fibre which eventually leads to the breakage of the specimen [36].

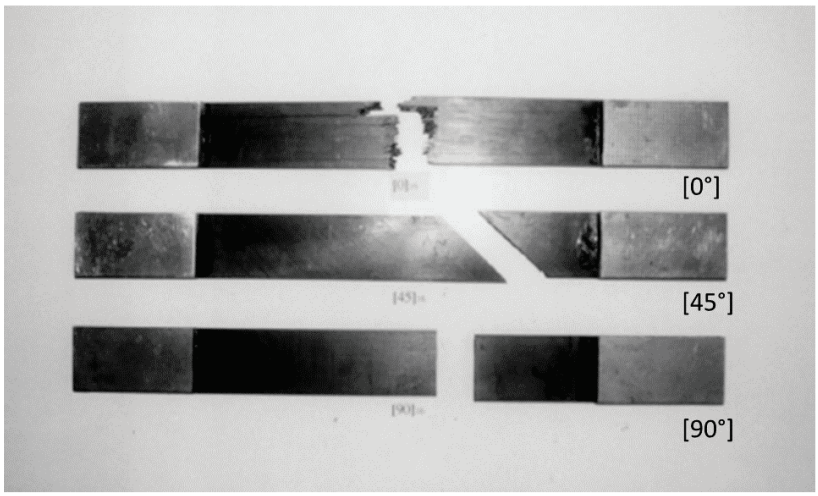

Figure 2.14: Various fracture patterns of 0°, 45° and 90° loading angle. [36]

2.2.3 Effect of Frequency on Fatigue Strength

A significant influence on the fatigue strength of composite materials is the frequency due to thermal hysteresis and higher strain rates. High testing frequencies are necessary since the testing

facility should be able to test up to the VHCF regime in reasonable time. Various authors have shown that for metallic materials the applied frequency does not have any significant influence. However, the typical viscoelastic behaviour of matrix materials suggests a high dependency on the applied testing frequency. Usually when a homogeneous, isotropic material is loaded with a certain strain value under the yield limit, the absorbed strain energy is almost completely released when unloaded. The area, limited by the paths between loading and unloading in a stress-strain curve, can be defined as the lost strain energy and is called hysteresis loop. Due to the in-homogeneous structure of polymers this hysteresis loop is well developed and indicates a high loss of energy in every cycle which is converted into heat [39]. The viscoelastic behaviour is therefore observable in time dependent materials, which shows stress relaxation or creep phenomena. This leads to the conclusion that polymer matrices show a significant dependency on the applied frequency. The form of the hysteresis and consequently the energy loss is dependent on various factors like [39]:

- Loading conditions such as frequency and stresses.
- Viscoelastic properties of the material like damping characteristics and stress relaxation behaviour.
- Heat transfer characteristics such as geometry and thermal conductivity.
- Material damage characteristics.

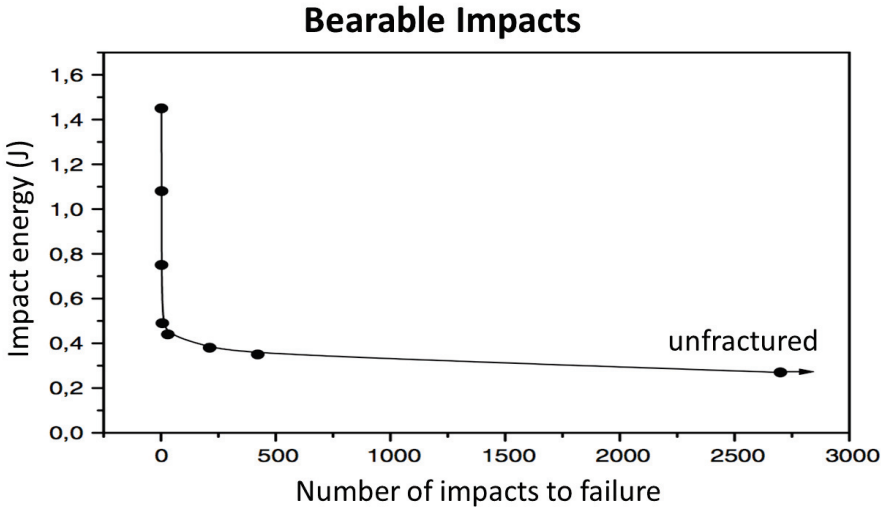

Figure 2.15: Number of bearable impacts for varying impact energies [40]

Al-Hmouz [39] reported for Carbon/PEEK composites a general decrease of fatigue life with an increase of frequency. He observed for low frequencies mainly matrix cracking which induced delaminations or fibre matrix debonding. These damages then accumulate and cause alteration of the material properties and loss of strength. For higher frequencies similar damage development was described, however the damage propagation appears faster and at higher densities.

2.2.4 Impact Loadings

In this part of the thesis the influence of impacts on the material will be explained. This shall list which effects impact-like stresses provoke in the material and how to represent them adequately. Impact loads are usually classified into two categories, i.e. low velocity and high velocity (ballistic) impact. High velocity impacts generally result in complete penetration of a projectile into the laminate. These impacts typically occur with velocities greater than $10\,\mathrm{m\,s^{-1}}$. Furthermore the damage is highly concentrated near the point of impact [41]. The impact can be characterized by its force-time curve [40].
Generally an impact load is a shock loading, where a high amplitude loading is applied in a short

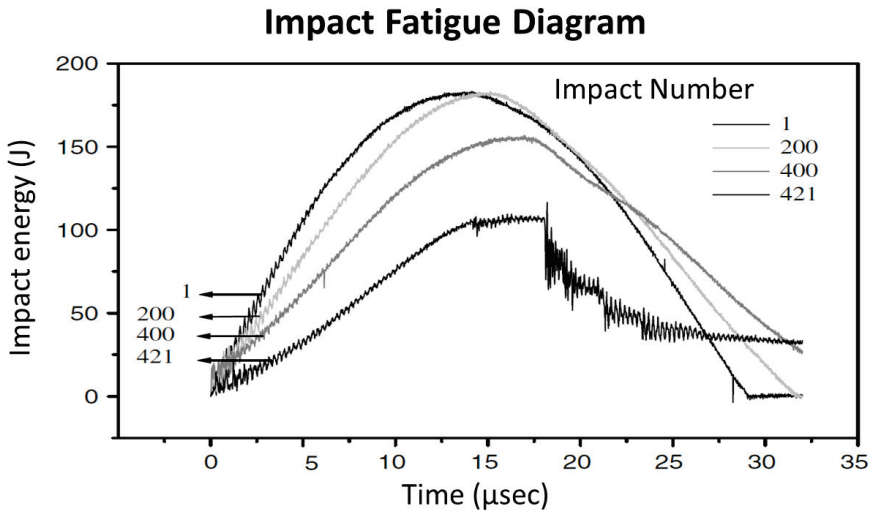

Figure 2.16: Altering force-time curve for impact fatigue [40]

period of time, respectively at high speed. Materials often behave in a more brittle way when exposed to impact loadings. Impact resistance is therefore a material property which indicates the ability to resist or to fracture under impact loading and it is a reference value for how much energy is absorbed [42]. Impact loading mainly generates delamination and debonding in composites. Furthermore the material properties such as tensile or compressive strength may be decreased [40]. The occurring damage due to the impact loading itself is usually characterized by parameters like impact velocity, fibre-matrix system and interfacial bonding.
Impact fatigue originates from low energy impacts and can be far more damaging than conventional cyclic stress [43]. Sinmazcelik et al. [40] tested specimen with relatively low impact energy ranging from 0.27 J to 1.45 J and reported a general tendency to more bearable impacts for decreasing impact energy as seen in figure 2.15. No crack initiation was observed with an impact energy lower than 0.35 J. At those low impact energies the specimens fractured like a typical impact fatigue failure. Figure 2.16 shows the altering force-time curves with the number of impacts. Depending on the fibre-matrix system the damage leads either to pulling-out of fibres or matrix cracking for systems with lower interfacial bonds, respectively transverse fibre breaking for systems with strong interfacial bonds [40].

2.2.5 Strain Rate Dependency

The strain rate is a parameter which can describe an impact. For this reason the effect of different strain rates on the fatigue strength of CFRP will be studied here. High strain rates originate from impacts, given that the strains are generated in short time periods. Thus the strain rate $\dot{\varepsilon}$ is defined as the temporal derivative of the strain ε, stated in equation 2.23 as:

$$\dot{\varepsilon} = \frac{\partial \varepsilon}{\partial t} \tag{2.23}$$

Higher strain rates can be represented by high testing frequencies as shown in chapter 4.1.4. However, due to the low thermal conductivity and a high damping factor in CFRPs high testing frequencies can cause autogenous heating which negatively influences the material behaviour. This

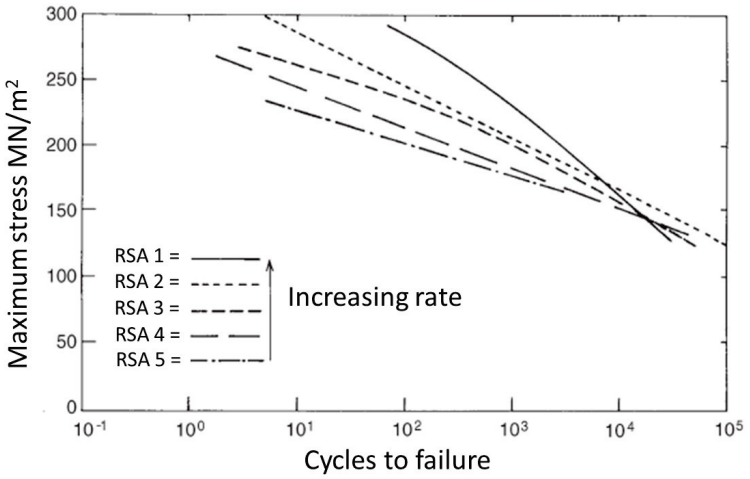

Figure 2.17: Correlation of strain rate and fatigue life [2]

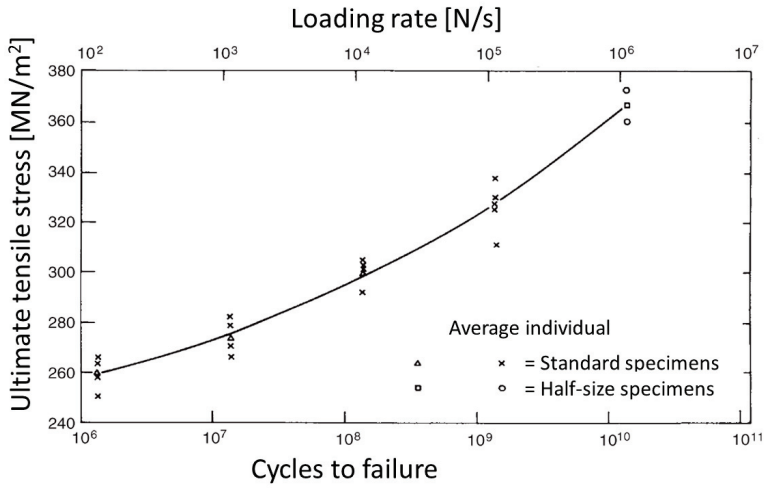

Figure 2.18: Correlation of strain rate and ultimate strength [2]

means that the self heating problem has to be examined closely. Figure 2.17 shows the relation between the applied strain rate and the fatigue life. It has to be mentioned that these curves were registered for a glass-fibre fabric epoxy, a triangle waveform to generate constant strain rates and with varying loading rate instead of strain rate. Furthermore the ultimate strength values associated with the respective strain rates are shown in figure 2.18 [2]. After normalizing the fatigue

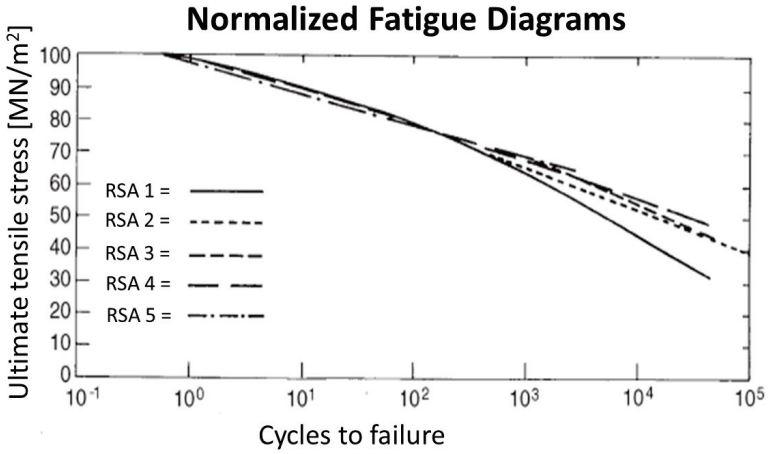

Figure 2.19: Normalized fatigue behaviour of glass fibre fabric epoxy [2]

data with its associated ultimate strength the curve shown in figure 2.19 results. As it can be seen from the graph, the fatigue behaviour stays consistent for all strain rates. The fast decrease of fatigue strength of RSA 1 can be explained by temperature effects which are caused at a higher testing frequency.
Strain rates over $0.02\,\mathrm{s}^{-1}$ effect the fatigue strength additionally with inertia and wave propagation effects depending on various parameters like geometric parameters e.g. alignment and size of the fibres and spacial content of fibres [44]. Various authors used the Split Hopkinson Pressure Bar [44] [45] to test specimens with strain rates over wide ranges with tension, compression and shear stresses.
Stiffness as well as strength can vary significantly when loaded with different strain rates. Tests for carbon/epoxy laminates showed that stiffness increases with higher strain rates and then decreases again after passing a critical value. This results in higher peak stresses for high strain rates [45]. In figure 2.20 three strain rates are given as an example of how the stiffness can vary.

Hosur et al. [45] examined cross ply laminates loaded in-plane and showed that the composite fractures under laminate splitting when loaded with moderate strain rates i.e. $82\,\mathrm{s}^{-1}$ and $163\,\mathrm{s}^{-1}$. When tested with a strain rate of $817\,\mathrm{s}^{-1}$ the laminate could not respond quickly enough and the fracture resulted in one major laminate and several sublaminates. Further it was observed that generally the stiffness of the laminates increases with higher strain rates but decreases strongly after passing a certain value [45]. According to [44] the strain to failure ratio for low strain rates is 4.5 % and the results of [46] showed a ratio of 2 % for dynamic strain rates. This confirms the assumption that at lower strain rates the laminate can dispose the stress through the whole specimen and suffers a more steady deformation [44]. Ochola et al. [44] reports a change in the mode of failure when increasing the strain rate and assumes that certain energy amounts are associated with certain failure modes. At higher strain rates the CFRP suffers under complete disintegration which requires more energy as the typical shear fracture at lower strain rates. However, his tests were

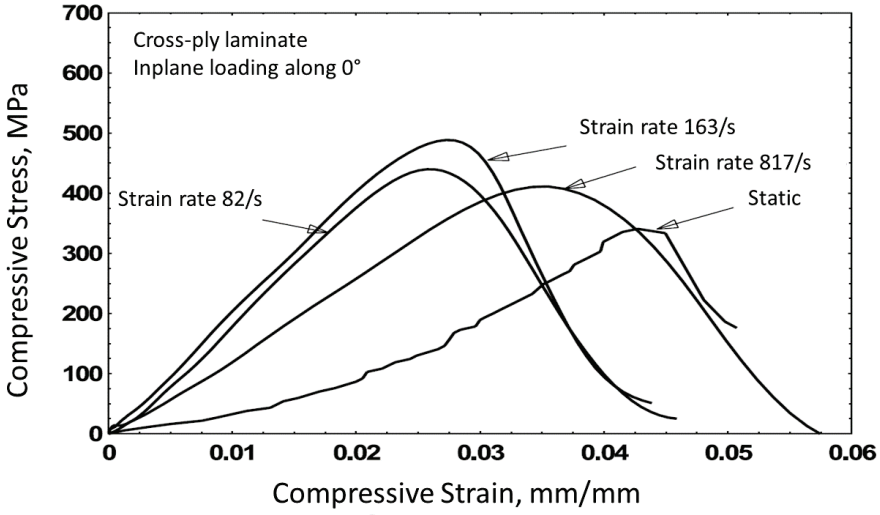

Figure 2.20: Correlation of strain rate and stiffness [45]

carried out with only two different strain rates, namely $1.0 \times 10^{-3}\,\mathrm{s}^{-1}$ and $450\,\mathrm{s}^{-1}$, and therefore do not point out a transitional phase. Nevertheless a linear relation is suggested but for off-axis loading it can also be non linear. Cantwell et al. [8] suggested a material system with higher strain to failure ratio to increase the fatigue strength of composites. This is due to the better ability to absorb impact energy when loaded with high strain rates. Therefore the impact resistance and hence the fatigue strength of CFRP is lowered when loaded with high strain rates [44].
In summary it can be said that there is a significant discrepancy between varying authors. Some of the researchers report increasing trends of the strength with strain rate, others suggest a decrease after a certain value. The normalization of the fatigue curves at various strain rates with the associated static values is a good approach. However, this method has to be approached very critically.

2.2.6 Temperature Effect

In chapter 2.2.5 the self-generated heating during high frequency tests was brought up. Besides, in figure 2.19 the temperature effect at the highest loading rate causes a stronger decrease of the fatigue strength. Hence, in this chapter the temperature effect on composite materials is reviewed to estimate the influence of a temperature change at high testing frequencies. Polymers are generally affected excessively by autogenous heating at high loading frequencies. This is caused by a high damping factor and a low thermal conductivity. The mechanical material properties and fatigue strength are reduced with increasing temperature. This means that the testing frequency is normally chosen to be as high as possible to reduce testing time, but without any excessive temperature rise in the specimen [2]. During testing the temperature of the specimen surface is usually monitored and a limiting temperature rise of maximal 10 °C is suggested in ISO 13003 with attention to the sensitivity of the used material [47]. Carbon fibre composites can suffer higher testing frequencies compared to glass- or aramid-fibre composites due to the higher thermal conductivity of the carbon fibre. Obviously in unidirectional composites a high conductivity is only given in fibre direction.
The recommended testing frequencies which range typically between 1 Hz and 25 Hz are not prac-

ticable when testing the VHCF region. Backe et al. [48] solved the temperature problem at high testing frequencies with a pulse-pause sequence. During the pause phase the specimen has time to cool down to the required temperature. This obviously lowers the effective testing frequency drastically.
The surface temperature of the specimen should be checked at least at every cycle. Additional attention has to be paid when any of the system's parameters are changed. For example the material may behave differently with varying fibre direction and orientation. An extra cooling system can be applied but has to be monitored closely since the internal temperature can be different [2].

2.2.7 Mean Stress Dependency

The mean stress dependency describes the effects of different R-ratios on the fatigue life. Generally it can be said that for fibre composites, tension loading is least critical and reversed loading causes the greatest damage and fails first when loaded with the same stress amplitude. During reversed loading, matrix cracks accumulate when stressed tensionally which gradually reduces the fatigue strength. At low cycles tension loading generally shows a better fatigue strength as compression loading, but has a steeper decreasing S-N curve and therefore fails at lower stresses at high cycles compared to the compressive loaded material. This is in good agreement with the static behaviour of the material. It has to be mentioned that these results are valid for 0° fibre orientation. For 90° fibre orientation the tensile loading showed the most damage. In this orientation the fibres do not carry any stresses and the matrix is much more sensitive to the tensile stresses. Figure 2.21 shows a constant life diagram. The resulting curves represent, for a certain number of cycles, the bearable stress amplitude associated with a bearable mean stress. These diagrams are also known as Haigh-diagrams. Equation (2.24) represents the rays for constant R-ratios[5].

$$\sigma_a = (\frac{1-R}{1+R})\sigma_m \tag{2.24}$$

The dashed curves in the diagram 2.21 represent the Goodman diagram which is represented by equation (2.25). The experimental data showed a relationship which is more like a Gerber relationship according to equation (2.26). Goodman and Gerber curves are suggested material behaviours for calculation of the mean stress dependency. σ_G and σ_p are the bearable mean stresses σ_m where the according stress amplitude σ_a is zero.

$$\sigma_{a(\sigma_m)} = \sigma_{a(\sigma_m=0)}(1 - \frac{\sigma_m}{\sigma_G}) \tag{2.25}$$

$$\sigma_{a(\sigma_m)} = \sigma_{a(\sigma_m=0)}(1 - \frac{\sigma_m}{\sigma_p})^2 \tag{2.26}$$

Dimensioning a structure according to a Goodman line will therefore lead to a very conservative design. Furthermore the diagram shows that the material seems to be more resistant to compressive stress at higher cycles but shows the opposite behaviour for small numbers of cycles as stated above.

2.3 Estimation of Fatigue Life

The estimation of fatigue life of CFRPs is a most interesting and difficult issue. A high number of factors and parameters affect the occurring failure mechanisms and their progress. Making an

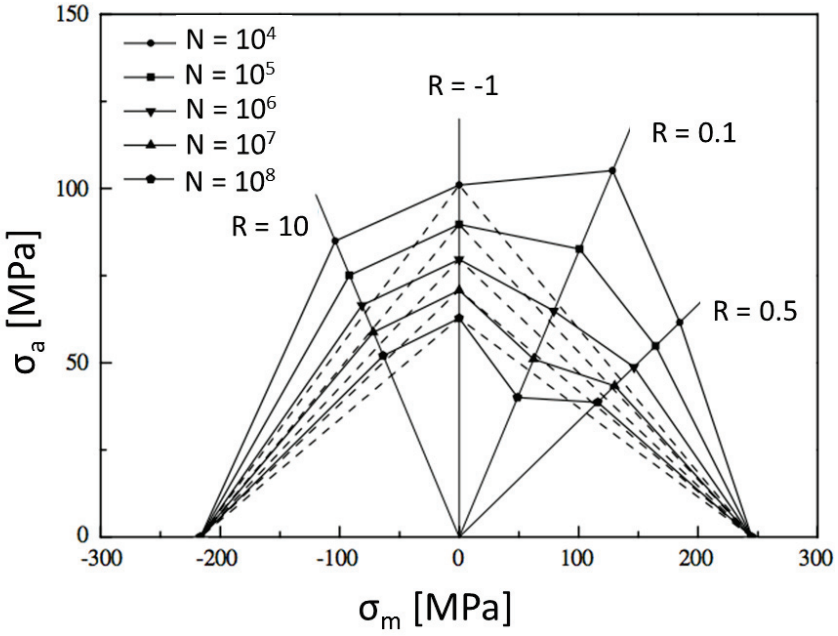

Figure 2.21: Constant life diagram from [5]

accurate prediction for the life of a material or even a structure involves difficulties.
Contrary to metallic materials, the analysis of initiation, propagation and unstable growth single cracks does not apply to composite materials. Talreja in [37] suggests that due to the local damage mechanisms a homogenising of a composite material and describing fatigue in terms of average stresses can not lead to adequate predictions. As already mentioned above, the fatigue life diagram describes the fatigue behaviour of FRPs better since the occurring strain is actually the limiting factor. Another fact that is in favour of the fatigue life diagram, is the possibility to apply a mechanism based model of life prediction. [37].
According to Orth et al. [1] there are generally two approaches for a fatigue life prediction:

1. **Fatigue Life Model:** Strain based methods as described above. S/N curves and mean stress dependency deliver information for a statement about fatigue life.

2. **Phenomenological models:** Macroscopic physical parameters, e.g. stiffness or residual strength degradation, form the base for a fatigue life analysis. The degradation of stiffness is approximated, based on calculated stress distribution and the loading history. This method is more complex and requires more resources but comes up with better results and a statement about the progress of damage [5].

A combination of those two approaches would evaluate the loss in stiffness from the fatigue test and further include the stress rearrangements in a structure. The requirements for an accurate life prediction model are according to Orth et al. [1]:

- Ability to analyse the used laminates

- Based on elastic stresses
- Applicable and expandable for non-proportional multi-axial stress states
- Requirement for as few as possible material tests

Thereby it is suggested to use material characterizations of unidirectional single layers to predict the behaviour of the whole composite. The proposed life model by Orth et al. [1] is based on the extension of the static failure criteria by Puck. Depending on the applied mean stress and active stresses in the lamina, different damage mechanisms result. Finally a Haigh diagram was suggested where the mean stress and fibre orientation are plotted over the fatigue strength for a life of 2×10^6 cycles. However, no predictions or estimations for fatigue life over 2×10^6 cycles is suggested since there is no experimental data available yet.

2.3.1 Criterion of Failure

To make a statement about the fatigue life of a material it is necessary to define a criterion of failure. For strain based methods either the complete breakage or the degradation of stiffness under a certain value are typical criteria. The degradation of stiffness can be measured during a fatigue test without much additional effort. The stiffness can be calculated from the force displacement relation. According to [1] the stiffness degradation can be split into three regions:

- **Region I:** A fast decrease of stiffness can be observed of about $20\,\% - 30\,\%$ of the initial stiffness.
- **Region II:** Small linear degradation of stiffness over a wide range of life of circa $10\,\%$ of the initial stiffness.
- **Region III:** The stiffness is again decreasing fast which leads eventually to breakage of the composite.

As a criterion of failure the transition point from region II to region III is suggested. This point can be received due to the change of the gradient of the tangent of the stiffness curve. Such stiffness curves are typical for matrix dominated systems. However, there are material systems which do not show this degradation of stiffness. For such materials systems the stiffness degradation can not be assigned as a criterion for failure. In these cases breakage is advised as failure criterion [1].

Chapter 3

Fundamentals: Very High Cycle Fatigue (VHCF) Devices and Techniques

A material suffers from fatigue when it is loaded cyclically over a period of time. The very high cycle fatigue describes the material behaviour over 1×10^7 cycles. Testing in the VHCF region is a difficult and complex issue due to various reasons. When loading a specimen with 1×10^9 cycles or more, a rather high testing frequency is required to keep the testing time within reasonable limits. On the other hand it should also be considered that high frequencies can lead to significant warming of the specimen due to material damping, which, especially in polymers, can affect the material properties [49]. Additionally the damping properties of unidirectional fibre composites highly depends on the type of loading [5]. Another aspect to consider, when testing the specimen for compression loading, is buckling. Michel et al. [3] reported solving this problem with shorter specimen below the first free length of an Euler buckling mode. A mechanical lateral support for the specimen is not advised due to fretting phenomena between support and specimen especially at higher frequencies.
When designing a testing machine for VHCF one also has to consider that the machine itself must withstand the high number of cycles for every test [50].
Finally a testing device should be designed to meet these requirements. In the following part of this thesis various testing facilities of different authors will be examined and discussed to find a reasonable design for a testing machine which should simulate the actual loads and stresses in the most realistic manner.

3.1 Servo Hydraulic Testing Machines

The servo-hydraulic devices are standard machines for testing up to 1×10^7 cycles and generally work within a frequency range between 1 Hz and 50 Hz. High energy losses resulting from the regeneration of the oil pressure for every cycle makes a cooling device necessary [51]. Testing with 50 Hz would take over seven months to reach 1×10^9 cycles. By using 1000 Hz the testing time can be reduced to eleven days.
For this reason servo hydraulic testing systems were developed which can work at a frequency of

up to 1000 Hz [50]. Resonances become an important issue at such high frequencies. There are testing schemes which take advantage of the resonance properties of the system to produce high frequencies. When using servo hydraulic stimulation, the arrangement of the machine should avoid resonances. This can be achieved with stiff frames, large masses and short columns. However, it is suggested to determine the eigenfrequencies of every specific arrangement. Dual high frequency servo valves or high flow voice coils generate the necessary flow rates to generate higher frequencies as usual [50].
Another thing to consider at high frequencies are the relatively high acceleration forces of the moving masses. These forces need to be included in calculations and must be compensated in the control loop. The load signal can differ significantly if not compensated [50].

3.2 Resonant Testing Machines

A resonance testing setup stands out due to its generally higher testing frequencies and a lower energy consumption compared to servo-hydraulic facilities. A resonant testing system is typically a mechanical vibrating system where the actuator, the frame and the specimen compose a complex harmonic oscillator. Theoretically the system has an infinite number of eigen modes and can, for example, be stimulated electromagnetically in the desired resonant frequency. An eigen-mode has to be chosen which induces sufficiently high loads into the specimen without stressing the load frame and the remaining system. Typical reachable frequencies with those systems lie between 50 Hz and 250 Hz [33] [51].

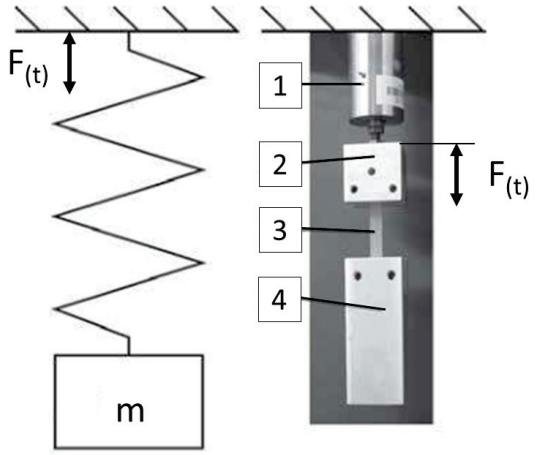

Figure 3.1: Simple spring mass system used as testing machine. 1: actuator; 2: clamp; 3: specimen; 4: counter mass [33]

3.2.1 General Configuration of Resonant Testing Machines

The simplest configuration of a resonant testing system consists of a spring and a mass, namely an one mass oscillator. Adam et al. [33] implemented this configuration using the specimen as spring

element and a counter mass mounted to the specimen as seen in figure 3.1. The actor was fixed to a base point. In this case a piezoelectric actuator was chosen. Piezoelectric actuators and their associated problems are explicitly described in chapter 3.3. The specimen was then fixed to the counter mass and the actuator using clamps.
Initial and transient effects can be avoided by using a closed control unit that uses the displacement

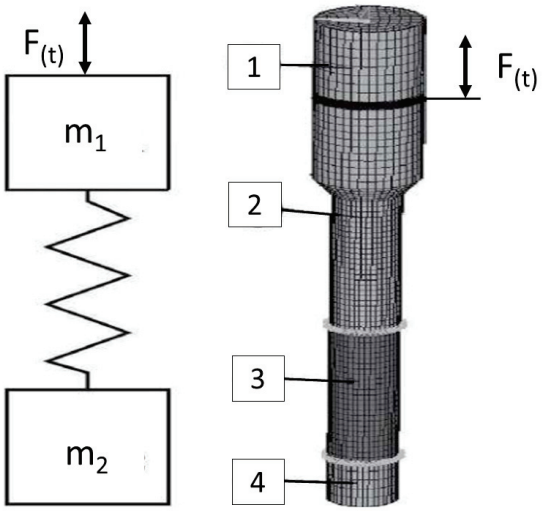

Figure 3.2: Two mass spring system used as testing machine. 1: actuator; 2: booster; 3: specimen; 4: counter mass [33]

of the counter mass or the strain of the specimen as a reference. Furthermore the actuator has to be rather powerful to generate the power and forces to load the specimen with appropriate stresses. Usually the test stand turns out to be large compared to the specimen. The cooling system and the control unit have to be highly accurate to be able to work with such actuators.
Another possibility is a two mass system. The system is represented in figure 3.2. The advantage of this more complex configuration is that the actuator is taken out of the flow of forces and can be smaller. In other words, in this configuration, high loads are induced into the specimen whereas the test stand is basically unloaded [33]. To generate stress ratios other than $R = -1$, the resonant oscillating system has to be mounted into an additional system which overlies a static force. This can be achieved by using a static servo hydraulic test stand or the like. This way the stress ratio can be adjusted to the required values. Another possibility is to combine the resonant system with a servo hydraulic fatigue testing machine. That way the specimen can be loaded simultaneously with high frequency, low amplitude stress and low frequency, high amplitude stress [51].

3.2.2 Vibrating System

In a resonant testing machine the testing frequency supplied from the machine, respectively the actuator must be a natural frequency of the oscillating system. The specimen forms a complex system with its actuator, the fixing and the horn. This system needs to be well analysed and adjusted so that the specimen vibrates in the correct eigenmode and the strain and stresses occur at the correct section of the specimen.
To make the control and excitation of a vibrating system as simple as possible it is necessary to

keep the number of displacement nodes as low as possible. Due to the symmetry of the specimen the displacement in the specimen's center should be zero and is therefore an obligatory node. Additionally any displacement where the static load is applied should be avoided, therefore a system as seen in figure 3.3 has three displacement nodes and two stress nodes stated as DN and SN respectively. Between two neighbouring displacement nodes a stress node can be found exactly at the ends of the specimen [52]. The exact calculations are found in chapter 4.3

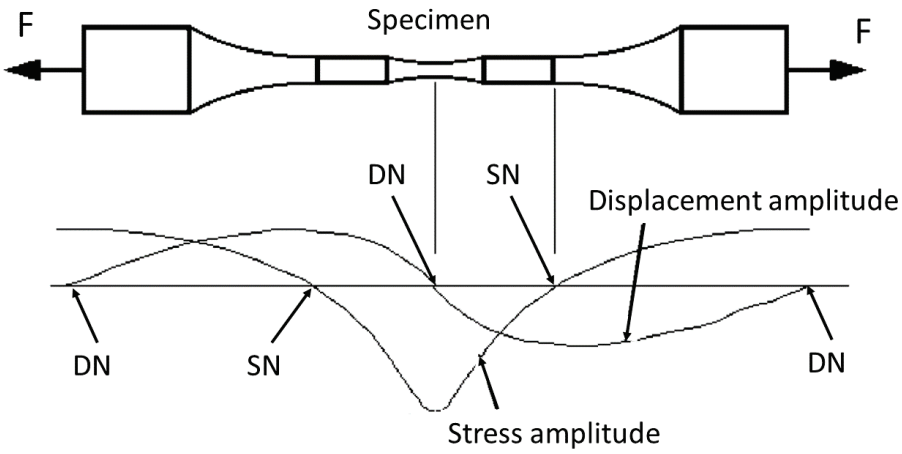

Figure 3.3: Displacement and stress curves through a specimen [52]

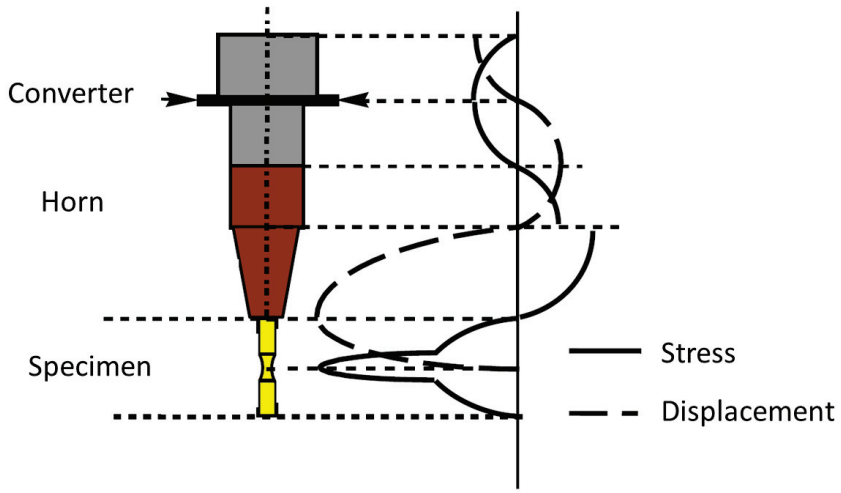

Figure 3.4: Vibrating system of a piezoelectric stimulated test facility [53]

3.3 Piezoelectric Driven Ultrasonic Testing Machines

A big advantage of piezoelectric driven actuators is their wide applicable frequency range from quasi-static into the kHz region. High accuracy with reasonable high forces is achieved in combination with an appropriate electrical amplifier and controller.
The effective principle behind piezoelectric driven testing machines is the inverse piezoelectric effect. A piezoelectric crystal exposed to an electrical field shows this effect and expands up to 0.1 % of its length. This expansion is used to generate the desired loading [54]. The underlying mechanism of ultrasonic testing facilities is to cause oscillations in ultrasonic resonance at one of the specimen's longitudinal modes [53]. The principle is very similar to that from resonant testing machines as explained in chapter 3.2.
As already mentioned, testing time is a crucial factor especially in the VHCF regime. Ultrasonic fatigue testing offers an opportunity to test at frequencies up to 20 kHz. Naturally it is necessary to work within the resonance frequencies of the specimen. Hence the design of all vibrating parts has to be correctly adjusted to fit the requirements. Additionally the desired amplitudes are reached quickly. A feed-back control and an induction displacement gauge is required to avoid overshooting which additionally increases the adjustment accuracy [51].

3.3.1 General Configuration and Principle of Piezoelectric Driven Ultrasonic Testing Machines

Generally an ultrasonic fatigue test machine consists of the following parts[51][53]:

- A generator capable of producing high frequencies connected to a piezoelectric converter which transforms the sinusoidal electrical signals into mechanical vibration. To amplify the amplitude an ultrasonic horn is installed.
- To control and adjust various testing parameters such as amplitude, pulse-pause sequence and frequency a control unit is necessary. Measuring units facilitate the online classification of desired values.
- When testing fully reversed tension compression loading, the specimen has to be mounted at only one end. Usually a servo hydraulic system is mounted to generate the static overlying load for various stress ratios. This configuration offers the opportunity to generate a complex loading by superposing different load signals from the resonant system and the servo hydraulic system. [53]
- The system should also provide possibilities to mount devices like cooling system, cameras, strain gauges, temperature monitoring etc.

Figure 3.4 shows the vibrating system with converter, horn and specimen. The stresses and the displacement are also represented. The horn must be designed in a way to amplify the displacement to the required values. The vibrating horn has two displacement maxima and one node as seen in figure 3.5. The amplification factor F_{Amp} is defined by the two displacement maxima V_1 and V_2 as stated in equation (3.1).

$$F_{Amp} = \frac{|V_1|}{|V_2|} \tag{3.1}$$

The distribution and the amplification factor of those maxima depend on the geometrical form. A finite element analysis can be useful if the geometry is complex [53].
As already mentioned in chapter 2.2, the damping of CFRP at high frequencies can induce high

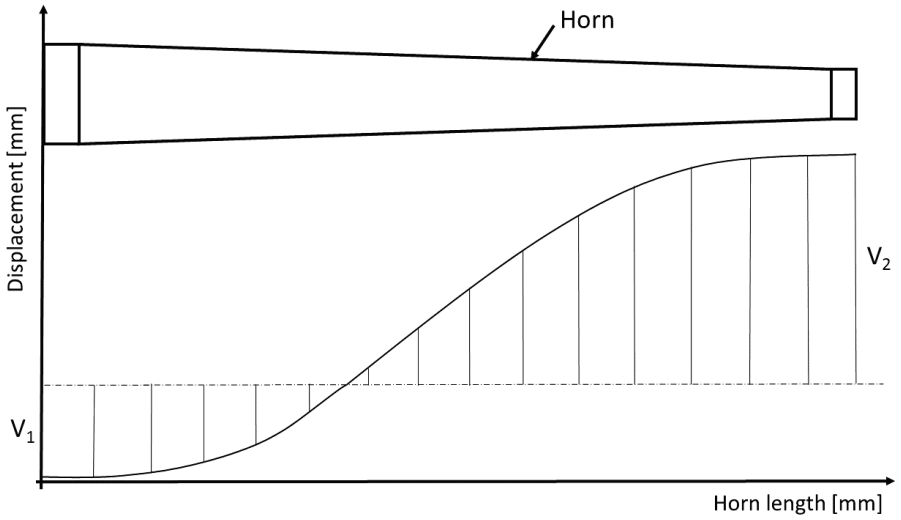

Figure 3.5: Displacement distribution of an amplifying horn [53]

temperatures and alter the material properties and finally the results of the tests. Various solutions for this problems were suggested. E.g. in [48] the testing is executed with pulse-pause sequences in addition to permanent cooling with dry air to keep the temperature under the glass transition temperature. Figure 3.6 shows a pulse-pause sequence and the correlating temperature development. The pause phases may take even more time to cool down than the pulse phase. This lowers the effective testing frequency significantly compared to the nominal frequency [54].
However, Adam et al. [33] use bending fatigue tests because then the stresses are mainly in the exterior layers of the specimen. This means that also the heat is essentially generated at the exterior layers and can efficiently be transferred to the surrounding air. They showed that this configuration leads to temperature raise of approximately 10 °C relative to the ambient temperature. Stanzl-Tschegg et al. [51] suggests a pulse length of 25 ms to 100 ms and pauses of 25 ms to 1000 ms depending on the material damping. Naturally, additional cooling with compressed gasses or liquids can be installed, though corrosion or moisture effects must be considered. Furthermore, gauges need to be mounted to measure displacement respectively the strain. These systems have to be very fast and accurate to record the displacements of the vibrating specimen appropriately. Inductive or capacitive displacement gauges measure the oscillating displacement amplitudes when mounted at one end of the specimen. However, optical methods like a laser doppler vibrometer might be used to record the absolute values of the change in length Δl. The information is needed for the closed control loop and for the calculation of the resulting strain $\varepsilon = \Delta l / l_0$. An accurate control of the resonance system is also useful to detect any cracks since the stiffness and further the resonance frequency can alter with occurring or growing cracks. The frequency must continuously be adjusted to excite the system constantly at its natural frequency. The strain amplitudes $\varepsilon_{(t)}$ can also be measured directly with strain gauges. If applicable, the stresses can be calculated using Hook's material law, stated in equation (3.2) [51] [53]:

$$\sigma_{(t)} = E\varepsilon_{(t)} \tag{3.2}$$

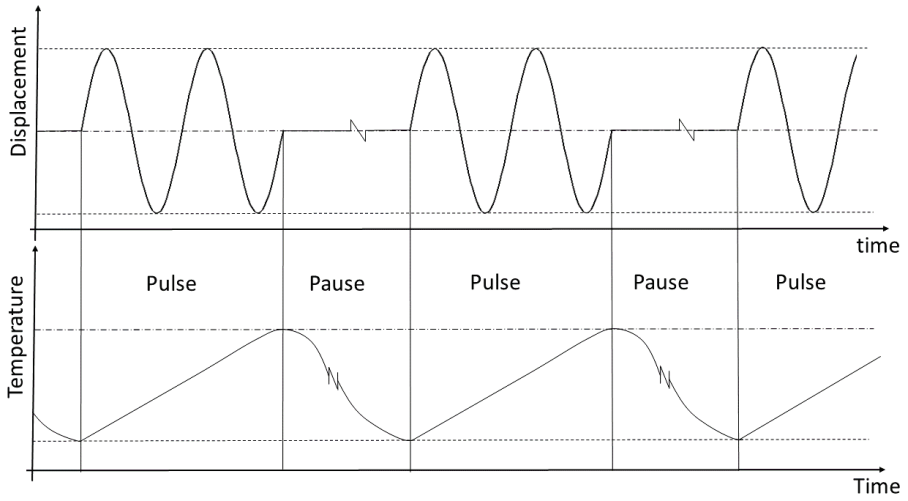

Figure 3.6: Pulse-pause sequence and temperature development

When working with a strain gauge the placement of the gauge on the specimen is crucial and can lead to incorrect measurements.

3.4 Characteristics of Piezoelectric Actuators

Testing facilities using piezoelectric crystals work with very high accuracy and are less energy consuming as for example servo hydraulic testing machines. The two most important parameters of a piezoelectric crystal are the free stroke and the blocking force. Both are reached with maximum voltage. For this reason piezoelectric actuators are often specified by these two parameters. Blocking force and free stroke are defined as following [55]:

- The free stroke is the maximal displacement achieved by the actuator at a given voltage without external load.
- The blocking force is the required force to push back a fully energized actuator to zero displacement.

It is important to consider that piezoelectric actuators, on the contrary to e.g. hydraulic driven actuators, are not capable of generating the maximum force at every actuator position. Figure 3.7 shows the relationship between the stroke of the actuator and the blocking force and indicates the operating range for various grades of stiffness of specimens [54].
The piezoelectric actuator has to be capable of generating forces up to several kN and an excitation displacement of approximately 10 µm. High voltage actuators are generally able to work with higher forces and are therefore the suggested choice. Low voltage actuators reach large displacements more easily [56].
Usually piezoelectric actuators are either cylinders or ring shaped. Ring shaped actors offer additional possibilities regarding mounting and using the actuator. Furthermore the pipe shaped structure is more resistant to buckling compared to a cylinder with the same volume. Generated

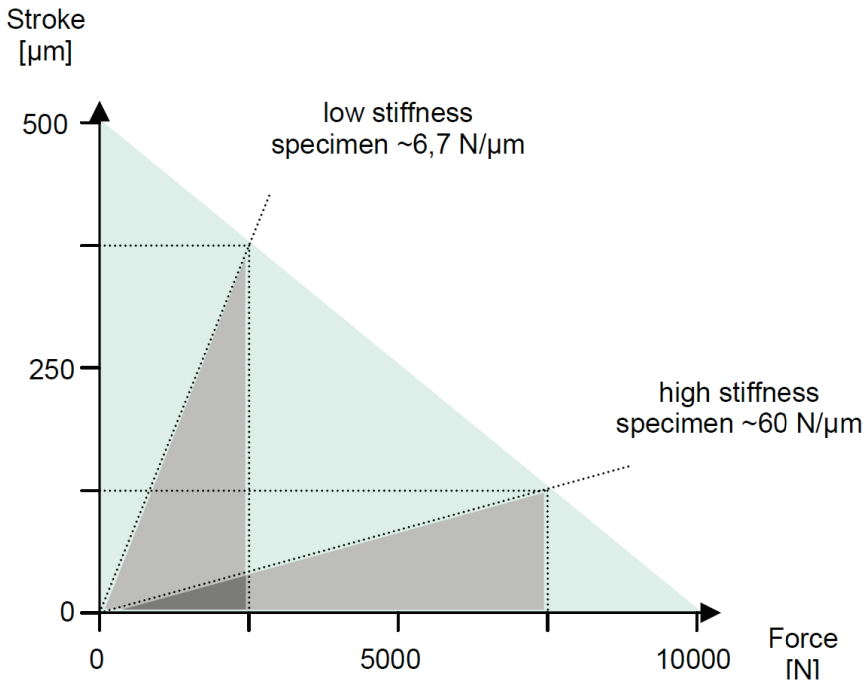

Figure 3.7: Relation of actuator stroke and blocking force [54]

heat from losses is easier removed and can radiate faster to the surrounding medium due to the larger surface to volume ratio [56].
When applying piezoelectric actuators it is of great importance to avoid any tension forces acting on the actor. Therefore a pre-stress system needs to be applied which compensates for tension stresses. Usually passively working force capacities like mechanical or hydraulic spring elements are used. The pre-stress system has to be dimensioned so that the actor is never confronted with tension forces. Figure 3.8 shows a working principle of a pre-stress system.
Piezoelectric elements are predestined for dynamic applications. However, high acceleration rates correlate with high electric power usage at high frequencies which can cause significant warming of the actuator. Generally piezoelectric actuators are not able to work at their resonant frequency but can be applied over a wide range of frequencies up to 10 kHz. However, there are actors which work in their resonant frequency, usually over 20 kHz, but are then reduced to small bandwidths around this natural frequency. For excessive fatigue applications, the exciting system has to be dimensioned to withstand high frequencies over enduring cycles. The heating of the actuator plays an important role and can reduce the life of the system significantly. Piezoelectric actuators which work in their resonant frequency are made of a specific ceramic. Normal actors should never be excited at their natural frequency which would result in a fast failure of the ceramic [56].

3.5 Data Acquisition and Control Unit

The data acquisition and control unit is responsible for measuring the strain or stresses respectively in the specimen and keep them in the desired ranges. The measured data are finally evaluated and should deliver a statement about the fatigue behaviour of CFRP.

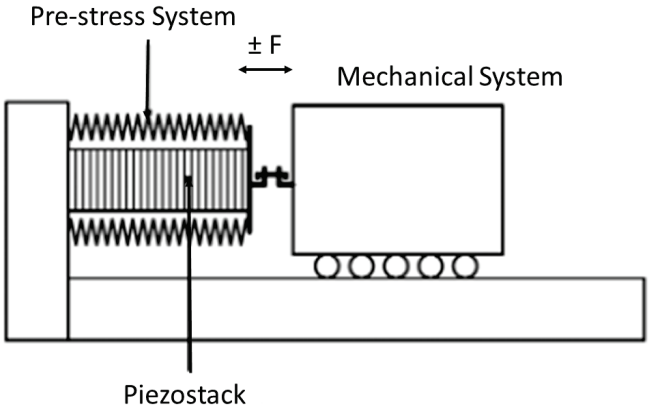

Figure 3.8: Internal pre-stress system [56]

Stanzl-Tschegg et al. [51] suggests an inductive coil assembly in combination with a control unit and consequently creates a strain-rate controlled test. The mentioned assembly leads to uncertainties of maximal $\pm 1\,\%$ of the amplitude. Additionally the accuracy stays steady over a wide range of ultrasonic power, which should be verified by using online data acquisition [51].
The specimen should be loaded with a constant amplitude during the whole test. However, in a high frequency test machine the amplitude and hence the strain depends on various parameters. To ensure a highly accurate test, a control unit is necessary which adjusts the testing frequency and power input of the piezoelectric actuator so that the same strain is achieved in every cycle.

For controlling the testing facility and for data processing reasons it is necessary to install a data acquisition device. Recording the peak and through values of the control criterion and the associated displacement values is a minimum requirement. The data has to be filed continuously with a certain frequency. The recording frequency depends on the frequency the specimen is stressed with. The further data processing practice can include determination of the modulus loss or damping factor. The monitoring of the specimen temperature, acoustic emission or in-situ ultrasonic scanning can also be a way to report degradation [2].

Data acquisition is one of the most crucial issues for collecting experimental data. Accuracy and preciseness of the measurement is the key to correct results. For fatigue life prediction experimental data is needed which has to include measurement of localized loads, loading frequency and of course the number of cycles. Also the temperature is usually recorded along with the number of cycles [57].

3.5.1 Strain Based Testing

Strain in a material is defined as the relative displacement of points within a body that is generated by an external force [58]. Usually stress based fatigue testing is the preferred method because it is more easily applicable. This method works well as long as the material is only stressed in its elastic

region. Especially in composites the occurring stress is difficult to identify because they consist of different components. According to Talreja et al. [37] there are two reasons to examine the fatigue of composites strain based:

1: The failure strain of the composite correspondents to the failure strain of the fibre, independently of the fibre volume fraction.

2: The fatigue limit of the composite is limited by the fatigue limit of the matrix. Due to the fibre constraint, the matrix is stressed strain controlled, even if the composite is tested load controlled.

Strain measurement on the other hand can be difficult to apply. There are various methods to measure strain directly or indirectly. These are listed and shortly explained in the following. The measured strain is then fed to the controller for closed loop control. The alignment of the measuring device is crucial and is essential for the accuracy of the test [57].

3.5.1.1 Extensometer

Usually an extensometer measures the strain indirectly over the displacement of the upper and lower end of the strained length of the specimen. Another way is using a clip gauge. Extensometers measure the displacement using two knives touching the surface of the specimen which then are moved according to the induced strain in the specimen. This method is commonly used, but has its restrictions in bandwidth. Additionally the knives may influence the fatigue life of soft materials [57],[59].

3.5.1.2 Strain Gauge

Strain gauges are resistive devices and can measure the strain directly on the surface of the examined object. The working principle is based on the change of electrical resistance with varying geometrical dimensions. Therefore the resistance change of a material under mechanical strain can be used to measure small strains very accurately. The change of the resistance of the strain gauge is directly proportional to the applied strain which makes the strain gauge a practical and widely used instrument. Strain gauges are generally a good solution for their high bandwidth and accuracy. However, the placement can be very problematic to achieve correct results. Anyhow, the most limiting factor for strain gauges is their restricted life, which can be significantly below the desired testing cycles. A strain gauge is often used to verify the accuracy of the actually applied measurement system [57],[59].

3.5.1.3 Optical Strain Measurement

Generally optical methods determine differences in path lengths of light from the same source. These path length differences can then be used to determine strain and strain fields. Full-field evaluation of strain caused displacement is possible with those devices. There are various methods of interferometry, for example holographic interferometry or speckle-shearing interferometry with various advantages and disadvantages [57]. Those systems are highly accurate and have high bandwidths, however they are expensive.
A 3-D scanning laser vibrometer is an optical measurement device especially developed for high

frequency applications. A third applied laser allows to make statements about the profoundness as well. This device is used for ultrasonic fatigue tests in which the testing frequencies are higher than 20 kHz. It measures the eigenfrequencies as well as the strain in the specimen [60].

3.5.1.4 Digital Image Correlation

Digital Image Correlation (DIC) is also a widely used instrument to detect strain directly in a specimen. Images are taken continuously of the natural texture or an artificial pattern on the specimen's surface and are then matched by correlation. With this method the exact strain on the surface can be measured. The DIC method needs a lot of calculation time, however Tao et al. [59] applied this system in a real time system by optimizing the calculation process and even used it as control value in a closed loop control. A strain data acquisition frequency of 10 Hz was reached [59].

Chapter 4

Simulations and Design Process of a Resonant Testing Device

In the following chapter the execution of the simulation process for the loadings and the design process is represented. It is important to point out that the analysis of the occurring loadings in the ram are executed on the current cast iron ram and are not valid for a component made of CFRP. Further the results of this simulation are used for the estimation of the required testing signal. This part of the thesis is a suggestion for a design process of the testing signal and has to be remade for a ram made of CFRP. The design process includes the calibration of the vibrating system, its simulation and the design of the specimen.

4.1 Analysis of the Loading and Resulting Stresses

The scope of this thesis is to develop a testing facility to estimate the life of a ram of a high performance stamping press made of CFRP. A lighter ram can reduce mass forces which allows higher working frequencies and therefore higher productivity. However, the ram is exposed to relatively high loads during its life and a very high number of cycles. Furthermore the machine works at high shots per minutes and the time, in which the load will be applied, is short. This leads to the conclusion that the ram is exposed to a complex loading composed of an impact-like load and a smaller cyclic load. The exact stresses depend on a number of parameters like material properties of the working material or the tool. For this reason, the stresses a ram is exposed to, will be estimated, discussed and analysed. The effective stresses and strains in the ram are difficult to identify. Therefore a simulation will be needed where the resulting stresses are derived from the stamping force curve. The exact design of the new ram made of CFRP is not available yet. The global behaviour of the composite component should be as close as possible to the current steel ram. However, local effects will differ significantly.
The following simulation should help to make an estimation of the expected damage mechanisms and how to reproduce them in a testing device. However, this method has to be remade for a ram made of CFRP.

Performance Stamping Machine BSTA 200-60 The BSTA 200-60 is a high speed stamping machine made by BRUDERER® AG and has a press force of 200 kN. The machine is

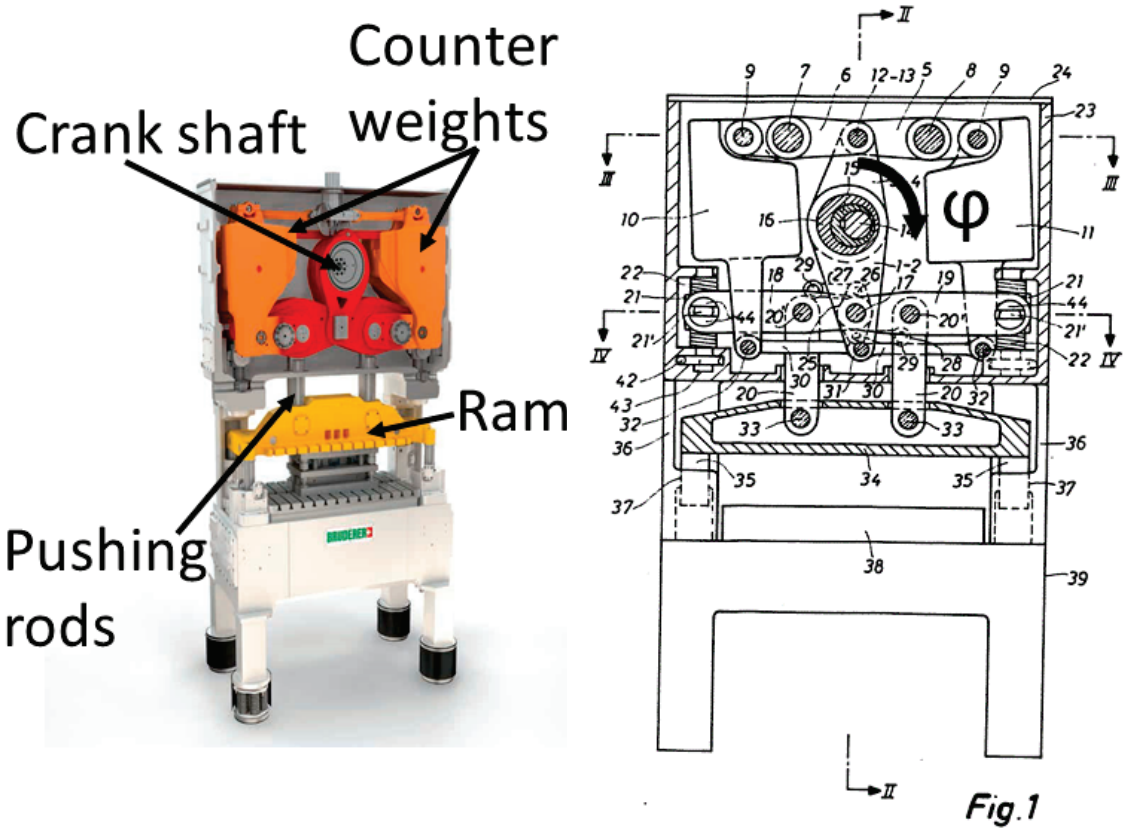

(a) BSTA 200-60 machine (b) Sketch of the transmission unit

Figure 4.1: BSTA 200-60 machine by BRUDERER® AG and its transmission unit [61] [62]

represented in figure 4.1a. The press can work with up to 2000 shots per minute (SPM) and the goal of a lighter structure is to increase the speed up to 2500 SPM. The kinetic relations of the mechanics are given by BRUDERER® AG and shall help to get an idea of the occurring stresses. A specialized lever system converts the rotational movement from an eccentric crank shaft to an uniformly translational movement of the ram. The transmission unit is shown in figure 4.1b. The upper dead center is by definition at a crank angle of $\varphi = 0°$ of the eccentric shaft and the lower dead center at $\varphi = 180°$ of the shaft. The drive system includes a special system for balancing the masses.

4.1.1 Occurring Forces and Stresses

Since a force or stress analysis of the ram is not available, the active forces and the resulting forces that are induced into the ram have to be assessed. The resulting loadings in the machine depend on various parameters hence an exact evaluation of the occurring stresses is not usable. However, qualitative force stroke developments are known for stamping processes from different sources [61] [63]. The velocity of the ram when hitting the sheet is at 150° crank angle approximately $0.5\,\mathrm{m\,s^{-1}}$ for the BSTA 200-60 machine at 2500 RPM. Therefore the impact can be classified as a low velocity impact and stress wave effects can be neglected. The relevant force time curve which stresses the ram, is calculated from an assumed stamping force time curve. The characteristic

curve depends on the thickness of the plate which has to be cut, the stamping velocity, hardness of the material, the form of the cut out and other parameters. The impact energy is then given by the total area under the force-time curve.

Since the force development in the ram varies with so much variable parameters, there are no existing data sets which exactly represent the force time curve. For this reason an empirical approximation of the force time curve was generated using MATLAB®. The scope of the approximation was to represent the force stroke curve given in the left-hand diagram in figure 4.2 provided by BRUDERER® AG [61]. In figure 4.2 the right-hand diagram shows a process with some softer material. This leads to smaller peak forces but the more elastic behaviour of the material needs more time to be broken through. For the simulation, the left-handed diagram is chosen because its higher force peak and the shorter time in which the process is done lead to higher stresses and strain rates which is more critical for the reviewed material.

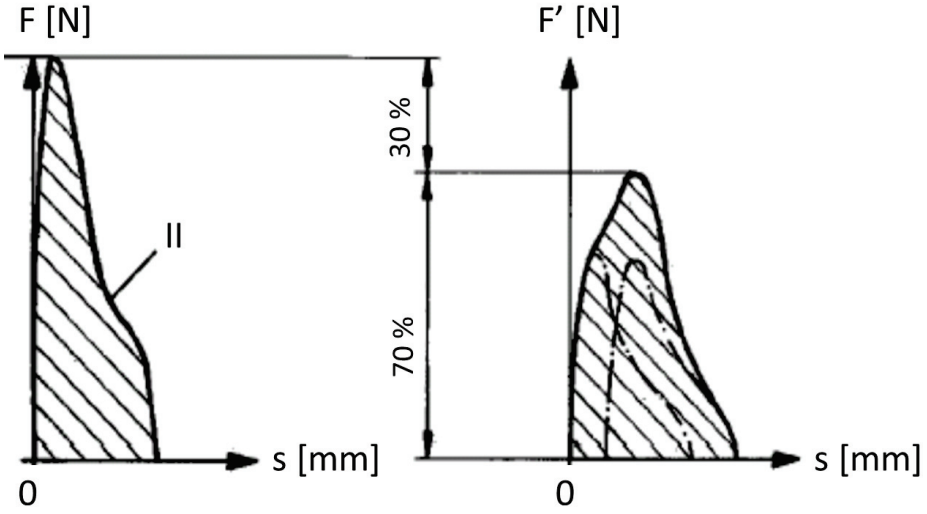

Figure 4.2: Typical force stroke development for a hard (left diagram) and a soft material (right diagram) [61]

The force stroke curve is further converted into the force time curve using the kinematic relations. This is the required curve for the simulation of the stamping process and will lead to an adequate approximation of the strain rates and maximum occurring stresses. The geometrical approximation of the force development can be drawn from the characteristic parameters of the stamping process. The maximum force is the highest force provided by the power unit. The maximum force marks the peak of the curve. The time when this maxima is reached, depends largely on the cut material and its strain hardening exponent and can be well approximated with a sinusoidal development. Further the depth at which the sheet is broken through, represents the point where the force curve breaks away at the end. The chosen typical parameters, suggested by BRUDERER®, for the approximation are listed in table 4.1 [61]. A MATLAB® script was written which approximates the given curves with sinusoidal functions and a sudden breakaway of the force. Afterwards a polynomial function of 8^{th} degree was fitted to remove any discontinuity. The generated resulting force stroke and force time curves are shown in figure 4.3. The kinetic relations define the stamping time and are therefore a crucial factor for the strain rate and the outcome of the simulation.
It is important to point out that these curves largely depend on several influencing factors. An

exact statement about the force development in the ram is therefore hardly possible. The scope of this approach is to recreate a worst case scenario to estimate the maximal strain, strain rates and strain accelerations. As mentioned, a ram is for ten years or more in operation and has to cope with various loadings. The scope is to choose a material which is capable of dealing with any possible loading in the nominal force range.

Process Parameters:	
Maximum force F_{Max}	200 kN
Residual force at breakthrough	30 % of F_{Max}
Speed of the machine	2500 SPM
Crank angle when hitting the sheet	145°
Crank angle at F_{Max}	150°
Sheet thickness	0.8 mm
Cutting depth at breakthrough	0.5 mm

Table 4.1: Typical parameters for a stamping process

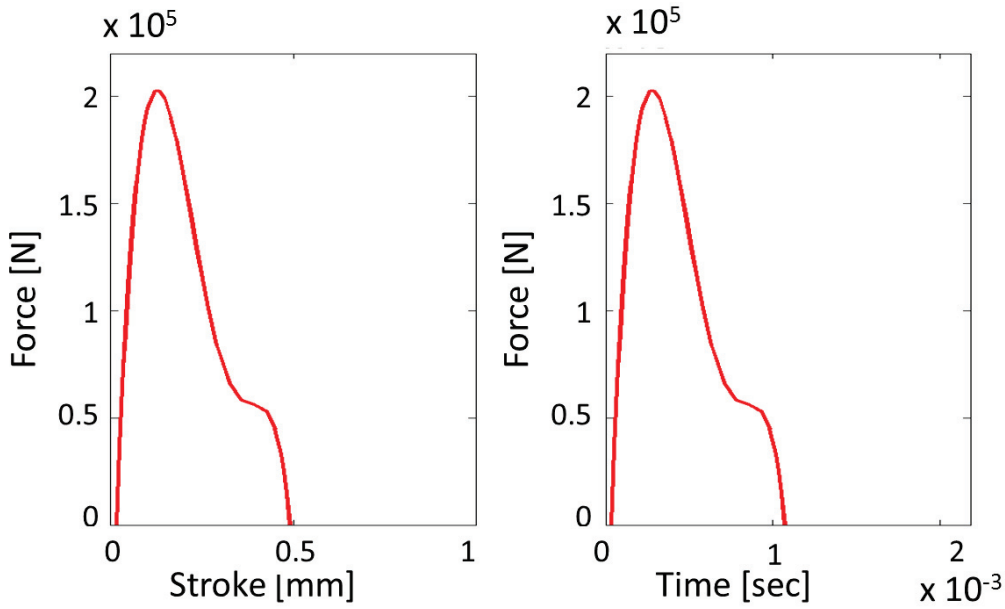

Figure 4.3: Approximation of the force stroke and force time curve

4.1.2 Energy Content of the Stamping Process

An important parameter to characterize the impact and the energy which is induced into the ram is the cutting energy. The cutting energy is the required energy per stroke to cut through the metal sheet. The formula (4.1) is defined by the integral of the cutting force F_C times the travelled distance s the tool makes when cutting through the sheet [63].

$$W_C = \int F_C ds \tag{4.1}$$

The simplified version (4.2) of the equation mentioned above is stated in [63]. In this equation, s is the covered distance during cutting and k is a correcting factor between 0.3 and 0.5 which is compensating for the non rectangular form of the force curve. A harder material leads to a smaller and steeper force time curve and therefore to a smaller factor k. This means that a more ductile material needs more energy to be cut through [63].

$$W_C = F_C \; s \; k \tag{4.2}$$

4.1.3 Stamping Process Simulation

The scope of the simulation of the stamping process is to get a general idea of the occurring stresses and strains in the ram. The results have to be seen very critically since the final design and material of the ram are not defined yet. The represented procedure should be seen as a suggestion to design the required testing signal and has to be recalculated for a new design and material of the ram. Nevertheless the scope is to design a ram with the exact same properties as the currently used ram, regarding stiffness and ductility. The reason for this approach is to be able to guarantee the quality of the process. This justifies executing the simulation on the ram made of cast iron which is presently used as a first approximation. The ram was redrawn and strongly simplified in SIEMENS® NX 8.5 to reduce calculation time. The overall length of the ram is approximately 800 mm and its width is about 400 mm.
A finite element simulation was carried out in ANSYS® WORKBENCH 15.0. The FE analysis with the Workbench tool from ANSYS® should deliver fast and accurate results. To simulate fast dynamic processes an explicit dynamic solver was applied. The geometry of the ram was imported as a step file.

4.1.3.1 Properties of the Analysis and Meshing

As already mentioned, an explicit dynamic solver was used. This method needs greater calculation time but delivers good results for dynamic processes. The simulation time was set to 1.3×10^{-3} s and the maximal number of time steps limited to 1×10^5 steps. The time in which the force is applied is about 1.1×10^{-3} s. The representing ram was meshed with tetrahedra elements. This results in 122000 elements.
The material properties of the currently used ram which were applied in the simulation are listed in table 4.2.

4.1.3.2 Boundary Conditions and Loading

The following step was to specify the boundary conditions. Since a worst case scenario was rebuilt, the mounting of the ram was assumed to be perfectly rigid. This means that all applied forces have to be compensated by the ram. The rigid support was implemented on the bores of the ram, where the ram is mounted to pushing rods of the driving system. The ram was fixed in all three translational directions whereas the rotatory movement around the center of the bore was allowed.

Material Properties:	
Young's modulus	$2 \times 10^5\,\mathrm{N/mm^2}$
Poisson's ratio	0.28
Density	$7200\,\mathrm{k/m^3}$
Tensile ultimate strength	240 MPa
Compressive ultimate strength	820 MPa
Constant damping ratio	0.001

Table 4.2: Material properties of the ram for the FEM simulation

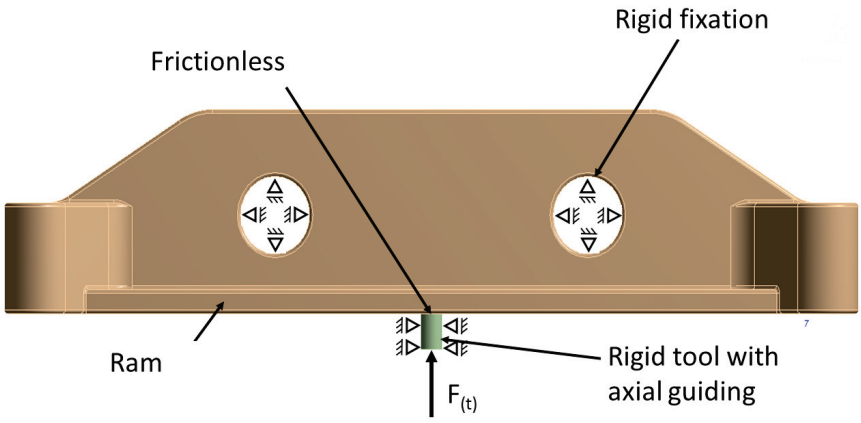

Figure 4.4: Configuration of the tool and the ram

Furthermore the tool was chosen to be a small cylinder with a diameter $d = 20\,\mathrm{mm}$ and was placed touching the downward facing surface of the ram. The connection of the ram and the tool was assumed to be frictionless. Also the tool was assumed to be perfectly rigid, so that all of the resulting forces are induced into the ram. In real life application the tool covers the whole width of the ram and stiffens the component. This effect is not included in this simulation. However, the force initiation on a small surface represents a tool with a small cutting area and typical results, sufficiently distanced from the force initiation area, can be expected. In close proximity of the force initiation area unrealistic high stress peaks will be observed. The simulation results around this area must be seen critically or neglected for further investigations.
The mentioned configuration should result in strains and stresses, which are hardly ever reached in real life applications. Nevertheless the ram should be able to withstand these loads over its whole lifetime. The tool was radially secured to avoid any lateral displacements. The final configuration of the system can be seen in figure 4.4. The force time data were loaded into Ansys and applied on the tool. The outcome of the simulation is represented in chapter 4.1.3.3

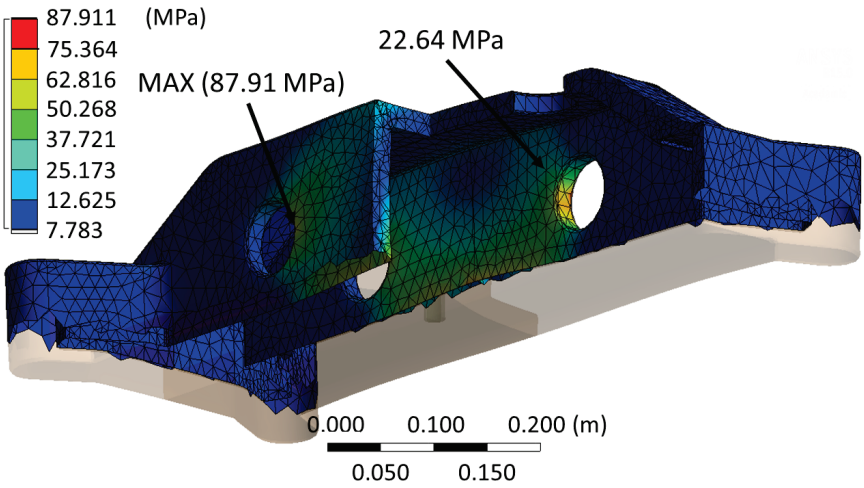

Figure 4.5: Resulting Mises stresses in the ram

4.1.3.3 Results

The results of the FEM simulation showed good agreement with expectations and, apart from the force initiation area, essentially no unexpected results appeared. For the further analysis of the results only the upper part of the ram was examined to avoid stress peaks derived from force initiation on the small area. As already mentioned this assumption is justified because the mounted tool usually has an additional stiffening effect which significantly reduces the strains in this region of the ram.

In figure 4.5 the resulting Mises stresses are represented after 5.655×10^{-4} sec simulation time. At

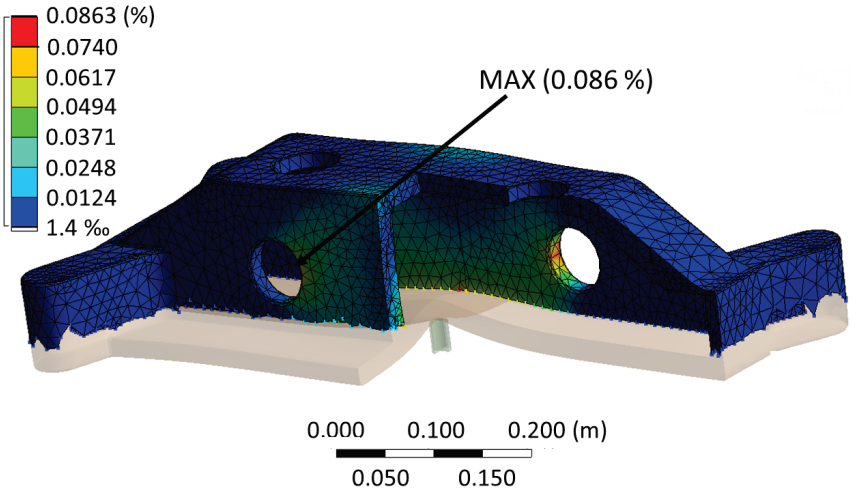

Figure 4.6: Mises strains in the ram

this moment, the stresses did already distribute from the downward facing surface to the whole ram. The locations of the maximal occurring stress is pointed out in figure 4.5 and reaches 87.91 MPa. The maximum occurs at the rigid fixations and can be accredited to numerical effects. Neglecting

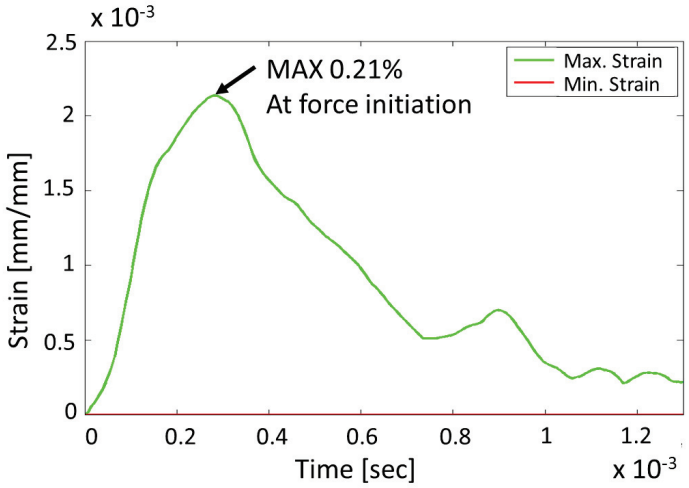

Figure 4.7: Maximum strain sequence in the ram

the outstanding stress peaks at the supports, most of the ram experiences stresses in a range between 20 MPa and 40 MPa. The moment of the maximal occurring stress correlates with the time at which the maximal force is applied and results in 168.75 MPa near the force initiation area. As already mentioned the small force initiation may result in good approximations in the residual ram, however the proximity to the force initiation must be neglected.
The same analysis was then examined for strains which are also calculated using the von Mises

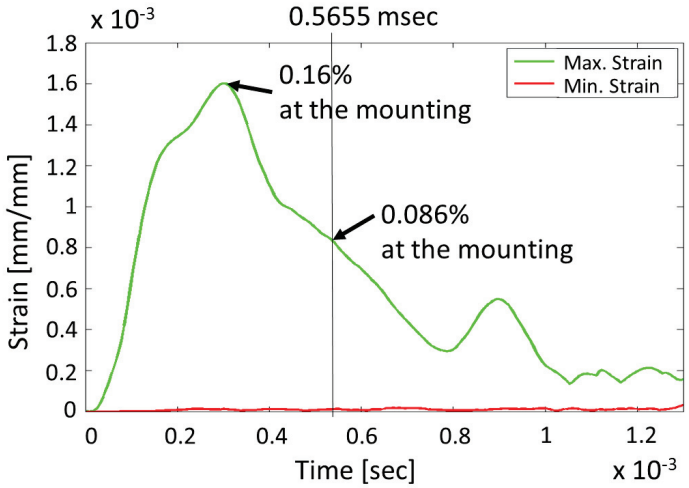

Figure 4.8: Progress of strains excluding the close proximity of the force initiation

criterion. Figure 4.6 shows the strain distribution in the ram after 5.655×10^{-4} s. Figure 4.7 on the other hand shows the sequence of the maximal strains in the ram whole ram. The maximal strain was observed with 0.21 % corresponding with the location of the maximal stresses near the force initiation area. Neglecting the close proximity of the force initiation area the maximal occurring strain was 0.16 %, also located at the mounting of the ram. The strain sequence in figure 4.8 always shows the maximal strain in the area marked in figure 4.6. These peaks may be

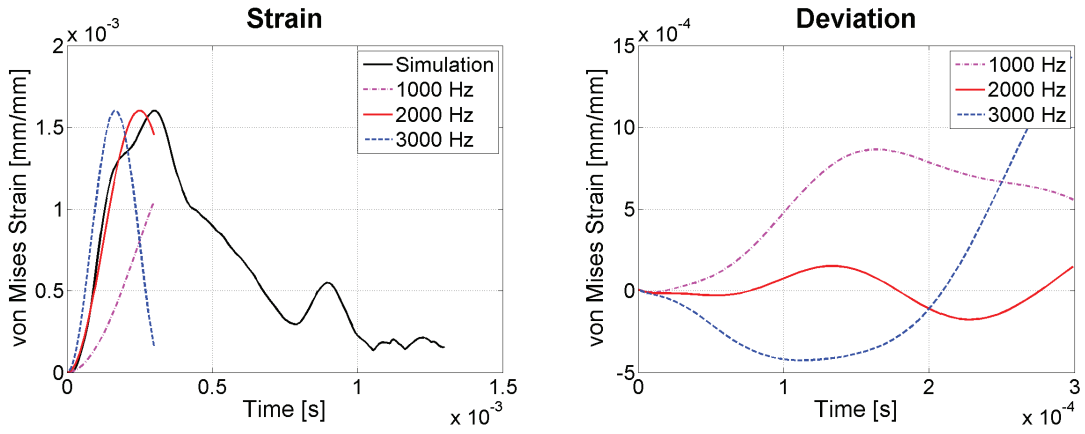

(a) Strain sequence (b) Deviation

Figure 4.9: Strain sequence of the simulation for the inner lateral side and of the testing signals

derived from numerical effects and have to be seen critically. Further a newly designed CFRP ram will have steel inlets for the mounting to the pushing rods. This will also lead to an completely different behaviour at these sections. The material in the ram, ignoring again the outstanding peaks, is exposed to strains ranging from 0.02 % to 0.05 %. This leads to the conclusion that for the designing of the composite ram, an approximate strain of 0.1 % is desirable and possible. From the strain sequences shown in figure 4.7 and 4.8 further investigations on the acting loadings in the material can be made. Strain rate and strain acceleration are important influencing parameters which can be calculated from this information. The process of derivation for these parameters is explained in the following.

4.1.4 Representation of the Load

The correct representation of the load should connect the real life event and the testing procedure. The scope is to generate a testing signal which simulates the real life loadings as closely as possible to provoke the same damage mechanisms to be able to make valuable life predictions. However, it has to be mentioned that the strain data derived from the simulation discussed in chapter 4.1.3, is subject to an uncertainty. Furthermore a resonant testing system only allows loading signals in sinusoidal form.
For the reasons stated above, the results from the FEM simulation were compared to possible test loadings. The resulting strain time sequence was exported and loaded into MATLAB®. 200 samples were stored during the simulated time frame of 1.3×10^{-3} s. In figure 4.9a the generated curves of the testing signals and the simulation results are represented. The black curve marks the simulation data from the strain sequence represented in figure 4.8. Assuming a strain controlled test as a testing signal, three different testing frequencies were examined, namely 1000 Hz, 2000 Hz and 3000 Hz. These reference frequencies were chosen to be applicable and reasonable values for comparison for they provide an adequate time lapse. The maximal strains are reached in a very short time. The comparison signals are plotted until they reach the maximum strain of the simulation data. This is the crucial part of the loading, since from then on the material is only unloaded. The first impression suggests to choose the 2000 Hz signal, which approximates the simulation data well. The diagram in figure 4.9b shows the deviation of the testing signals from the simulation

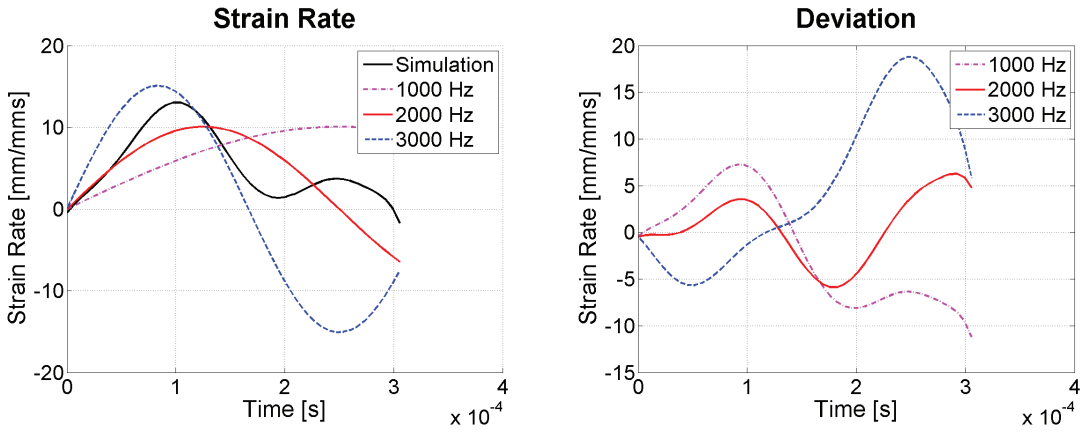

(a) Strain rate sequence (b) Deviation

Figure 4.10: Strain rate sequence of the simulation for the inner lateral side and of the testing signals

data. This deviation d is simply calculated according to formula (4.3).

$$d = \varepsilon_{Simu} - \varepsilon_f \tag{4.3}$$

Where ε_{Simu} is the strain derived from the simulation and ε_f is the according strain from the test signal. The deviation also shows good agreement for the 2000 Hz signal showing a maximal deviation of 1.5×10^{-4} mm/mm. The shape of the strain sequence describes the strain rate progress. This is the actual value the testing signal has to be designed for since the strain rate influences the damage mechanisms decisively. The next step was therefore to generate the strain rate sequence. No continuous function was available from the simulation results to calculate the derivative hence the difference quotient was used for the simulation data as stated in equation (4.4). The reference testing signals were computed in MATLAB® and the analytical derivatives were calculated.

$$\dot{\varepsilon} = \frac{\varepsilon_{i+1} - \varepsilon_i}{t_{i+1} - t_i} \tag{4.4}$$

In equation (4.4) i references to the according entry of the simulation data. The results are shown in figure 4.10a. Figure 4.10b shows the deviation of the reference signals from the simulation data.

The strain rate from the 2000 Hz signal shows very good agreement in the first part, but differs later by about ±4 mm/mms. Compared to the absolute value of ±13 mm/mms this is a significant difference. However, the strain rate is the same magnitude and approximates well in average. The damage mechanism are expected to be the same in the regarding strain rate range. The exact testing frequency will not be exactly adjustable in a resonant testing machine because there are many variables that influence the resonant frequency of the system.

Another parameter which was examined was the strain acceleration. These data were generated the same way the strain rate was calculated. Equation (4.5) describes the difference quotient for the calculation of the strain acceleration of the simulation data. The reference signals were again calculated analytically. Figure 4.11a shows the results of the calculations, whereas 4.11b describes again the deviation of the reference signals from the simulation data.

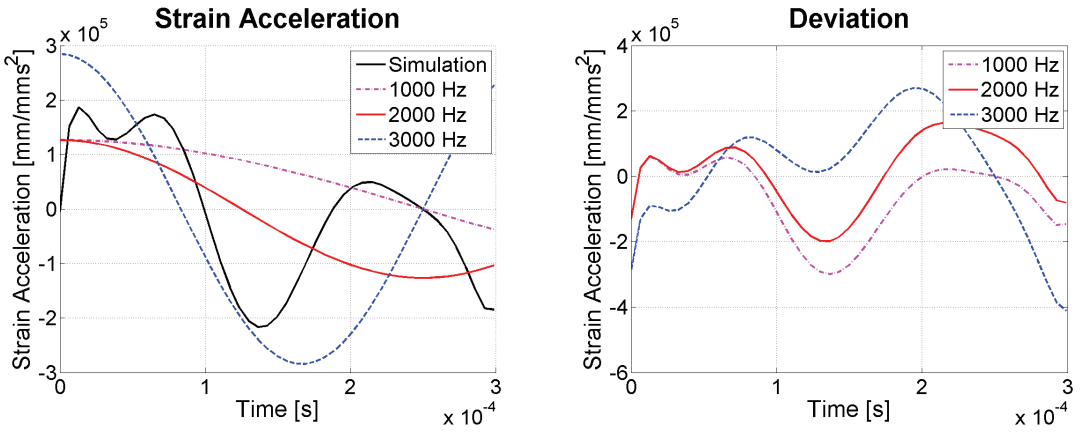

(a) Strain acceleration sequence (b) Deviation

Figure 4.11: Strain acceleration sequence of the simulation for the inner lateral side and of the testing signals

$$\ddot{\varepsilon} = \frac{\dot{\varepsilon}_{i+1} - \dot{\varepsilon}_i}{t_{i+1} - t_i} \tag{4.5}$$

The strain acceleration shows very high values as can be seen in the left hand diagram in figure 4.11a. The simulation data shows the highest value at $1.8 \times 10^5\,\mathrm{mm/(mm\,s^2)}$. The reference signal of 2000 Hz deviates strongly whereas the 3000 Hz signal shows good agreement at least for the first part. The results suggest to aim for a testing frequency ranging from 2000 Hz to 2500 Hz. In summary, it can be said that with the correct testing signal the loading can be adequately represented. Depending on the applied strain and frequency, various strain rates and accelerations can be shown. However, when testing with a resonant testing facility the sinusoidal loading is inherent to the system. Working with different signal shapes would also be interesting. For example, a triangle signal could represent a constant strain rate but will not necessarily represent the given load.
Furthermore it is important to point out that this part of the thesis is a suggestion for the design of the testing signal. A component made of CFRP will locally react differently. Especially the high damping ability of composites will influence the outcome of the FEM simulation. For linearly-elastic materials the strain rate and therefore the testing signal can directly be derived from the force time development represented in figure 4.3. It is therefore suggested that the presented proceeding has to be repeated for a CFRP ram.

4.2 Specimen Type

The specimen type is an important influencing factor to be considered. Depending on the type of loading, the fibre orientation and other parameters, CFRP reacts differently and the same material can show different results as explained in chapter 2.2. The shape of the specimen can influence and adjust various parameters as preferred. In a resonant testing machine the operating frequency range and the resulting strain amplitude strongly depends on the specific stiffness of the specimen and therefore on its length and section area. This can be useful because the adjustable specific stiffness of the specimen always allows to work in the required frequency for the piezoelectric actuator and

to represent the desired loadings [54]. Various other criteria like the repeatability, accuracy, cooling properties and boundary effects have to be contemplated also.

4.2.1 Specimen Type: ASTM D3039 Standard

The first design of the specimen was made according to the ASTM D3039 standard. Although it is said that the design of the specimen and the gripping interface is different in almost every laboratory, based on the specific material system used, the recommended geometry for the specimen is broken down into three levels [31]:

- General requirements i.e. mandatory shape and tolerances.
- Specific recommendations i.e. non mandatory suggested dimensions.
- Detailed examples i.e. non mandatory typical practices.

4.2.1.1 General Requirements

The general specifications and requirements of the shape of the specimen according to ASTM D3039 are listed in table 4.3.

Depending on the type of fixture it is necessary to apply tabs on the specimen to avoid any friction influences within the specimen itself and to focus the stress peak to the middle of the specimen. The specimen's width and thickness have to be chosen so that the cross section contains an adequate number of fibres. The length of the specimen has to be a compromise between a sufficient length to avoid bending stresses caused by eccentric fixture and a short length to be more stable against buckling [31].

According to ASTM D3410 standard [64] the specimen's thickness, gage length and width are related in equation (4.6), where $E^c[MPa]$ is the longitudinal modulus of elasticity, $F^{cu}[MPa]$ the ultimate compressive stress, $G_{xz}[MPa]$ through thickness shear modulus, h the specimen thickness and $l_g[mm]$ the length of the gage section.

$$h \geq \frac{l_g}{0.9069\sqrt{(1-\frac{1.2F^{cu}}{G_{xz}})(\frac{E^c}{F^{cu}})}} \tag{4.6}$$

4.2.1.2 Spring Stiffness of the Specimen

The spring stiffness of the specimen is the proportionality factor of the applied force and the resulting elongation. The spring stiffness is a crucial property of a resonant testing system. The spring stiffness c of a component with constant cross section can easily be calculated using equation (4.7), where E is the Young's modulus in the according direction, A is the area of the stressed cross section and l is length of the unloaded specimen. Thus the stiffness of a such a component is the needed force to elongate this component for unit of distance.

$$c = \frac{E\ A}{l} \tag{4.7}$$

	Parameter	Requirement
Coupon Requirements:		
	shape	constant rectangular cross section
	minimum length	gripping + 2 times width + gage length
	specimen width	as needed
	specimen width tolerance	±1% of width
	specimen thickness	as needed
	specimen thickness tolerance	±4% of thickness
	specimen flatness	flat with light finger pressure
Tab Requirements:		
	tab material	as needed
	fibre orientation (composite tabs)	as needed
	tab thickness	as needed
	tab thickness variation between	±1% of tab thickness
Tabs:		
	tab bevel angle	5° to 90°, inclusive
	tab step at bevel to specimen	feathered without damaging specimen

Table 4.3: Specimen geometry requirements according to ASTM D3039[31]

In the beginning the dimensions of the specimen where chosen to be 1.0 mm thick, 15.0 mm wide and 100.0 mm in length. These dimensions lead to a spring stiffness of $3.14 \times 10^7\,\mathrm{N\,m^{-1}}$ assuming a Young's modulus of 2.09×10^5 MPa. This value is taken from a standard CFRP material of the ANSYS material library. The dimensions are in agreement with the ASTM D3410 standard and proofed as applicable. The mentioned material properties are used for all further investigations such as the dimensioning of the piezoelectric actuator and the vibrating system.

4.2.2 Specimen Type: Pipe Shape

Adam et al [33] suggested a pipe shaped specimen for their resonant testing facility. Several advantages can be drawn from a pipe specimen. Firstly and most importantly the surface to volume ratio is bigger, which leads to better cooling properties. For comparison a coupon specimen with a cross section of 15 mm by 1 mm and a length of 100 mm was assumed. To achieve the same volume for a pipe specimen with an inner diameter of 20 mm and the same length the outer diameter would be 20.47 mm. The surface to volume ratio would then be $2.1\,\mathrm{mm^2/mm^3}$ for the coupon compared to $8.3\,\mathrm{mm^2/mm^3}$ for the pipe. A wall thickness of circa 0.5 mm is the minimal dimension for manufacturing and to obtain representative results. Furthermore the manufacturing in all fibre

directions is no problem and no edges are present where fibre scattering can occur. However, there are no existing standards which suggest dimensions or tolerances for a pipe specimen. The general requirements and tolerances can therefore be taken from the ASTM D3039 standard described in chapter 4.2. The dimensions have to be chosen to satisfy the requirements of stiffness, good surface to volume ratio, buckling and repeatability.

Various values for the wall thickness were examined regarding their influence on the spring stiffness, the temperature behaviour etcetera. An applicable dimension was chosen to be 20.0 mm for the inner diameter and a wall thickness of 1.0 mm and 0.5 mm was used for calculations. Again, using the material properties mentioned above from ANSYS, a spring stiffness of $12.5 \times 10^7\,\mathrm{N\,m^{-1}}$ is reached for the 1.0 mm wall and $6.4\,\mathrm{N\,m^{-1}}$ for the 0.5 mm wall.

4.2.3 Fixture of the Specimen

The support of the specimen is also an essential issue. Especially when the specimens are loaded with compression stresses and the strain measurement is applied externally. When testing with a piezoelectric actuated resonant system, the specimen holder is part of the oscillating system and has to be included in the eigenvalue analysis. Freitas et al [65] use a solid metallic specimen with an axis symmetrical hourglass form and recommend to connect actuator, booster, horn and specimen with a screwed connection.

Since the specimen shape according to ASTM D3039 are coupons, a screwed solution is basically eliminated. Generally gripping methods are recommended. However, at high frequencies a smaller and lighter solution such as glueing is also possible. When using gripping methods, low gripping pressures are desirable to avoid grip failures [2]. Therefore glueing would seem to be the preferable solution. Glueing the specimen directly into the horn and the counter mass makes it difficult to remove it after finishing the test. Also the strain measuring technique has to be considered. Assuming that the strain is measured from the difference of the travelled distances of the two masses, it has to be guaranteed that all components and fixations are sufficiently stiff compared to the specimen so that only the specimen is strained. This problem could be avoided when using for example digital image correlation as a measuring technique. This means a gripping method for fixing the specimen into the moving masses is preferable for this specific set up, mainly for two reasons: The fixation is sufficiently stiff and the specimen can easily be removed and exchanged. It has to be considered that a gripping method requires tabs or a wall strengthening at the clamped zone.
After several simulations considering the thermal, resonant and general mechanical behaviour the coupon shaped specimen was rejected and a pipe shaped specimen was preferred for reasons mentioned above.

4.2.4 Heat Generation and Temperature Distribution

The heat generation in the specimen due to the lost energy from the visco-elastic behaviour is one of the major concerns for a high frequency testing facility. Especially for materials with low thermal conductivities the internal heat generation can lead to a significant rise in temperature and will strongly affect the testing results. Various specimen geometries were examined regarding their heat transfer and cooling properties and a reasonable solution is presented. Figure 4.12 shows the qualitative heat flux in the specimens. $+\dot{q}$ represents the internal heat generation whereas $-\dot{q}$ stands for the dissipated heat energy from the surrounding medium. It is impossible to make an

exact statement since the heat generation, heat conduction and heat transfer highly depends on the specific material properties. Obviously the testing facility should be able to test various materials. For this reason it is intended to rebuild a scenario with supposable high damping factors to generate a high temperature rise. This should give an idea of the temperature conditions in the specimen. Furthermore the necessity of any additional cooling can be assessed.
The transient temperature proceeding is calculated using a FE analysis with ANSYS®. In the

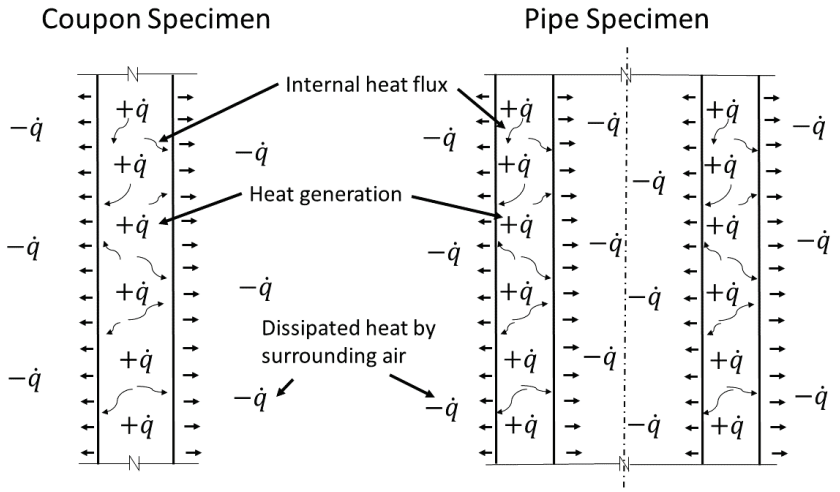

Figure 4.12: Heat flux and heat transfer in a coupon specimen and a pipe specimen

analysis the specimen is assumed to be heated uniformly on the inside and was cooled down at the outer surfaces. The material was chosen to be orthotropic to make the calculation effort reasonable. The material data is represented in table 4.4. The generated heat is due to the lost energy from

Simulation Parameters:	
Density ρ	$1.54 \times 10^{-9}\,\mathrm{kg\,m^{-3}}$
Specific heat capacity	$800\,\mathrm{J\,kg^{-1}\,K^{-1}}$
Thermal conductivity in fibre direction	$5.0\,\mathrm{W\,m^{-1}\,K^{-1}}$
Thermal conductivity orthogonal to the fibre direction	$0.5\,\mathrm{W\,m^{-1}\,K^{-1}}$
Loss modulus	$1.0 \times 10^{9}\,\mathrm{N\,m^{-2}}$
Occurring strain	$0.001\,\mathrm{mm\,mm^{-1}}$
Testing frequency	2000 Hz

Table 4.4: Simulation parameters for the heat problem

the applied strain as explained in chapter 2.1.3. According to equation (2.6) the generated thermal energy increases with the loss modulus and the square of the strain. Equation (2.6) gives the Energy per cycle and per unit volume ΔE in $\mathrm{J\,m^{-3}}$. The calorific potential $\dot{q}$ is then given by equation (4.8), where f is the frequency.

$$\dot{q} = \Delta E * f \tag{4.8}$$

Inserting the values from table 4.4 the lost energy according to (2.6) is:

$$\Delta E = \pi E'' \varepsilon_0^2 = 3141.6\,\mathrm{J\,m^{-3}} \tag{4.9}$$

Multiplying the lost energy ΔE with the applied frequency f results in the calorific potential $\dot{q}$:

$$\dot{q} = \Delta E * f = 6.283 \times 10^6\,\mathrm{W\,m^{-3}} \tag{4.10}$$

The calorific potential stated in (4.10) is the generated heat per unit volume which is induced into the specimen, where a strain of $0.001\,\mathrm{mm\,mm^{-1}}$ occurs. In the simulation the generated energy was applied over the whole specimen which implies that the specimen is strained equally over the whole length.

The examined heating problem is a transient problem and is solved in the FEM solver ANSYS®. The material properties are taken from table 4.4 and the internal heat generation is equal to the calorific potential from equation (4.10). Different specimen shapes were then simulated and the results were compared.

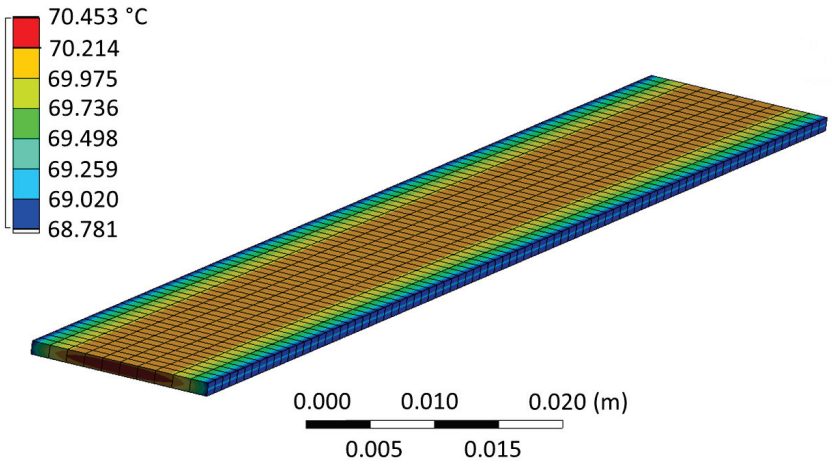

Figure 4.13: Temperature distribution in the coupon specimen after 10 sec for $\alpha = 10.0\,\mathrm{W\,m^{-2}\,K^{-1}}$

4.2.4.1 Coupon Specimen

To begin with the coupon specimen according to ASTM D3039 standard was simulated. The same dimensions as mentioned in chapter 4.2.1.1 were used. The fibre orientates along the long edge of the specimen. This means that the smaller thermal conductivity is orientated to the larger surfaces which leads to bad conditions for the heat transfer. Initially the temperature of the specimen is at room temperature at 22.0 °C and so is the temperature of the surrounding air. As a heat transfer coefficient α from the specimen surfaces to the surrounding air a value of $10.0\,\mathrm{W\,m^{-2}\,K^{-1}}$ was found to be reasonable for free convection. For forced convection a heat transfer coefficient α of up to $100.0\,\mathrm{W\,m^{-2}\,K^{-1}}$ can be reached [66] [67].

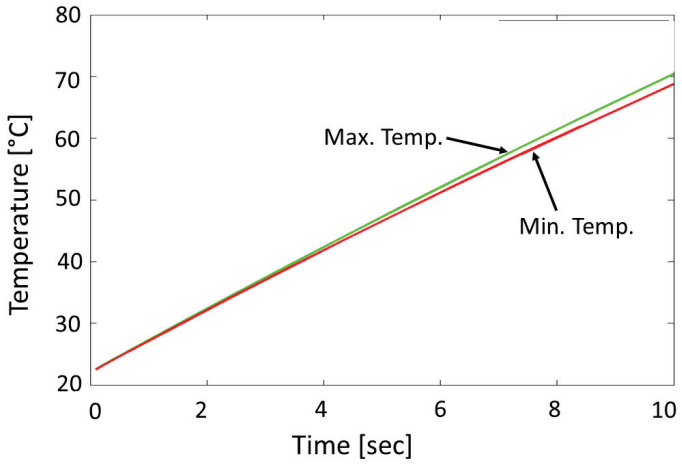

Figure 4.14: Temperature development in the coupon specimen after 10 sec for $\alpha = 10.0\,\mathrm{W\,m^{-2}\,K^{-1}}$

In addition, to achieve better cooling results the surrounding air can be cooled down before forcing it over the specimen's surface. The simulation was ran for 10 sec and the results for the first simulation with a heat transfer coefficient of $10.0\,\mathrm{W\,m^{-2}\,K^{-1}}$ are represented in figure 4.13 and figure 4.14. The temperature rises quickly and has not yet reached a steady state condition after

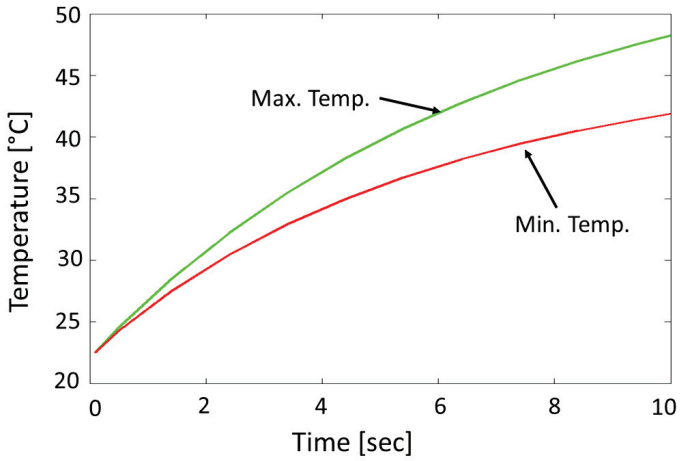

Figure 4.15: Temperature development in the coupon specimen with $\alpha = 100.0\,\mathrm{W\,m^{-2}\,K^{-1}}$

10 sec for this simulation. The core of the specimen reaches 70 °C at the end of the analysis. As mentioned, the maximum temperature variation of the specimen may not exceed 10 K during the whole test. Therefore installing a cooling system would be mandatory. The most simple solution would be to cool the specimen applying a forced fluid flow on the specimen's surface. An estimated heat transfer coefficient of $\alpha = 100.0\,\mathrm{W\,m^{-2}\,K^{-1}}$ is assumed for the second simulation. Again the surrounding fluid is at room temperature 22.0 °C. This correspondents with a simple fan or the like, which generates the fluid flow. Figure 4.15 shows the results of the simulation. The temperature

rise is not as critical compared to the simulation with the smaller heat transfer coefficient. However, the increase of temperature is still too high and would have an unacceptable impact on the test results. Additionally due to the higher heat transfer coefficient and the small thermal conductivity of the CFRP a larger temperature gradient is observed, as seen in 4.15 where the highest and lowest temperatures in the specimen are represented respectively. Though it is no critical gradient, every tested system should be checked for their behaviour to develop temperature gradients to avoid additionally induced thermal stresses.
Further simulations with the coupon shaped specimen were executed but no satisfying results were

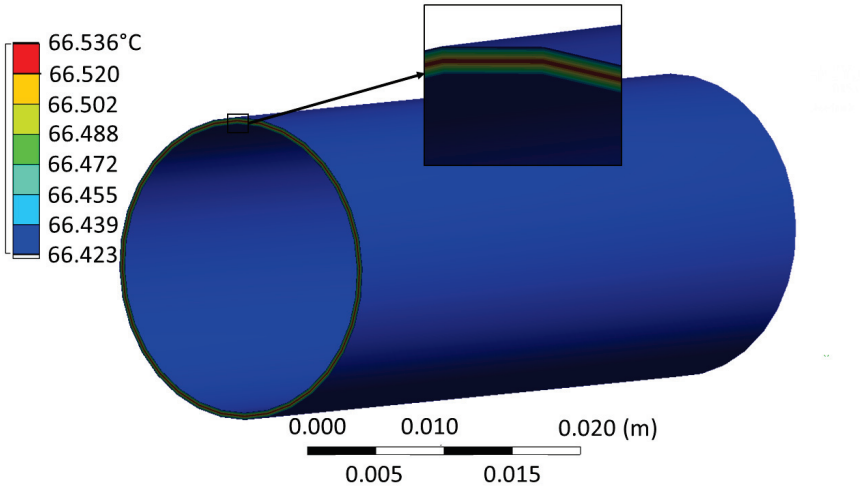

Figure 4.16: Temperature distribution in the pipe specimen ($d_i = 20\,\text{mm}, t = 0.5\,\text{mm}, l = 60\,\text{mm}$) after 10 sec for $\alpha = 10.0\,\text{W}\,\text{m}^{-2}\,\text{K}^{-1}$

observed. To keep the specimen within the desired temperature range, an extensive cooling device must be installed.

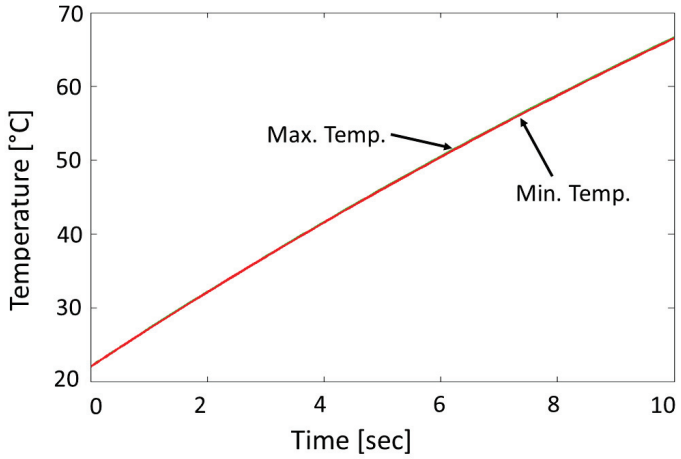

Figure 4.17: Temperature development in the pipe specimen ($d_i = 20\,\text{mm}, t = 0.5\,\text{mm}, l = 60\,\text{mm}$) with $\alpha = 10.0\,\text{W}\,\text{m}^{-2}\,\text{K}^{-1}$

4.2.4.2 Pipe Specimen

After the unsatisfying results from the coupon specimen, the pipe specimen was simulated to be heated internally. Different dimensions of the pipes were examined. The fibres for all simulations were orientated axially for the same reasons as mentioned above. With the special geometry of the specimen it would be technically possible to apply a liquid cooling on the inner surface. However, a liquid cooling should be avoided due to its influence on the damping properties of the system and on the material properties. Various thermal conductivities were simulated for the specimen's surfaces.
The first specimen which was tested had a length $l = 60\,\text{mm}$, an inner diameter of $d_i = 20\,\text{mm}$ and

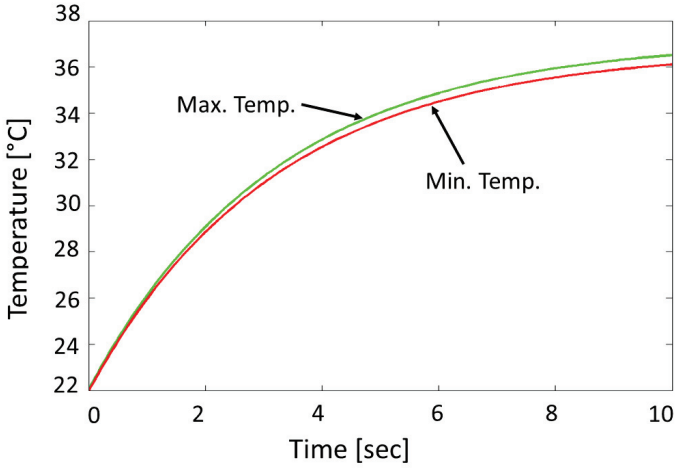

Figure 4.18: Temperature development in the pipe specimen ($d_i = 20\,\text{mm}, t = 0.5\,\text{mm}, l = 60\,\text{mm}$) with $\alpha = 100.0\,\text{W}\,\text{m}^{-2}\,\text{K}^{-1}$

$t = 0.5\,\text{mm}$ wall thickness. For the first simulation the heat transfer coefficient was assumed to be $\alpha = 10\,\text{W}\,\text{m}^{-2}\,\text{K}^{-1}$ which led to the results shown in figure 4.16 and figure 4.17.
For comparison, it should be pointed out that the mentioned dimensions lead to a total volume of $V = 1930\,\text{mm}^3$ compared to $V = 1500\,\text{mm}^3$ of the coupon specimen. The dimensions were chosen to be applicable in the testing device. The larger volume implies a higher energy generation. The observed results do not significantly deviate from the coupon specimen despite the larger surfaces. The reason for the small difference in the temperature behaviour is due to the small heat transfer coefficient. The generated heat can't get out of the specimen. Subsequently another simulation was executed for the same specimen and higher heat transfer coefficients which resulted on the outcome represented in figure 4.18. Compared to the coupon specimen, the maximal occurring temperature is approximately 30 °C lower than before. Additionally, thanks to the thin wall thickness, there is no significant temperature gradient.

4.3 Setup and Structure of the Testing Machine

After a profound research of the state of the art regarding high frequency fatigue testing, a possible solution to represent the loading and especially the high number of load cycles was chosen to be

a piezoelectric driven resonant testing facility. The desired testing frequency ranges from 1.5 kHz to 3 kHz. In chapter 3.3.1 the main components needed for a piezoelectric driven test facility are listed. Based on these guidelines the general parts for the testing machine are:

- A power generator which also transforms the provided 50 Hz voltage signal to the desired frequency of the sinusoidal electrical signal. Preferably the frequency should be adjustable between 1.5 kHz and 5 kHz.
- A piezoelectric device which transforms the electrical signal into mechanical movement i.e. displacement to generate the mechanical stresses in the specimen.
- To reach the desired strains in the middle of the specimen a reasonable and adequate mass and stiffness combination must be found.
- A control unit to secure various parameters like strain, resonant frequency and the overheating of the specimen.
- A cooling system to cool the piezoelectric actuator as well as the specimen.

According to this general listing of devices and problems the test stand is built up step by step. The whole testing system is complex and all parts have to be carefully adjusted to another to provide a reliable and accurate testing machine.

4.3.1 Resonant System

The resonant system is actuated by the piezoelectric actuator. The correct dimensioning of every single component is important to acquire accurate results. Depending on masses, stiffness and damping the system's resonant frequency is different and the desired forces to excite a certain strain, respectively displacement are varying. In the following section two approaches to analyse the influence of the respective parts and to find a good calibration of the parameters, are represented.

4.3.1.1 State Space Model

To begin with, a simple mathematical model of the test stand was designed. The oscillating system was represented with a two - mass - spring - damper model which is excited by a sinusoidal force. A schematic diagram is shown in figure 4.19. The mass m_1 is the excited mass and represents the booster horn, whereas the spring and the damper, described by stiffness c and damping factor d, are representatives for the CFRP specimen. The mass m_2 is a counterweight, which should help to reach the desired strains, adjust the whole system as required and to reproduce the same testing frequency for different materials. $F_{(t)}$ is the exciting force which excites the booster horn. $s_{1(t)}$ and $s_{2(t)}$ are the distances the masses make due to the exciting force.
This model can be represented using a state space model. A state space model describes a system using first-order differential equations instead of one or more n^{th} order differential equations [68]. Generally there are two equations which represent the state space system. Equation (4.11) determines the state of the system and equation (4.12) determines the output of the system. $x_{(t)}$ and $u_{(t)}$ are the state variables and the input variables respectively. In this specific case $x_{(t)}$ has to include the exciting Force $F_{(t)}$ and $u_{(t)}$ has to contain the information about the distances $s_{1(t)}$ and $s_{2(t)}$ the two masses make. The representation in matrix form presumes that the system state

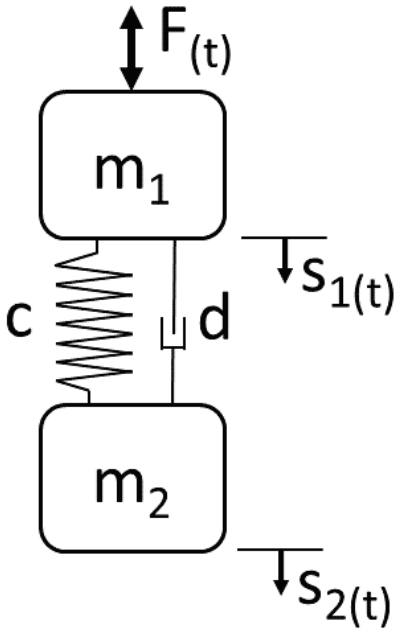

Figure 4.19: Mathematical model of a resonant testing machine

change $x'_{(t)}$ and the system output $y_{(t)}$ are linear combinations of the system state and the input vectors [69].

$$x' = Ax_{(t)} + Bu_{(u)} \tag{4.11}$$

$$y = Cx_{(t)} + Du_{(u)} \tag{4.12}$$

The matrices are described as follows [69]:

Matrix A describes how the current state affects the state change $x'_{(t)}$ and is called the system matrix.

Matrix B describes how the system input affects the state change $x'_{(t)}$ and is called the control matrix.

Matrix C describes the relationship between the system state and the system output and is called output matrix.

Matrix D is a possibility for the system input to affect the output directly and is called feed-forward matrix.

The matrices in the specific case of the above described system are stated in equation (4.13), (4.14), (4.15) and (4.16):

$$A = \begin{Bmatrix} 0 & 1 & 0 & 0 \\ \frac{-c}{m_1} & \frac{-d}{m_1} & \frac{c}{m_1} & \frac{d}{m_1} \\ 0 & 0 & 0 & 1 \\ \frac{c}{m_2} & \frac{d}{m_2} & \frac{-c}{m_2} & \frac{-d}{m_2} \end{Bmatrix} \tag{4.13}$$

$$B = \begin{Bmatrix} 0 \\ \frac{1}{m_1} \\ 0 \\ 0 \end{Bmatrix} \tag{4.14}$$

$$C = \begin{Bmatrix} 1 \\ 0 \\ -1 \\ 0 \end{Bmatrix} \tag{4.15}$$

$$D = 0 \tag{4.16}$$

The factor $\frac{1}{m_1}$ in Matrix B generates the exciting force represented by the according acceleration of m_1. The output matrix C returns the distances $s_{1(t)}$ and $s_{2(t)}$, answering the excitation. Solving the stated model in MATLAB® delivers the bode plot as well as the displacement difference between the two masses. Assuming a completely rigid system except for the specimen, the displacement difference Δl divided by the initial length l_0, gives the strain in the specimen.

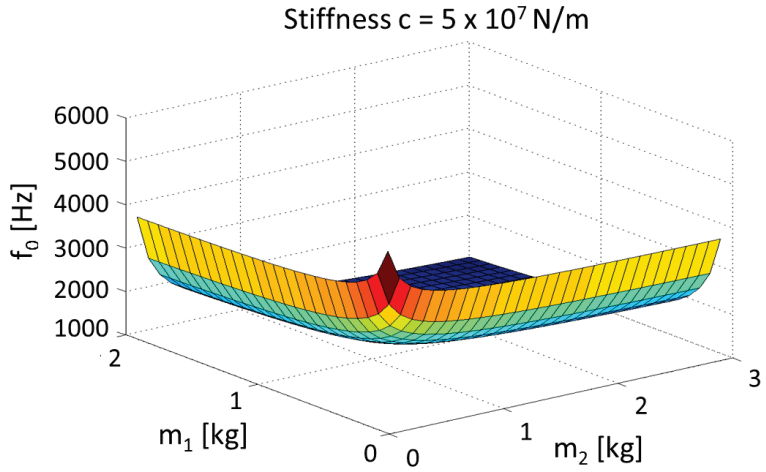

Figure 4.20: Resulting frequency for a specimen stiffness of $5 \times 10^7\,\mathrm{N\,m^{-1}}$

Results: The state space model was then used to execute a parameter study to obtain information about the influence of the respective masses and which stiffness would be ideal to operate the device in the desired frequency range. After calculating the estimated spring stiffness using equation (4.7) for several material systems and geometries, the practicable arrangements showed degrees of stiffness ranging from $5 \times 10^7\,\mathrm{N\,m^{-1}}$ to $1.5 \times 10^8\,\mathrm{N\,m^{-1}}$. The executed parameter variations are listed in table 4.5

Calculation Parameters:	
Horn mass m_1	0.1 kg to 2.0 kg
Counterweight mass m_2	0.1 kg to 3 kg
Spring stiffness of specimen c	$5 \times 10^7\,\mathrm{N\,m^{-1}}$ to $1.5 \times 10^8\,\mathrm{N\,m^{-1}}$
Damping coefficient d	450 N sec /m
Initial length l_0	60 mm
Amplitude of the exciting sinusoidal force F_A	1000 N

Table 4.5: Assumed parameters for the state space model

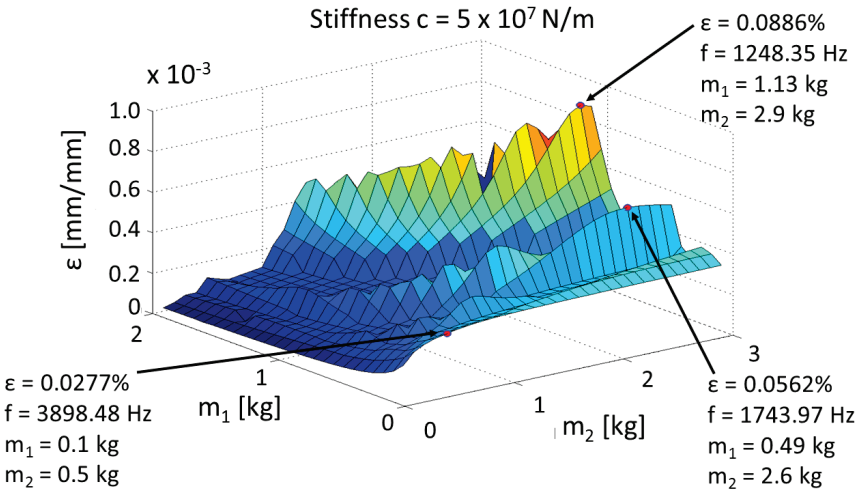

Figure 4.21: Resulting strain for a specimen stiffness of $5 \times 10^7\,\mathrm{N\,m^{-1}}$

The results are displayed in a surface plot, where m_1 and m_2 are represented on the $x-$ and $y-$ axes and the strain or the natural frequency of the particular system are assigned to the $z-$ axis. For a specimen stiffness of $5 \times 10^7\,\mathrm{N\,m^{-1}}$ this leads to the results shown in figure 4.20 for the frequency and in figure 4.21 for the resulting strain. As expected, the natural frequency of the system increases with smaller masses. A fact which is worth mentioning is that reducing only one of the two masses also results in high resonant frequencies. For example, if the horn mass is adequately reduced, the counterweight can be increased to induce higher strains into the specimen. Figure 4.21 shows the strain response to a mass variation. In the figure three values are pointed out: the maxima of the whole field, the maxima for the horn mass $m_1 < 0.8\,\mathrm{kg}$ and the maxima for the masses $m_1 < 0.5\,\mathrm{kg}$ and $m_2 < 0.5\,\mathrm{kg}$. The maximal obtained strain with this arrangement is $\varepsilon = 0.000\,88\,\mathrm{mm\,mm^{-1}}$ which is close to the desired strain in the fatigue tests which will be

$\varepsilon = 0.001\,\text{mm/mm}$.
As already mentioned the amplitude of the exciting force in this model is $F_A = 1000\,\text{N}$ and can easily be increased up to $F_A = 4000\,\text{N}$. The resonant frequency for the maximal strain is only $f = 1248\,\text{Hz}$ and is significantly under the requested testing frequency of circa $f = 2000\,\text{Hz}$. The peak in the second field for $m_1 < 0.8\,\text{kg}$ reaches a strain of $\varepsilon = 0.000\,56\,\text{mm/mm}$ at a frequency of $f = 1744\,\text{Hz}$ and would therefore lie in an imaginable range. For reaching these results the horn mass has to be $m_1 = 0.5\,\text{kg}$ and the counterweight should be around $m_1 = 2.6\,\text{kg}$. The last pointed out value produces a resonant frequency of $f = 3898\,\text{Hz}$ with a strain of $\varepsilon = 0.000\,28\,\text{mm/mm}$ and leads to the conclusion that also for high frequencies the requested strain could be induced.
Figure 4.22 shows the strain response for a specimen stiffness of $c = 10 \times 10^7\,\text{N m}^{-1}$ and as expected it shows a similar shape of the plot with generally higher resonant frequencies but smaller strains. The marked peaks are again in the same mass ranges as mentioned above. The second peak with a strain of $\varepsilon = 0.000\,30\,\text{mm/mm}$ at a frequency of $f = 2241\,\text{Hz}$ is again a desirable result, assuming an increase of the exiting force by the factor of 3.

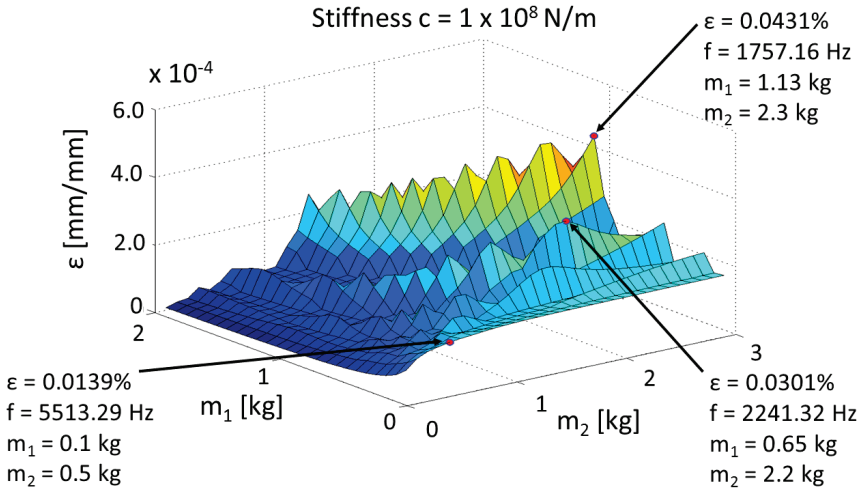

Figure 4.22: Resulting strain for a specimen stiffness of $10 \times 10^7\,\text{N m}^{-1}$

4.3.1.2 Modal Analysis using FEM

After getting a general idea of the weight distribution, a model was build in SolidWorks® to test three different arrangements which were examined for natural frequencies and occurring strains using a FE analysis in Ansys® Workbench. The reason for this analysis was to verify the results from the mathematical model explained above and to specify reasonable specimen geometries. For the simulation simple pipe specimens were used with point masses attached to their ends as seen in figure 4.23. The dimensions of the inner diameter d_i, outer diameter d_o, length l_0 and the resulting stiffnesses are displayed in table 4.6. Two different Young's moduli were chosen as reference which can be seen in table 4.6. A material with a higher modulus is basically more interesting for the application since a highly stiff structure is required. However, the testing device should not be restricted to high modulus materials. For the mathematical model, a damping factor of 450 N sec /m was chosen, which translates approximately to a constant damping ratio of 0.04 for the FE analysis.

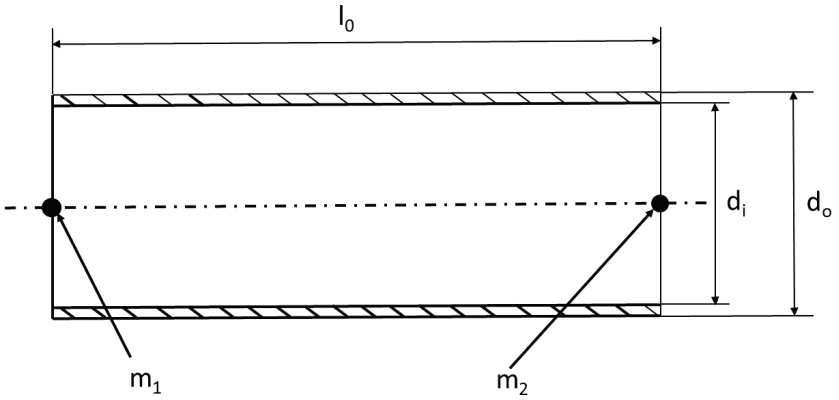

Figure 4.23: Set up of specimen and masses for FEM simulation

	Specimen #1	Specimen #2	Specimen #3
Young's modulus	2.09×10^5 MPa	1.21×10^5 MPa	2.09×10^5 MPa
Inner diameter	20.0 mm	20.0 mm	25.0 mm
Outer diameter	21.0 mm	21.0 mm	26.0 mm
Wall thickness	0.5 mm	0.5 mm	0.5 mm
Strained length	60.0 mm	60.0 mm	60.0 mm
Stiffness according to equation (4.7)	112 070 N mm^{-1}	64 570 N mm^{-1}	139 530 N mm^{-1}
Stiffness calculated using FE analysis	112 200 N mm^{-1}	64 960 N mm^{-1}	139 560 N mm^{-1}

Table 4.6: Dimensions and the corresponding stiffness of the examined specimens

To begin with, the horn mass m_1 and the counterweight m_2 were assumed to be point masses fixed rigidly to the specimen's ends. The mass arrangement was assumed to be $m_1 = 0.5\,\text{kg}$ and $m_2 = 1.0\,\text{kg}$ for the first simulations. According to the parameter study shown above, this seemed like a desirable arrangement. The results were satisfying and showed good agreement to the mathematical model.

Results: Table 4.7 lists the natural frequencies f_{Mat} and f_{FEM} and the generated strain ε_{Mat} and ε_{FEM} of the mathematical model as well as from the FEM model respectively. The exciting force is in both cases $F_{(t)} = 1000\,\text{N}$. The mathematical model's Bode plot for the displacement is shown in figure 4.24 for the specimen #1. The frequency in this plot is represented in rad/ sec and in a logarithmic scale. The first peak starting from 0 Hz is the first free eigenvalue where the whole system moves uniformly. The second peak at the longitudinal resonant frequency is also well visible and shows a strong amplification despite the high damping. The frequency range around this peak is the desired working frequency to achieve considerable amplification of the movement. The phase shift at this frequency indicates that the masses start to move counter wise which is also a desired

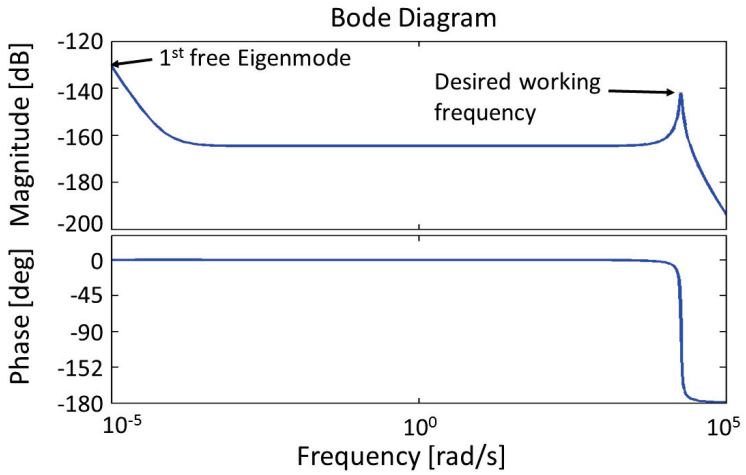

Figure 4.24: Bode plot for the specimen #1

	Specimen #1	Specimen #2	Specimen #3
f_{Mat}	2914 Hz	2220 Hz	3250 Hz
f_{FEM}	2918 Hz	2220 Hz	3254 Hz
ε_{Mat}	0.0013 m/m	0.0018 m/m	0.0012 m/m
ε_{FEM}	9.93×10^{-4} m/m	0.0019 m/m	8.8×10^{-4} m/m

Table 4.7: Resulting frequencies and strains of the examined specimens

effect to generate sufficient strains. This Bode plot is a simple and fast indication for a specific material system to get an idea at which range the desired resonant frequency lies. Additionally the transient response of the strain for specimen #1 is shown in figure 4.25 and shows that within 5×10^{-3} sec the system has reached its steady state. To compare the materials of specimen #1 and specimen #2 in their fatigue behaviour it is important to guarantee a similar testing frequency respectively strain rates. There are two practicable solutions to alter the natural frequency of a system. Either the stiffness and therefore the geometrical dimensions of one specimen are modified to obtain the same spring stiffness, or the excited masses are accordingly adjusted. Usually the same specimen dimensions are used to exclude any geometrical influences. This means that ideally the test stand should be designed to easily add or remove additional weights to adjust the natural frequency as needed. The maximum occurring strain is then simply set by altering the exciting force.

4.3.2 Design of the Testing Machine

This section shall explain the procedure of designing the particular parts and the assembly of a resonant testing device. Fixation of the specimen, weight of the components and applying the measurement systems are issues discussed in the following. Further a FE simulation of the particular design will carried out.

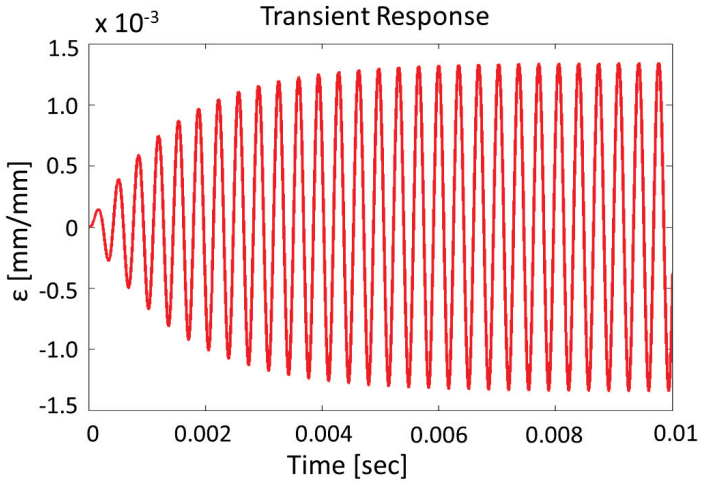

Figure 4.25: Transient response for the specimen #1

4.3.2.1 Fixing of the Specimen

Knowing the specimen's geometry being a pipe, the design of the testing device starts with a suitable fixture of the specimen. As mentioned above, there are generally two possibilities to fix the specimen to the exciting mass and the counterweight. Namely these were to glue them or to generate a frictional connection.
Designing a frictional clamp for a pipe specimen can be challenging especially when various specimen dimensions are required. It is important to generate enough force to fix the specimen rigidly to the masses, so that all strain energy is induced into the specimen's material and not into the connection.
Glueing may reduce the manufacturing effort since the necessary surface can simply be provided by the horn and the counterweight. For glued connections it is important to provide an adequately large surface to increase the strength of the connection. Figure 4.26a shows the section of the horn and the specimen where they can be bonded. The horn is designed to be hollow inside to provide sufficient cooling from the inside. A slightly larger bore, approximately 25 mm long, holds the specimen in place. The exact same system can be used for the specimen's other end at the counterweight. A major concern when glueing the specimen to the masses is that the connection may not be sufficiently stiff. The consequence is that the connection is strained instead of the specimen which will eventually lead to the failure of the connection. Assuming an indirect strain measurement using the moving masses, the connection has to be as stiff as possible to minimize the error from the strained bonding. Another disadvantage of glueing is the removal of the specimen. For further investigations the tested material should be easily removable without damaging it. One option would be an adapter to screw into the masses. This solution would require two new adapters for every new specimen. Figure 4.26b shows the second possibility to fix the specimen to the masses via a frictional connection. The specimen can easily be coupled to the masses. The pick-up element is sliced axially and wedged on the inside to press the outer surface against the inner surface of the specimen. The necessary force is provided by an inner wedge which is screwed against the pick-up element and inserted into the pick-up element before mounting it into the specimen. To tighten the connection, the pick-up element and the mass have to be twisted against each other. From the manufacturing point of view, this solution needs more effort but it is the more practicable solution

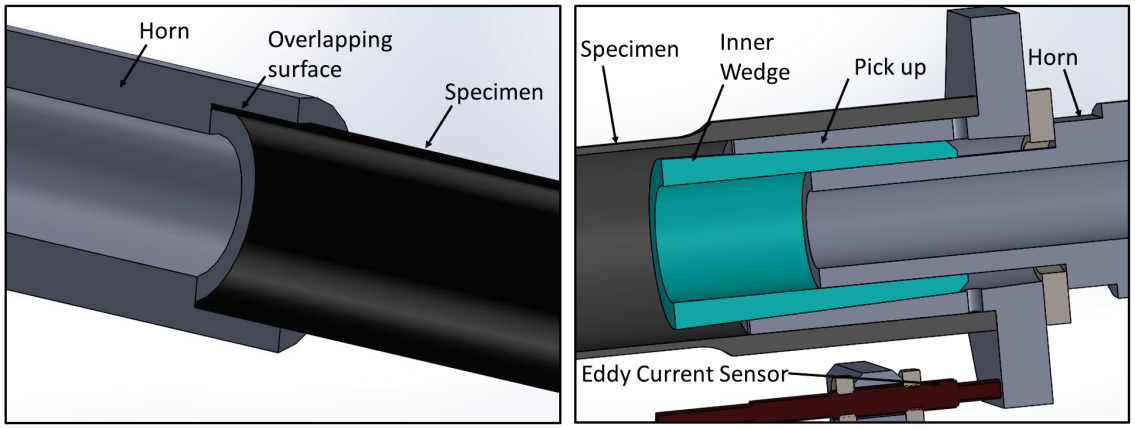

(a) Glued fixture of the specimen (b) Frictional connection of the specimen

Figure 4.26: Possible fixations of the specimen

since the mounting and removal of the specimen is fast and easily done. In addition, the overlapping surface of the specimen needs to be reinforced. This can be achieved by applying tangentially winded layers of the specimen's material. The thickness of the reinforcement should be at least 2.5 to 3 times larger than the specimen's thickness. In case of an insufficient frictional coefficient between the two materials, the connection can also be glued.
Eventually the frictional connection was chosen to be the more practicable solution and was therefore applied in the testing facility.

4.3.2.2 Horn

The design of the horn is one of the most crucial issues regarding an efficient and faultless operation. The horn is responsible to transfer the exciting energy from the piezoelectric actuator to the specimen. The horn must provide the connection to the specimen on one end and to the actuator on the other. Besides the horn must be able to generate the necessary pre-stress to prevent the actuator from working with tension stresses. The parameter study of the masses showed that the horn mass should be relatively lightweight. An optimal weight would be around 0.5 kg and additional combined weights of 0.5 kg should easily be attachable.
In the first design suggestion, as can be seen in figure 4.27, the horn has a long surface right after the connection to the specimen. On this surface an air bushing can be applied to ensure the axial alignment of the system. The same air bushing will be installed on the lower counterweight mass. The large diameter part of the horn provides space for screws to clamp the piezoelectric actuator between horn and support plate as demonstrated in figure 4.27. The actuator has to be loaded with sufficient pre-stress. The same screws can then be used to add discs as additional weight to the horn. Furthermore the horn reaches all through the piezoelectric actuator to align those two components. In the space between horn and actuator a pourable compound will be applied. The piezoelectric actuator used is a HPST 1000/35-25/40 actuator from PIEZOSYSTEM JENA GmbH. The horn has an axial through bore to provide sufficient cooling to the specimen. This horn design weighs 0.78 kg. The weight can significantly be reduced by removing the air bushing's surface and make the horn much shorter. Another disadvantage of this design is the pre-stress system. The piezoelectric actuator has to be loaded exactly axially to avoid any damages. Applying the pre-stress with this system is therefore a considerable issue. The screws in this design act as springs as

they are strained in their elastic range from the actuator and provide the tension forces to pull the system back. This means the actuator has to be strong enough to strain the screws. This implies that the screws are strained and crucially loaded. A fatigue life estimation has to be made for the screws. Alternatively every screw can be provided with a disc spring. That way the springs are going to be strained instead of the screws.

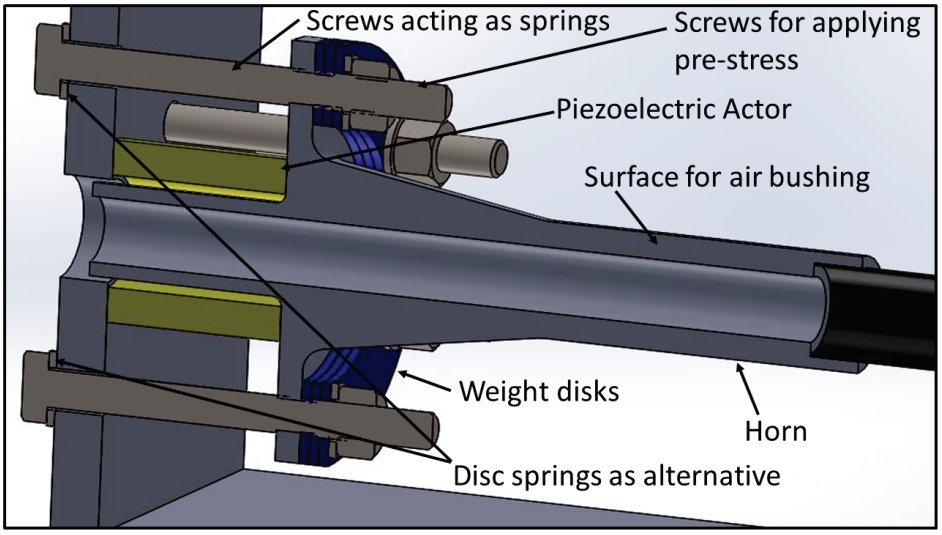

Figure 4.27: First design of the horn with the pre-stress system applied outside the piezoelectric actuator

Another negative aspect of this design is that the screws for the pre-stress would have to be separated from the screws to mount the additional weights. The separation is necessary so that the pre-stress does not have to be readjusted when an additional weight is added or removed. After facing many problems with represented design several changes were made.
A more advanced design of the horn is shown in figure 4.28. The main difference is that the pre-stress is generated through a nut mounted on the horn itself. This means that no additional screws are needed and the exact axially loading of the actuator is guaranteed. The horn itself is designed similarly to the horn above. However, in this design the parts are not secured against any rotational movement. This is especially important for the mounting and pre-stressing of the actuator. The larger diameter part is equipped with threaded bores to mount additional weights. The weight discs are cut in half for easier handling. Furthermore this design is compatible with the frictional connection. Without the surface for an air bushing this horn has a mass of 395 g. The figure shows the horn built in with the frictional connection, piezoelectric actuator, eddy current sensor and the support.
Again the inner continuous bore provides a possibility to cool the specimen from the inside. The horn itself acts as the required spring element instead of the screws as mentioned above and will therefore compensate the occurring tension forces. To guarantee a failure free operation a life estimation for the strained horn part was executed. It is also possible to place a disk spring between horn and nut to achieve a softer connection which requires smaller forces from the actuator.
The strained section of the horn is where the piezoelectric actuator applies its force. The actuator is limited by a maximum force. The used HPST 1000/35-25/40 has a blocking force of $F = 20\,\mathrm{kN}$. To ensure a long lasting operation the actuator should only be excited up to fractions of its maximum power. Therefore the section of the horn is limited by the maximal force generated by the actuator

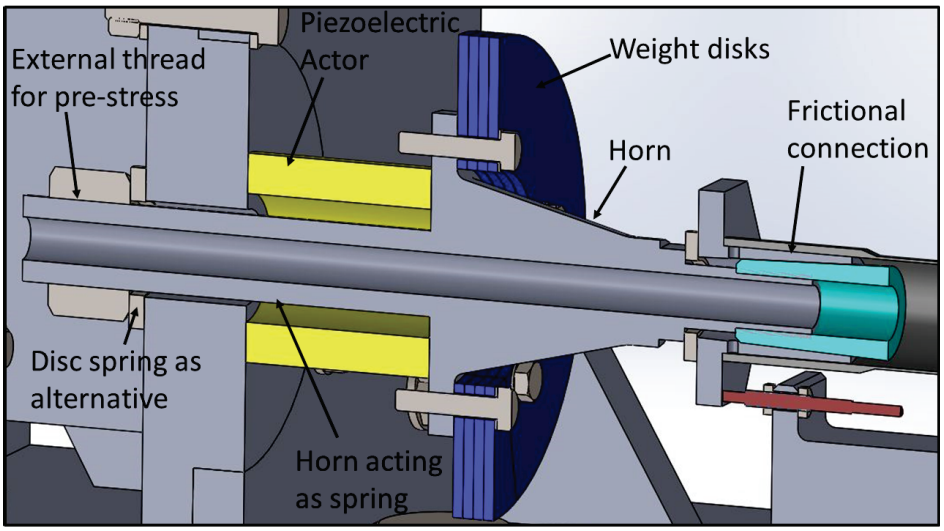

Figure 4.28: Horn design with inner pre-stress system

to achieve a certain displacement. For calculations the maximal force is assumed to be $F = 3\,\mathrm{kN}$ and the needed displacement to excite the desired strain will be around $\delta l = 5\,\mu\mathrm{m}$. The strained length of the horn will be $l_0 = 56\,\mathrm{mm}$ long. The stiffness of the horn in the section is given by equation (4.17). Assuming that the displacement will be in the elastic region, the produced force of a material strained by the displacement δl is stated in equation (4.18). Substituting c for equation (4.18) in equation (4.17) and solving for A, the maximal section is given by equation (4.19).

$$c = \frac{E\,A}{l_0} \tag{4.17}$$

$$F = c\,\delta l \tag{4.18}$$

$$A = \frac{F\,l_0}{E\delta l} = \frac{3000 \times 56}{210000 \times 0.005} = 160.0\,\mathrm{mm}^2 \tag{4.19}$$

The minimal inner diameter of the bore through the horn is then given by equation (4.20) where D is the diameter of the threaded base.

$$d = \sqrt{D^2 - \frac{4A}{\pi}} = \sqrt{14.8^2 - \frac{4 \times 160}{\pi}} = 3.5\,\mathrm{mm} \tag{4.20}$$

To ensure a sufficient cooling and to save weight, the inner bore has a diameter of $d = 8.0\,\mathrm{mm}$ and is therefore well over the minimal diameter. For comparison the needed force to strain the horn by $5\,\mu\mathrm{m}$ is stated in equation (4.21).

$$F = E\frac{\delta l}{l_0}\frac{(D^2 - d^2)\pi}{4} = 210000\frac{0.005}{56}\frac{(14.8^2 - 8^2)\pi}{4} = 2240\,\mathrm{N} \tag{4.21}$$

The pre-stress system in this case can easily be changed by mounting a disc spring between the nut and the support. With that the pre-stress system is much softer which implies smaller forces

to generate for the actuator but also for the restoring force. This is a good solution provided that the forces occurring in the exciting system are adequately small.

Fatigue Life Estimation: A fatigue life prediction was calculated based on the fact that the horn will be strained with every stroke the piezoelectric actuator makes. If no disc springs are applied, the horn has to provide sufficient pre-stress so that the actuator does not have to generate tension forces. A pre-loading force of $F_{Pre} = 10\,\text{kN}$ is applied. The piezoelectric actuator generates a sinusoidal force $F_{(t)}$ with an amplitude of $F_a = 2.5\,\text{kN}$. This leads to a pulsating compression stress of the horn. The horn will be made of structural steel S 235. The boundary conditions are summarized in table 4.8 and can be seen in figure 4.29. The effective direction of the forces F_{Pre} and $F_{(t)}$ are both to be seen exactly axially. All calculations were carried out with information from [70].

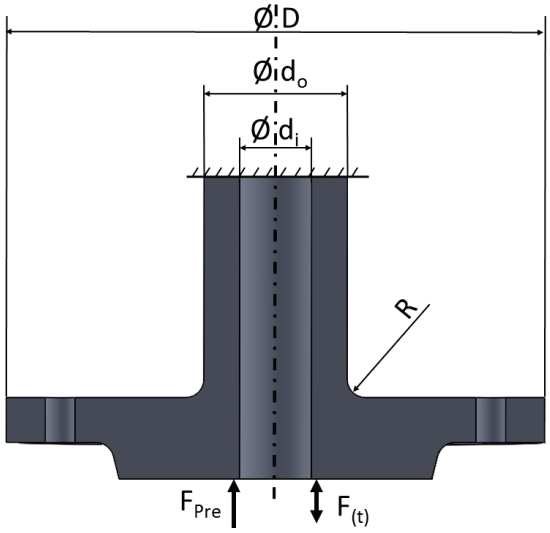

Figure 4.29: Boundary conditions for the fatigue analysis

Fatigue Life Boundary Conditions:	
Pre-loading	$F_{Pre} = -10\,000\,\text{N}$
Loading Amplitude	$F_A = 2500\,\text{N}$
Outer diameter of the stressed section	$d_o = 16.0\,\text{mm}$
Inner diameter of the stressed section	$d_i = 8.0\,\text{mm}$
Radius in the notch	$R = 2.0\,\text{mm}$
Large diameter after notch	$D = 60.0\,\text{mm}$
Material	Structural Steel S 235

Table 4.8: Fatigue Life Boundary Conditions

To begin with, the specific load case was determined. For this reason the mean stress σ_m and stress amplitude σ_a, seen in equation (4.23) and (4.24), were calculated using the acting forces F_{Pre} and F_a and the effective cross section A. The cross section is calculated in equation (4.22).

$$A = (d_o^2 - d_i^2)\frac{\pi}{4} = 150.8\,\mathrm{mm}^2 \tag{4.22}$$

$$\sigma_m = \frac{F_{Pre}}{A} = -66.3\,\mathrm{N/mm}^2 \tag{4.23}$$

$$\sigma_a = \frac{F_A}{A} = 16.6\,\mathrm{N/mm}^2 \tag{4.24}$$

The large pre-stress guarantees that the horn is always under compression stresses. The stresses will therefore always be in negative ranges. The maximum stress σ_{Max} and minimum stress σ_{Min}, stated in equation (4.25) and (4.26), are not in a critical range for plastic deformation as seen in equation (4.27) where R_{eH} is the material's yield strength and S_{Plast} is the safety factor for plastic deformation. σ_{Min} is taken for this calculation because its absolute value is greater.

$$\sigma_{Max} = \sigma_m + \sigma_a = -49.7\,\mathrm{N/mm}^2 \tag{4.25}$$

$$\sigma_{Min} = \sigma_m - \sigma_a = -82.9\,\mathrm{N/mm}^2 \tag{4.26}$$

$$S_{Plast} = \frac{R_{eH}}{\sigma_{Min}} = 2.8 \tag{4.27}$$

The next step is to define the geometrical effects on the fatigue life which is represented by the construction factor K_{Ftc} for tension and compression, stated in equation (4.28). The single elements in this equation are taken from diagrams in [70] and are explained in the following.

$$K_{Ftc} = (\frac{\beta_{ntc}}{K_g} + \frac{1}{K_{S\sigma}} - 1)\frac{1}{K_H} = 2.61 \tag{4.28}$$

To classify the influence of the notch from the diameter transition from 16 mm to 60 mm the stress concentration factor α is used which is stated in equation (4.29). For shouldered diameter changes this factor depends on the ratios of notch radius to the smaller diameter of the shaft r/d_o and of larger diameter to smaller diameter d_o/D. Further the notch sensitivity factor n is calculated in equation (4.30) where G' is the specific stress gradient and results for the mentioned dimensions in $G' = 1.22$. The notch factor β_{ntc} for tension and compression is further derived in equation (4.31).

$$\alpha_{(r/d_o=0.125;d_o/D=3.75)} = 1.9 \tag{4.29}$$

$$n = 1 + \sqrt{G'}10^{-(0.33+R_{eH}/712)} = 1.24 \tag{4.30}$$

$$\beta_{ntc} = \frac{\alpha}{n} = 1.53 \tag{4.31}$$

The next influencing factor is the geometrical size effect K_g. For tension and compression loading this factor is written in equation (4.32). Further the roughness of the surface is considered in the technical surface factor $K_{S\sigma}$. This factor depends on the surface roughness R_z and the tensile strength R_m. The component was manufactured on a turning machine so that the roughness can be assumed with $R_z = 50\,\mu\mathrm{m}$. The tensile strength for S 235 structural steel is $R_m = 340\,\mathrm{MPa}$. Equation (4.33) shows the result for this factor. K_H is the hardening effect of the surface for various surface hardening techniques. However, no surface hardening was applied so this factor results in the outcome stated in (4.34).
Given these parameters it is possible to calculate the construction factor stated in equation (4.28).

$$K_g = 1 \tag{4.32}$$

$$K_{S\sigma} = 0.93 \tag{4.33}$$

$$K_H = 1 \tag{4.34}$$

From the derived factors the design endurance σ_{DEtc} of the component can be calculated using equation (4.35). σ_{Etc} is the endurance limit for the material for a certain mean stress and is shown in (4.36). K_1 is the technological size effect and depends on the diameter the material was manufactured from. The component was turned out of a steel bar with outer diameter $d_{eff} = 70\,\text{mm}$ which results in the size effect factor stated in (4.37).

$$\sigma_{DEtc} = \frac{\sigma_{Etc}\, K_1}{K_{Ftc}} = 52.9\,\text{N/mm}^2 \tag{4.35}$$

$$\sigma_{Etc} = 150\,\text{N/mm}^2 \tag{4.36}$$

$$K_1 = 0.92 \tag{4.37}$$

With the provided information the dynamical safety factor S_{Dyn} is calculated from equation (4.38). The safety factor shows that the component is within its endurance limit and can be used as planned.

$$S_{Dyn} = \frac{\sigma_{DEtc}}{\sigma_a} = 3.2 \tag{4.38}$$

4.3.2.3 Counterweight

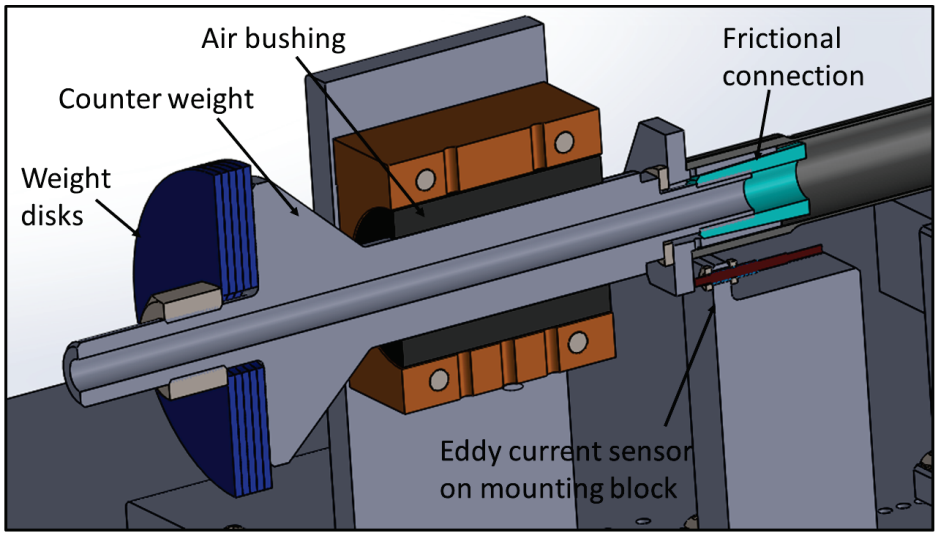

Figure 4.30: Counterweight with air bushing and additional weights

The counterweight is coupled by friction to the specimen and helps to achieve the needed strains or frequencies. The design of the counterweight should be as simple as possible and is also axially symmetric. The requirements for the counterweight are to allow an axial bearing and to mount additional weights. The counterweight is shown in figure 4.30. The lower end is equipped with

an external thread to fix the weight discs, whereas the upper end has an external thread for the frictional connection to the specimen. The long surface with a diameter of 25.0 mm allows to use an air bushing. This way it is guaranteed the system oscillates in a longitudinal mode and does not start to swing in any undesired direction. The figure shows the counterweight built in with air bushing, additional weights and frictional connection. The same measuring system is applied at the counterweight.

4.3.2.4 Assembly

The assembly shows the complete arrangement for the resonant testing system. The connecting dimensions for the large base plate are given by an available support stand. The bracket is also already available in the laboratory from earlier projects. Given these dimensions the testing machine was designed. In figure 4.31 the assembly is shown horizontally for better visibility. However, the testing device will be mounted vertically with the counterweight hanging freely.
As already shown above, the horn will be used to pre-stress the piezoelectric actuator and is

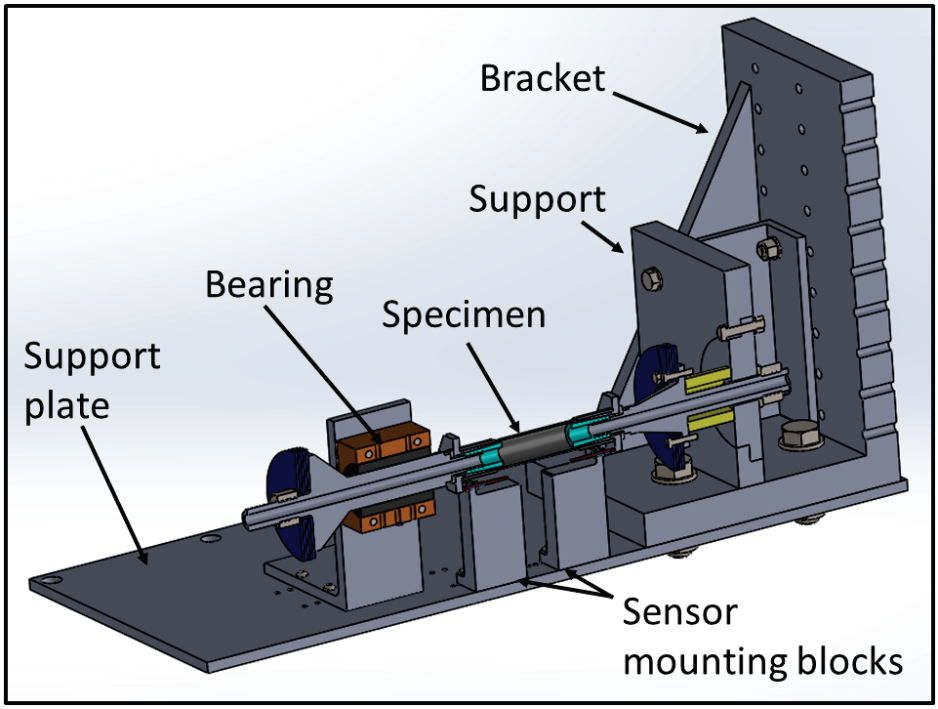

Figure 4.31: Section view of the complete assembly

therefore mounted to a support plate. The support plate is separated in two pieces which can be rotated against each other. This way the test stand can be rotated, without touching the pre-stress system. A rotation may be needed to tighten the frictional connection of the specimen. The bearing is mounted on a L-profile. If the testing stand oscillates exactly in its longitudinal resonant frequency, the bearing should not carry any load and only serves as a safeguard to avoid bending stresses. The L-profile is equipped with slotted holes for the bearing screws and with slightly larger bores to mount it to the base plate. That way the bearing can easily be adjusted for any axial misalignment. The L-profile can be mounted to the base plate in several vertical

positions to compensate changes of dimensions, for example for different specimen lengths. The sensor carriers are small aluminium blocks and have small bores to bring on the eddy current sensors. The measurement range of the applied sensor MICRO-EPSILON® U05(09) is 0.5 mm and the minimal measurable distance from sensor to object is 0.05 mm. This means that the sensors have to be mounted closely to the measuring surface. The surface against which will be measured is the surface of the outer wedge of the frictional connection. The sensor will be used also to measure the required pre-stress. Providing that the actuator has a certain stiffness the applied force can be calculated from the distance the actuator is compressed. Further the sensor is mounted with two nuts.That way the sensors are continuously adjustable for approximately 5 mm so that the sensor can be moved exactly in its optimal measuring range.

4.3.3 Determination of Eigenvalues and the Resulting Stresses

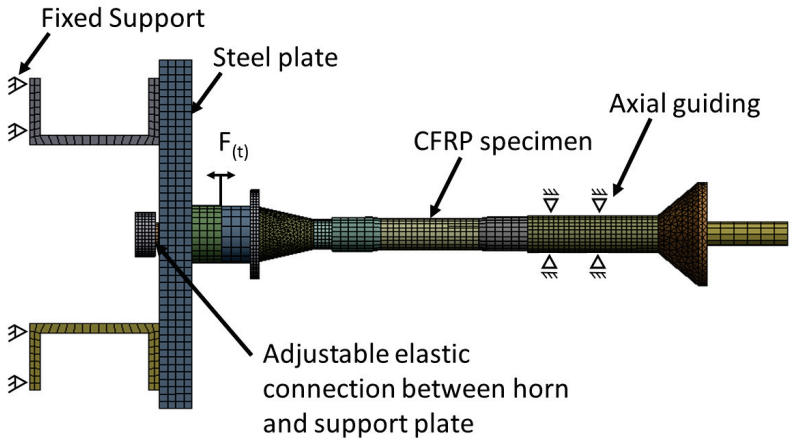

Figure 4.32: Simulated model of the testing device with boundary conditions and force initiation

The finalized test stand has to be checked for its natural frequencies. The support should not have any eigenvalues in close vicinity of the working frequency. This would cause strong vibrations of the test stand and would affect the results and stress the support structure. Furthermore the idealized two-mass system explained in chapter 4.3.1 has to be verified. The test stand should excite this particular eigenvalue. The supporting structure has to be stiff enough to act as a proper grounding and the connection between the excited mass and the support has to be softer than the specimen to achieve that mode. The stiffness of the connection from the vibrating system to the support can be adjusted by applying disc springs in a desired spring pile. The simulation was executed in ANSYS® WORKBENCH. It is assumed that the bracket and the base plate are heavy enough compared to the residual test stand, allowing them to be taken out of the simulation. The two U-profiles are fixed rigidly onto the upper surface. All connections were assumed to be rigid except for the connection between horn and support plate which was an elastic connection. The stiffness of this connection is easily changeable and can represent different sets of disk springs. The counterweight is guided axially representing the air bushing. Figure 4.32 shows the simulated system. Specimen #2 was taken into the analysis with a stiffness of 64 570 N mm^{-1}.

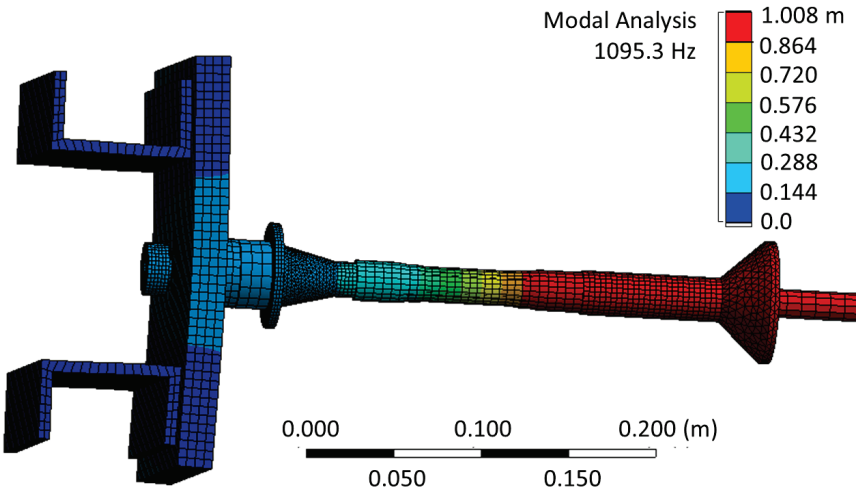

Figure 4.33: First longitudinal mode of the system (One-mass oscillator) with a highly stiff connection. The color map stands for displacement

Simulating the exciting piezoelectric actuator is more difficult. The actuator acts as an active element and does not affect the system with its stiffness but its weight will cause the resonant frequency to decrease. This problem was solved by cutting the piezoelectric element in half and oppositely applying the exciting force on those two elements. The two parts are bonded axially in order to avoid any natural frequencies from bending at this section. Only half of the piezoelectric mass is then added to the system but the results showed that its contribution is small. The connection between the support plate and the horn mass is simulated with a spring. That way the stiffness of the connection can be easily altered to show the influence of this connection.

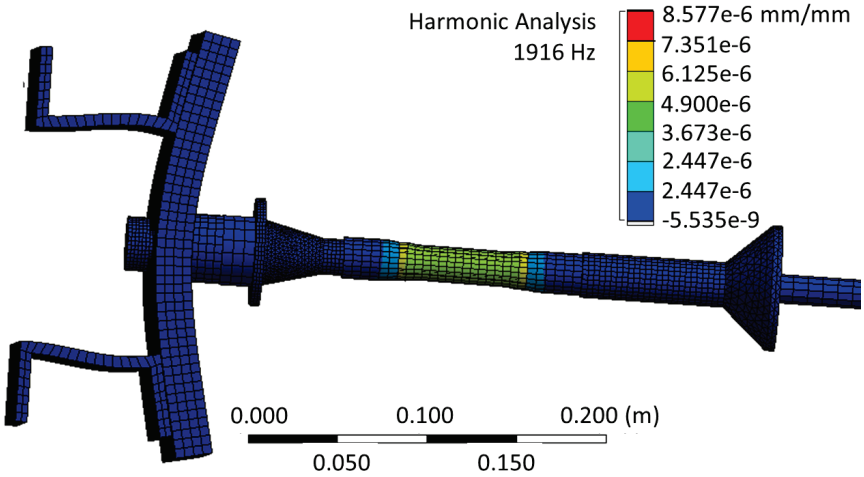

Figure 4.34: Second longitudinal mode of the system (Two-mass oscillator) with a highly stiff connection. The color map stands for strain

4.3.3.1 Stretched Horn

The first simulation was executed with the horn as the elastic element, as designed at the beginning. The elastic connection between support and horn was chosen to be as stiff as the horn itself. This is approximately $4.5 \times 10^5\,\mathrm{N\,mm^{-1}}$. The modal analysis were carried out without any damping so the results of the color map are out of proportion. The modal analysis should only deliver information about the form and frequencies of the eigenvalues. The actual deformations are further received from a harmonic simulation. The correct modal analysis is the basis for good results from the harmonic simulation. The results in figure 4.33 show the first longitudinal mode. At this mode, the system acts as an one-mass oscillator at only 1095 Hz. Furthermore the support starts to bend and consumes some of the strain energy from the specimen. The connection between oscillating system and support is too stiff. The mode where the upper mass is moving, is at 1916 Hz and is oscillating together with the bending support plate. The counterweight at this frequency hardly moves compared to the residual system. Figure 4.34 shows this excited mode.
This simulation leads to the conclusion that the support should be additionally stiffened to avoid any bending movements. However, the first longitudinal mode would be a possibility to operate the machine but it is lower than the actual required frequency.

The harmonic response for this system was analysed as well. The piezoelectric element was

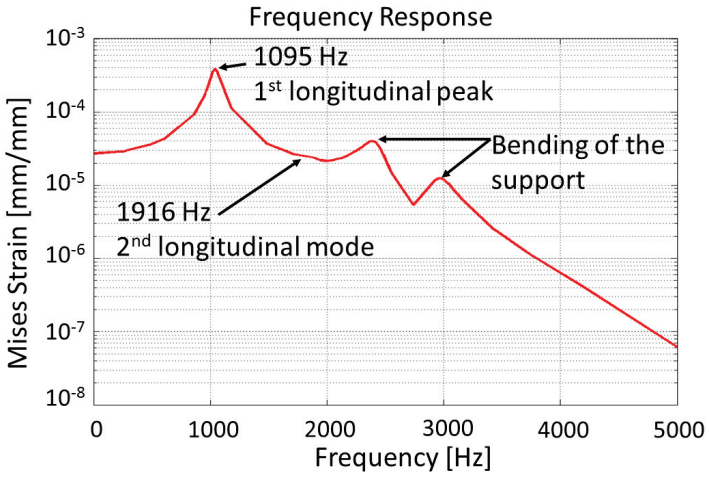

Figure 4.35: Frequency response for highly stiff connection of the system

thereby excited with a force of 1000 N on both sides. That way the actual generated forces of the actuator are represented. Figure 4.35 shows the frequency response in strain of the specimen. At 1095 Hz the first peak is the one-mass oscillator and results in a maximal strain of $3.81 \times 10^{-4}\,\mathrm{mm/mm}$ which is less than half of the required strain. The second longitudinal mode is hardly visible due to the small amplification but is pointed out in the diagram. Over 2000 Hz there are two resonant frequencies were the support bends and the counterweight stands still.

4.3.3.2 Disc Spring

In order to excite the two-mass oscillator correctly, a disc spring can be mounted to make the connection between the moving system and the support softer. To begin with, a disc spring according

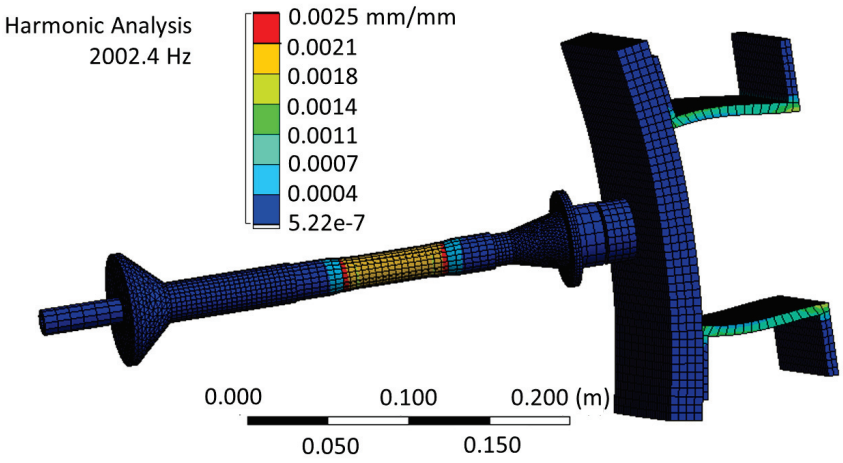

Figure 4.36: Second longitudinal mode of the system (Two-mass oscillator) with a disc spring connection. The color map stands for displacement in this diagram

to DIN 2093A was chosen with an inner diameter of 18.3 mm and 2 mm thickness which results in a spring stiffness of approximately 8000 N mm^{-1}. As expected, the first longitudinal mode showed the whole system moving together due to the much softer connection. The second mode was at 2002 Hz and induced a strain of circa 0.002 mm/mm which is twice as much as required.
Figure 4.36 shows the oscillating system. Figure 4.37 shows the frequency response of the system.

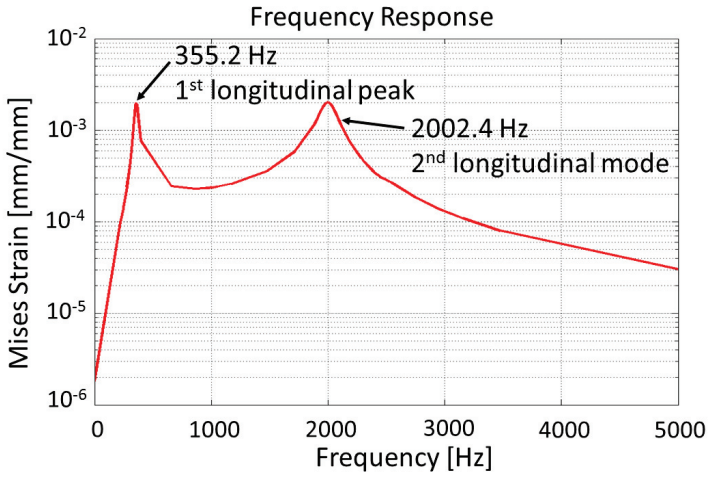

Figure 4.37: Frequency response for a disc spring connection of the system

For comparison, the spring stiffness of the connection was reduced to 500 N mm^{-1}. The frequency response, shown in figure 4.38, is similar to the previous one but the first mode is at a lower frequency. The second mode at 1946 Hz results also in similar strains but stresses the support less. The first mode lies closer to 0 Hz, which would coincide with no stiffness at all. The bode plot would then look like the one from the ideal mathematical model shown in figure 4.24.
Ideally the support plate is infinitely stiff and the connection of the moving system has no stiffness

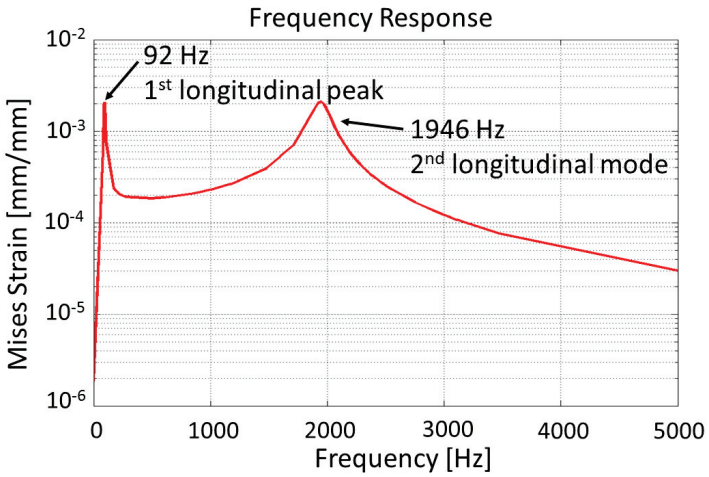

Figure 4.38: Frequency response for a very soft connection of the system

at all. This composition corresponds to the idealized mathematical model explained above. As already mentioned, the support plate and the connecting pieces should be additionally stiffened. The choice of the disc spring is a more critical issue. A soft connection would discharge the support. However, the disc spring is responsible to generate the tension forces to unload the actuator. Therefore the disc spring with an inner diameter of 18.3 mm and 2 mm thickness is chosen as a compromise. The disc spring can easily be exchanged to adjust the system if necessary.

4.3.4 Strain Measurement System

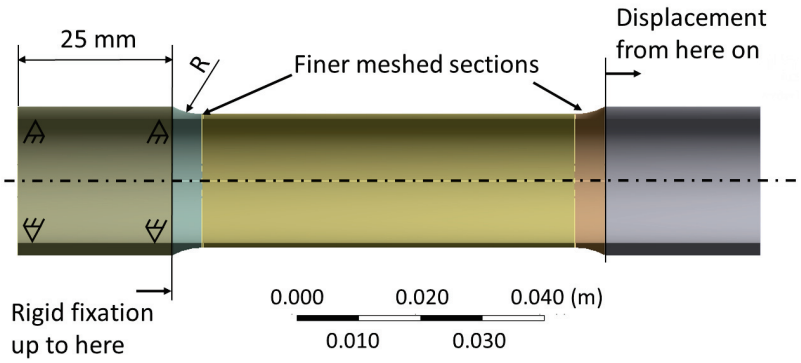

Figure 4.39: Boundary conditions and applied loads for the simulation of the strain distribution in the specimen

Two eddy current displacement sensors are used as a strain measurement system. However, they can only measure the strain indirectly, using the relative displacement of the masses. A FE analysis

was executed to validate this system. The analysis should give an idea of the strain distribution and any occurring strain peaks. The calculated strain ε from the relative displacement is calculated with equation (4.39) where x_{m_1} and x_{m_2} is the respective displacement of the horn and the counterweight and l_0 is the unstrained length of the specimen.

$$\varepsilon = \frac{\Delta l}{l_0} = \frac{x_{m_1} - x_{m_2 2}}{l_0} \tag{4.39}$$

Figure 4.39 shows the simulation's boundary conditions. It is assumed that the fixations of the specimen are perfectly rigid. In that way one side of the specimen was fixed rigidly for 25 mm. This is the length of the pick-up elements. On the other side of the specimen an uniform displacement

	Specimen #1	Specimen #2
Overall length	120 mm	120 mm
Strained length	60 mm	60 mm
Thickness	0.75 mm	0.75 mm
Transition radius	5 mm	10 mm
Calculated strain	5×10^{-5} mm/mm	5×10^{-5} mm/mm
Strain on strained length	4.81×10^{-5} mm/mm to ca. 5.60×10^{-5} mm/mm	4.44×10^{-5} mm/mm to 4.56×10^{-5} mm/mm
Strain concentration	7.22×10^{-5} mm/mm	6.44×10^{-5} mm/mm

Table 4.9: Dimensions of the examined specimens and their resulting strain

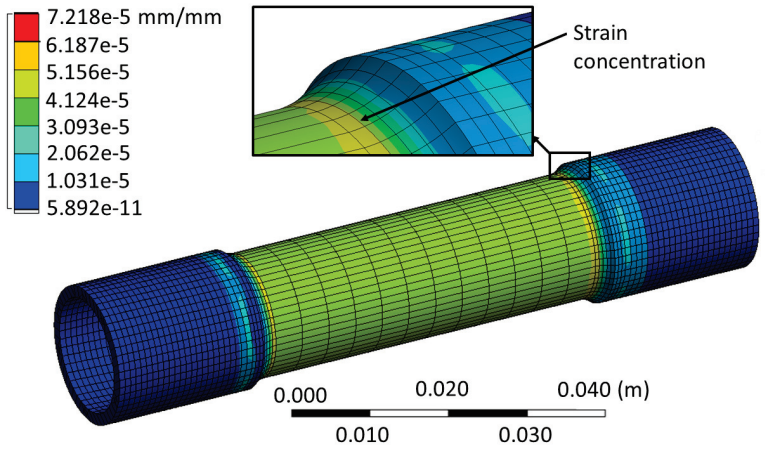

Figure 4.40: The strained specimen with a transition radius of 5 mm

was applied for the same length as mentioned above. The specimen was meshed with tetrahedra elements and the transition region was meshed finer to correctly reproduce the notch effect. The resulting strains in the specimen as mentioned above are at about 0.2 % with an excitation force of 1000 N. More important in this part of the thesis is the relation of the displacement of the masses to the strain. For this simulation it is not necessary to execute a harmonic simulation. The specimen with its fixations was loaded into ANSYS® WORKBENCH and a static displacement of

3 µm was applied onto the specimen.
Two different specimen geometries were compared as stated in table 4.9. The determining factor is the transition radius which acts as a notch and generates strain concentrations. As expected, the larger radius has a smaller strain concentration and is therefore the preferred option. Figure 4.40

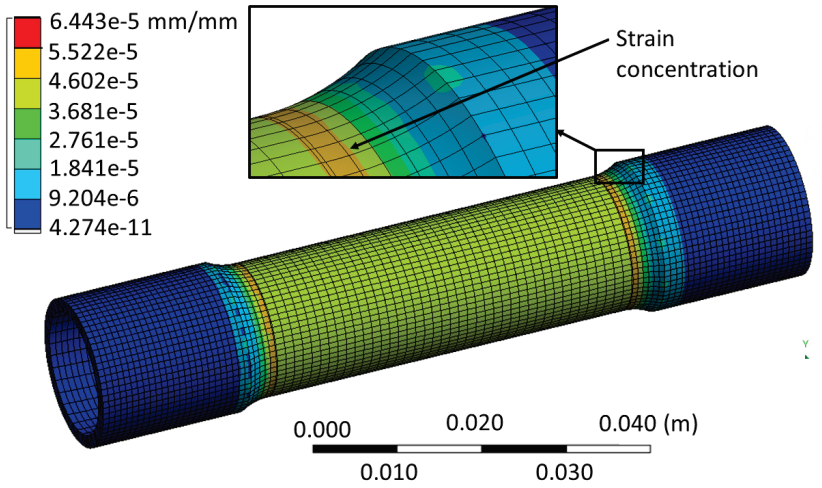

Figure 4.41: The strained specimen with a transition radius of 10 mm

shows the first specimen and the distribution of the strain. As expected, the second specimen does have smaller strain peaks at the transition region from the reinforcement to the strained section. The strain distribution on the strained length is for both specimen in an acceptable range compared to the calculated strain. The generated strain varies approximately ±10 % in close proximity to the transition area. Figure 4.41 shows the specimen with the larger transition radius. The elevated strain directly after the rigid fixation and the before the applied displacement can be ascribed to numerical effects.
Concluding it can be said that the larger transition radius is a better solution. There has to be enough space for the strengthening of the fixation area. This means the maximal radius is restricted to a reasonable value. A 10 mm radius proofed to be a good solution in the simulations. The strain concentrations in the simulation can turn out higher due to the perfectly rigid bondings. On the other hand a softer fixation can lead to a measuring error. To verify the measuring system on the test stand an additional strain gauge is recommended to compare the results of the two systems.

Chapter 5

Project Execution and Implemented Solution

In the following section the operation and functionality of the previously designed testing stand will be presented. Various problems like measurement system, closed loop control and frequency answer will be discussed. The represented testing device will be compared to the simulations and any deviations will be explained.

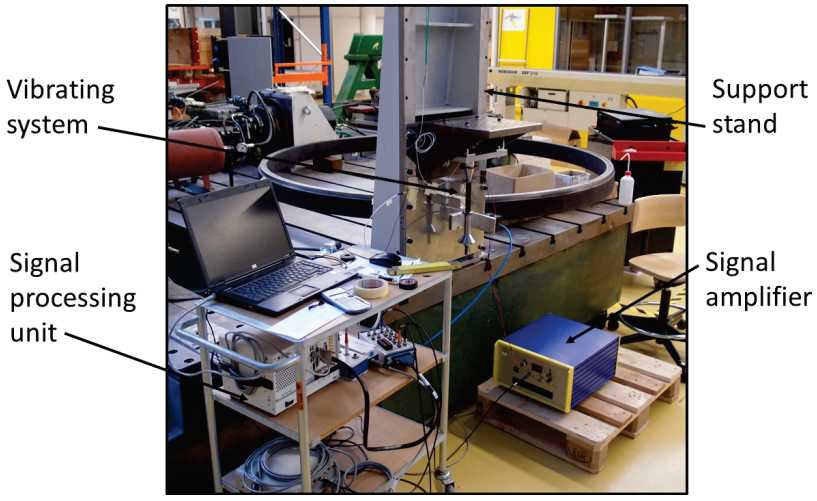

Figure 5.1: Picture of the built up test stand

5.1 Set Up of the testing device

Initially the general set up's devices which are in use, will be listed in the following. This contains the sensors including the signal processing tool, the air bushing, the specimens and the actuator. The set up of the testing device can be seen in figure 5.1.

5.1.1 Measuring System

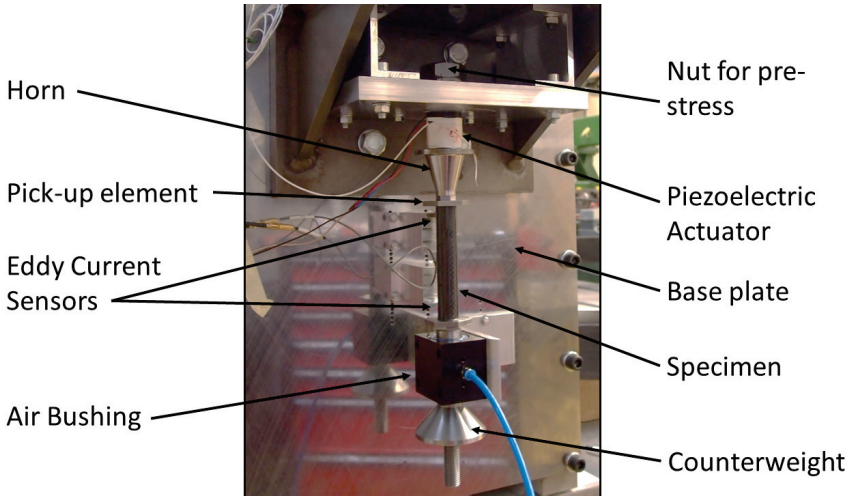

Figure 5.2: Picture of the vibrating system

The first step was to assemble the whole system as seen in figure 5.2 with the nut to secure the pre-stress only lightly tightened by hand. After mounting the horn and the actuator, both pick-up elements were fixed onto the specimen and attached to the horn on one side. Further the air bushing was mounted onto the base plate. After pressurizing the bushing with air, the counterweight was

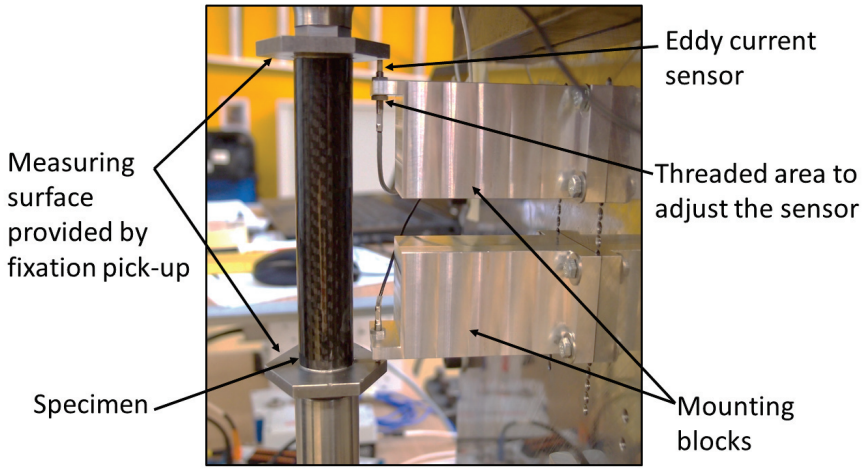

Figure 5.3: Mounting blocks for the eddy current sensors

pushed through the bushing and threaded into the other pick-up element of the specimen. The air bushing is fixed tightly just after the counterweight is attached to the system. That way the orientation of the bushing can be adjusted to guarantee a flawless operation.
Then the eddy current sensors were applied. Both alumina blocks were mounted on the plate so that an approximate distance of 10 mm between the measuring surface of the pick-up element of the moving mass and the mounting block is reached. Then the sensors are mounted on the blocks

as seen in figure 5.3 and the distance can be measured. With the information of the distance from the sensors the tips of the sensors can be adjusted to approximately 200 µm to work in their ideal working range.
With the displacement sensors setted up the pre-stress could be applied. The scope is to apply enough pre-stress so that the piezoelectric actuator is compressed by 20 µm to 30 µm and to make approximately two windings with the pre-stress nut.

5.1.2 Piezoelectric Actuator and Pre-Stress System

The chosen piezoelectric actuator is the HPST 1000/35-25/40 by PIEZOSYSTEM JENA GmbH. This actuator proofed to be sufficiently strong with a blocking force of 20 kN and a free stroke of 55 µm. The actuator was supplied with voltage by the signal amplifier PIEZOMECHANIK ® LE500/200 pointed out in figure 5.1. This generator amplifies the signal from the output of the control loop and generates a maximal voltage of 500 V which is half the maximal voltage of the actuator.
For the pre-stress system several combinations of disc springs were tested. In the end relatively

Property	Value
Outer Diameter	$d_e = 35.5\,\text{mm}$
Inner Diameter	$d_i = 18.3\,\text{mm}$
Thickness	$t = 2.0\,\text{mm}$
Height of unstressed spring	$h = 2.80\,\text{mm}$
Maximal Force	$F_{Max} = 5187\,\text{N}$
Maximal displacement	$h_0 = 0.60\,\text{mm}$
Linearity ratio h_0/t	0.3
Constant K_1	$K_{1(d_e/d_i=1.93)} = 0.69$
Stiffness according to equation (5.1)	$8331\,\text{N}\,\text{mm}^{-1}$

Table 5.1: Dimensions of the disc spring and derived properties

strong discs, packed in serial stacks were chosen to generate sufficient forces. The dimensions and derived stiffnesses are listed in table 5.1. According to the data sheet of the actuator the stiffness of the piezoelectric ceramic is approximately $500\,\text{N}\,\mu\text{m}^{-1}$. A pre-stress of approximately 20 µm results in a pre-stress force of 10 kN. The stiffness c of a disc spring can be calculated according to equation (5.1) [71].

$$c = \frac{4E}{1-\nu^2}\frac{t^3}{K_1 D_3^2} \tag{5.1}$$

In the mentioned equation E stands for the Young's modulus, ν for Poisson's ratio, t the thickness of the spring, d_e the outer diameter of the spring and K_1 is a constant depending on the diameter ratio d_e/d_i. However, this equation is only valid for disc springs with:

$$h_0/t \leq 0.4 \tag{5.2}$$

where h_0 is the maximal displacement the spring can make. For disc springs with $h_0/t > 0.4$ the non-linearly behaviour of the stiffness contributes too much to assume a linear spring characteristic. the spring will not behave absolutely linear so it is to consider that the spring will generally behave

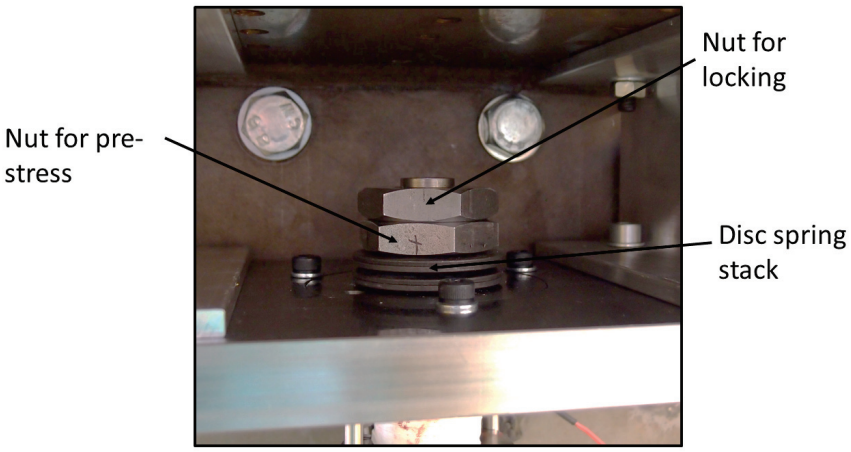

Figure 5.4: Picture of the disc spring stack

stiffer in the first part of its loading curve and will then be softer. It is important to make enough windings with the nut which secures the pre-stress system. If the nut loosens the pre-stress of the piezoelectric actuator will be gone and it can suffer serious damages.
In the end four of the described disc springs from table 5.1 were stacked serially as seen in figure 5.4. A stack of four disc springs leads to a maximal displacement of 2.4 mm. Applying two turns compresses the stack by approximately 2 mm so that enough residual space is provided for the spring stack to move.

To avoid any torsional loadings on the actuator a rotation lock of the horn, consisting of two

	Sensor horn	Sensor Counterweight
Without pre-stress	185.0 µm	226.1 µm
With pre-stress	204.9 µm	205.6 µm
Distance change	19.9 µm	20.5 µm
Applied turns	2	2

Table 5.2: Displacements due to pre-stress of the piezoelectric actuator

shoulder screws, was attached. Figure 5.5 shows the applied screws on the horn. The next step was to measure both distances between eddy current sensor and measuring surface on the pick-up element before and after applying the pre-stress. The differences in distance between the two measurements gives the pre-stress on the actuator. Both sensors shall give the same distance change. The measurements before and after applying the pre-stress are listed in table 5.2. A distance change of approximately 20 µm was reached with 2 turns of the nut which lies in the desired range. After applying successfully the pre-stress it is possible to remove the rotation lock and start with testing.

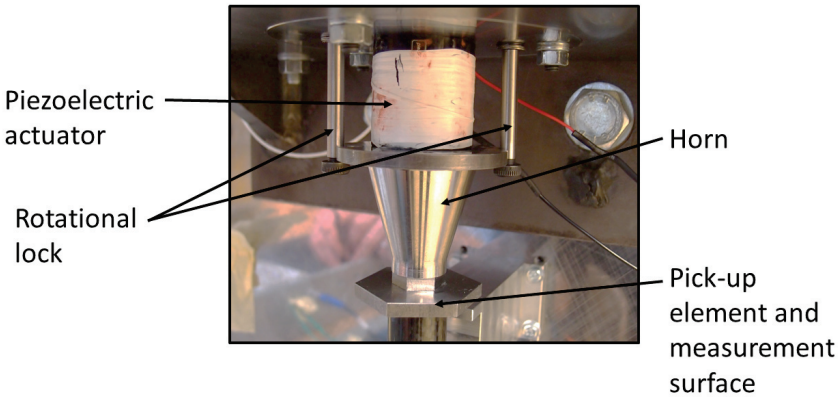

Figure 5.5: Picture of the applied rotation lock

5.1.3 Data Acquisition and Data Processing

The high testing frequency of the testing device implies a fast and accurate measuring system. For the specific prototype a real time system from National Instruments® was used. In a PXI 1031 chassis a NI 8106 real time system was fitted. Further a NI 6221 acquisition device was fitted from which a board was attached. The board has eight analogous input and two analogous output BNC channels. The whole system can be seen in figure 5.6.
The data processing was executed using Labview®. This software allows to launch a real time project and combine it with a user interface which runs on a normal hard drive. That way the data acquisition and data output was setted up. The time critical code, such as the data acquisition, the strain calculations and control loop, runs directly on the PXI hard drive so that even in case of a shut down or any other failure of the computer the control loop stays active. The right sample frequency, buffer time, deterministic loop speed and filter properties are very important to acquire a trustful and good signal.
In the beginning a simple program was developed to test the characteristics of the test stand. From the DAQ both eddy current sensors were read out and converted from voltage to associated value in µm in a deterministic real time loop with a sampling rate of 20 kHz. Both signals were overlaid with a lot of noise in high frequency range and a beat frequency with a period time of about $T_b = 0.05\,\mathrm{s}$ which results in a frequency of 20 Hz to 25 Hz as can be seen in figure 5.7. Further the noise is considerable stronger in the small amplitude section of the beat frequency. The reason for this behaviour is difficult to determine and is suggested to come from the data swap from real time system to PC which is approximately at this frequency. This would explain the stronger repetitive noise at this frequency. The same problem is encountered at the output of the real time system and may therefore induce the beat frequency. At this phase of the project a lot of monitored data is sent to the PC and saved there which costs a lot performance resources. This problem is expected to decrease sufficiently when signal monitoring is done only internally on the real time system and only strain amplitude and peak counter information is sent to the PC.
The exciting frequency at which the sample was taken, is 600 Hz. At this frequency the beat frequency is strongest and decreases afterwards again. However, it is seen at every frequency. Further the noise of the signal was filtered. The raw and the filtered signal is shown in figure 5.8 also at a

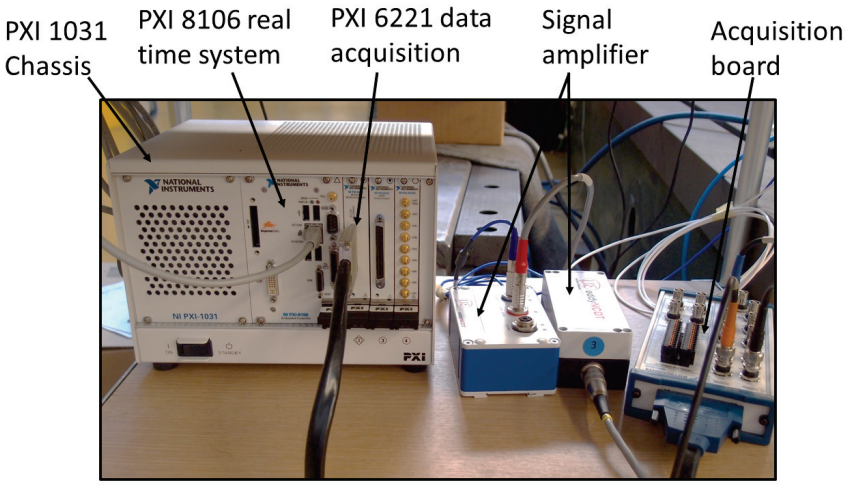

Figure 5.6: Real time PXI system from National Instruments®

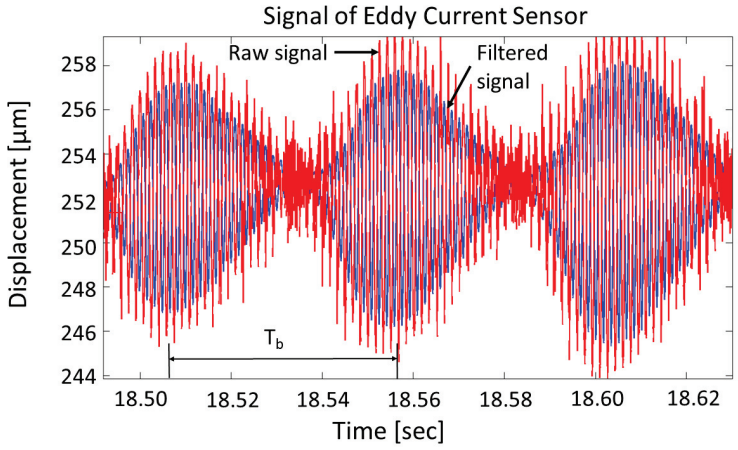

Figure 5.7: Beat frequency on the signal of the displacement sensor

frequency of 600 Hz. The period T_f is pointed out for the filtered signal. The applied filter was a Butterworth low-pass filter of 4^{th} degree with a passing frequency of 650 Hz. The passing frequency shifts upwards with increasing exciting frequency to generate a good signal at any frequency. Further the signal was subtracted by its offset value to have an oscillation around zero. Afterwards the two signals were subtracted from each other which, divided by the strained length, resulted in the effective strain in the specimen. After processing the signal the described way, a desirable curve was measured which is represented in figure 5.8. However, there is a phase shift due to the high order of the filter. It is important to treat both signals from the eddy current sensors exactly the same way to calculate the strain. The signals will be subtracted from each other which is a time critical process and has to be monitored closely. All signal processing will be executed in a deterministic loop with a iteration time of 0.5×10^{-3} sec to guarantee a flawless result. A cycle count was applied on this signal. The cycle counter counts only peaks with a certain amplitude and width to avoid counting noise peaks.
The value for the amplitude is defined by the strain which is specified by the user to be applied

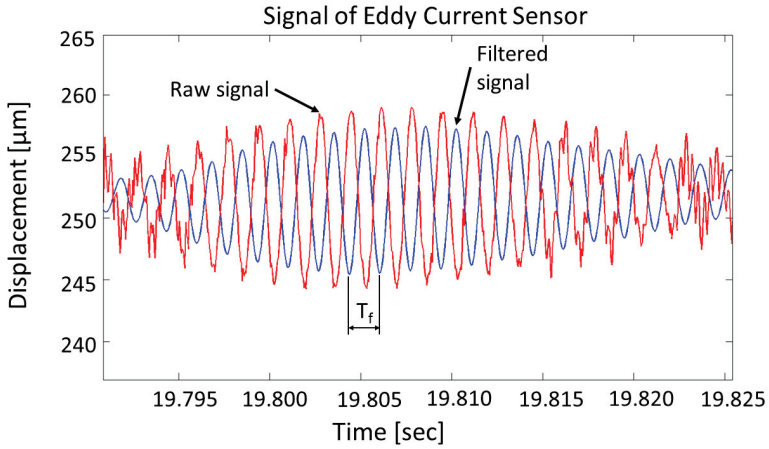

Figure 5.8: Raw and filtered signal of the eddy current sensor of the horn mass

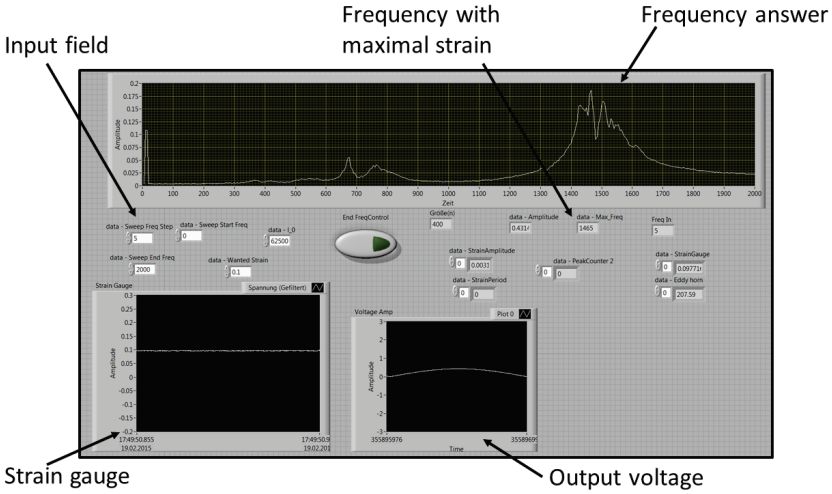

Figure 5.9: Front panel of the control program

on the specimen and the width is calculated from the frequency at which the machine runs at the time.

The front panel shown in figure 5.9 shows the outputs and inputs for the control loop. There are generally two programs, namely Frequency Control and Frequency Sweep. The Frequency Sweep program will be ran first to characterize the amplitude answer of the system. This program sweeps the frequency from a specified start frequency to an end frequency in determined steps. The data acquisition tool (DAQ) saves the strain to the associated frequency and plots the result in a graph. From this information the frequency at which the most strain is induced into the specimen can be determined. This frequency is saved and later on used for the other program Frequency Control. In the input field the required data such as strained length, end frequency, frequency step and required strain are inserted. Various outputs like strain gauge signal, strain amplitude or measured period of the signal can also be seen.

In the Frequency Control mode the program supplies the frequency, earlier derived from the Frequency Sweep program, to the actuator. With a PID control unit the amplitude of the supplying

signal is managed to keep the desired strain in the specimen. Every 60 sec the program sweeps the frequency up and down for a specified range. The according strain answers are compared to each other. Depending on which strain answer has the higher value, the control program adjusts the frequency to work always in the correct eigenvalue.

5.1.4 Specimen

The specimens for validating the testing device were dummies cut out of standard CFRP pipes. Two different pipes were provided by SUTER-KUNSTSTOFFE® AG and are specified in table 5.3. They were cut to a length of approximately 115 mm in order to smoothen both ends after the cutting. The strained length was later determined by measuring the distance between the pick-up elements and subtract the length of the pick-ups. The specific stiffnesses in table 5.3 were calculated using a length of 65 mm. The specimens' stiffnesses are given from the catalogue. However, to determine

	Pipe #1	Pipe #2
Catalogue Name	UltraSuperLite CFK Rohr	CFK-Prepregrohr
Inner Diameter	20.0 mm	20.0 mm
Outer diameter	21.0 mm	22.0 mm
Thickness	0.5 mm	1.0 mm
Young's modulus	98 GPa	100 GPa
Specific stiffness	48 396 N mm^{-1}	101 492 N mm^{-1}
Resonant frequency of analytical model	1918 Hz	2777 Hz
Resonant frequency of FE model with support	1810 Hz	2503 Hz

Table 5.3: Properties of the used specimen dummies

the actual stiffness of the specimens respectively of the system specimen and fixation, a simple tension and compression test in the ZWICK 1474 machine was executed. With this information the expected frequencies for the specific arrangements were calculated in the state space model. The results are shown in table 5.4. The specimen from pipe #2 can be seen in figure 5.10 clamped into the machine in the picture on the right side. The left hand diagram in figure 5.10 shows the force displacement relation of the specimens. The reason for this test is, in this phase only to achieve the exact stiffness of the system acting as a spring to have trustful values for comparison. The specimen was therefore only stressed in its elastic region with small forces. A maximal force of 2000 N and a maximal displacement of 0.5 mm were setted as testing parameters. The force was applied with a speed of 0.5 N/ min The clamping system from the fatigue stand was also used as an adaptor for the pulling machine. The results represented in figure 5.10 are fitted lines through averaged data sets of 10 tests for every set up. The standard deviation ranges between 0.45 % and 0.61 %. The lines were subtracted by their offset value for better comparison.
The according tests for the different wall thicknesses of the specimens are pointed out in figure 5.10. The resulting stiffnesses are all far below the expected values. With the slope of these lines it is possible to calculate the stiffness and according frequencies as listed in table 5.4. The derived values like Young's modulus and resonant frequencies are calculated with the tensional stiffness. These

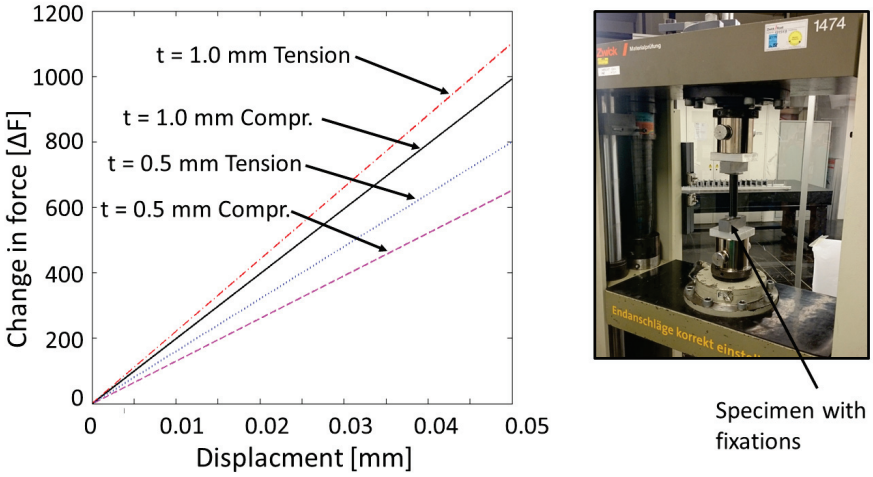

Figure 5.10: Picture of the clamped specimen and resulting force stroke curve

unexpected results showed the importance of this test. The stiffnesses are far below the initially assumed values which means that also the resonant frequencies are much lower. This deviation could be derived from a too weak fixation. This would mean that the specimen is hardly strained but the frictional forces between fixation and specimen are measured. However, the compression tests showed similar stiffnesses. Although the compression stiffness is expected to be lower but no reference values are available. Due to thinner wall thickness the clamping of the second specimen

	Specimen from pipe #1 ($t = 0.5\,\mathrm{mm}$)	Specimen from pipe #2 ($t = 1.0\,\mathrm{mm}$)
Length	64.9 mm	64.5 mm
Measured specific stiffness tension	$16\,005\,\mathrm{N\,mm^{-1}}$	$22\,030\,\mathrm{N\,mm^{-1}}$
Measured specific stiffness compression	$13\,038\,\mathrm{N\,mm^{-1}}$	$19\,845\,\mathrm{N\,mm^{-1}}$
Young's modulus	32.4 GPa	21.5 GPa
Resonant frequency of analytical model	1102 Hz	1293 Hz

Table 5.4: Results of tension and compression tests

had to be executed less tightened which would then also explain the slightly lower stiffness of the second specimen. However, at this point it can not totally be excluded that the material properties of the CFRP pipes are far below the expected value. For a better clarification of this issue it would be necessary to apply strain gauges on the specimens to measure the exact strain of the specimen. However, the result of this test is the effective spring stiffness of the system which determines the resonant frequencies.

5.1.5 Strain Gauge Measurement

For reasons mentioned above the measuring system with two eddy current sensors had to be verified. To measure accurately strain on the specimen, a strain gauge was found to be the best solution. The strain gauge applied was the LY 11-6/120A from HBM® AG. The strain gauges were operated in a two-quarter-bridge with compensation strain gauges in order to compensate temperature variation. The operated bridge can be seen in figure 5.11 where R_1 and R_3 are the active strain gauges (SG) and R_2 and R_4 are the compensation strain gauges (Comp. SG). The bridge is fed by the voltage U_E whereas U_A is the measured voltage.
The compensation strain gauge must suffer the same temperature development as the measuring strain gauge but should not suffer any mechanical loading. Such a place is hard to find. The compensation strain gauges were applied on the CFRP specimen on the height of the pick-up elements where no strain is induced. This should reduce the measuring error to a minimum. The temperature compensation is calculated with formula (5.3) where the respective ε represent the mechanical strain and thermal strain of the according strain gauge and ε_a is the finally measured strain. The effective strain ε_l is stated in equation 5.4. Further it is suggested that all strain gauges are from the same package or the same manufacturing lot so that they behave as similar as possible.

$$\varepsilon_a = (\varepsilon_{mec1} + \varepsilon_{therm1}) - (\varepsilon_{therm2}) + (\varepsilon_{mec3} + \varepsilon_{therm3}) - (\varepsilon_{therm4}) \tag{5.3}$$

$$\varepsilon_l = \frac{\varepsilon_a}{2} \tag{5.4}$$

Finally this means two strain gauges are applied onto the specimen and two strain gauges were

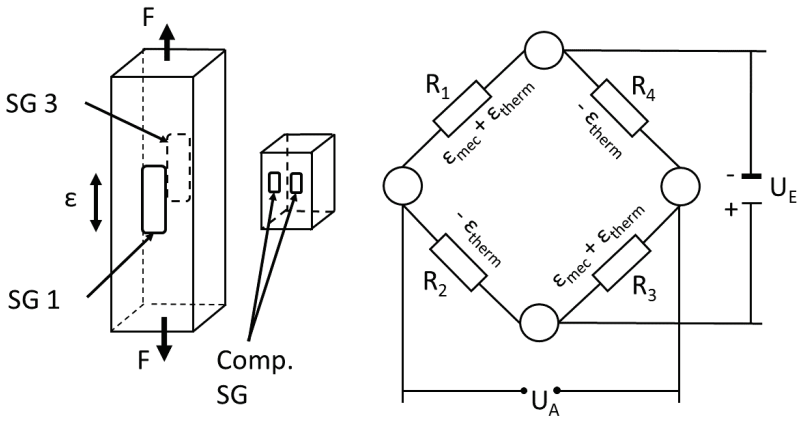

Figure 5.11: Operational circuit of the strain gauge measurement

operated as compensation strain gauges applied on the area of the pick-up elements [72]. In 5.12 the applied strain gauges on the specimen can be seen. The specimens used were cut from pipe #2 and had a operational length of 62.5 mm.
Applying strain gauges is a delicate issue in order to obtain trustful results. To compensate any additional error on the signal it is advised that all cable lengths connected to the strain gauges have the same length. Errors from cable resistances subsequently compensate themselves. The strain gauges were fed by the measurement amplifier AE 101 also from HBM® AG.
The next step was to calculate the scaling factor to receive the resulting strain on the specimen.

The measurement amplifier has a voltage range of 10 V. The feeding voltage U_E, the k-factor for all operated resistances in the bridge are stated in table 5.5. The measurement amplifier was further adjusted to achieve a good resolution and reset the zero volt signal in the required operating range. The amplification factor a is also stated in equation 5.5. With this information the output voltage is scaled to the desired strain signal with the formula for ε_a stated in equation (5.5) which is the measured strain.

Feeding voltage U_E	2.5 V
K-factor k	2.06
Amplification factor a	8.1

Table 5.5: Properties of the strain gauges and the Wheatstone bridge

$$\varepsilon_a = \frac{4\,U_A}{8.01\,k\,U_E} = 0.097\,U_A \tag{5.5}$$

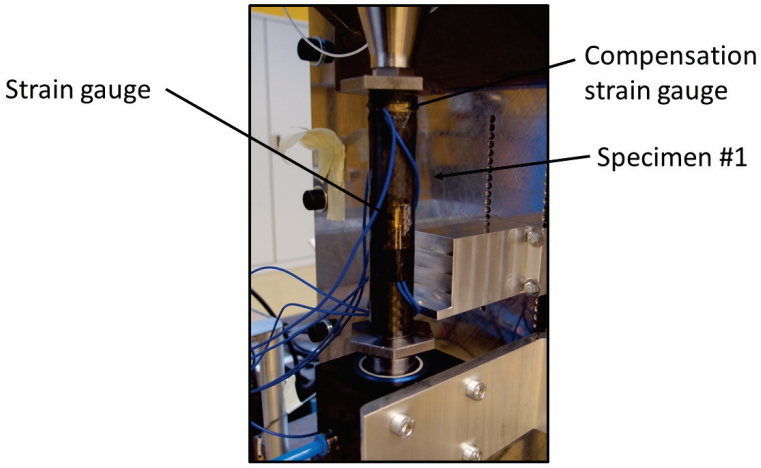

Figure 5.12: Specimen with applied strain gauges

5.2 Measurements and Results

In this section the measured results are represented and discussed. All data was saved from the LabVIEW® tool for further handling in MATLAB®.

5.2.1 Strain Answer on the Frequency

After adjusting all time critical signal acquiring issues to achieve a good signal the above mentioned frequency sweep was executed. The control program increases thereby the exciting frequency step by step with the same voltage amplitude and the according strain answer was saved to file. Before

starting the program, the frequency amplifier for the piezoelectric actuator was set to an offset of 250 V which strained the spring stack for 12.3 µm. The amplitude fed into the frequency amplifier was 0.5 V which results in a voltage amplitude for the actuator of 50 V. A 5 Hz frequency step every 0.1 sec proofed to be a good value and an end frequency of 2000 Hz was chosen. According to the simulations with the ideal stiffnesses higher frequencies are expected, however the strain gauges meet their limits at 14 000 Hz bandwidth and any higher frequencies are critical to acquire with these. Additionally the effective spring stiffnesses are lower and so are the expected frequencies. Nevertheless the specimens were excited up to 4000 Hz but no peak was detected once 2000 Hz were exceeded neither with strain gauges nor with the eddy current sensors. Two specimens from the pipe #2 were applied and tested with this frequency sweep with respective strained lengths of 62.5 mm and 64.0 mm. The diagram shown in figure 5.13 shows the resulting answer for the two

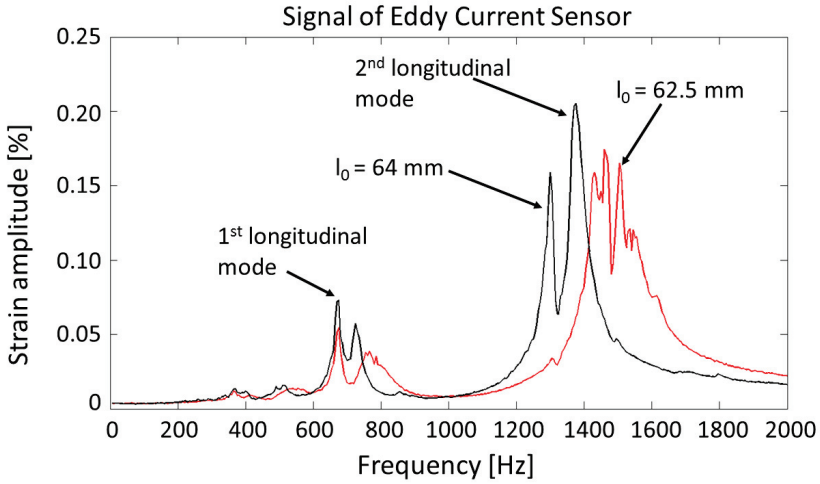

Figure 5.13: The answer in strain amplitude on excitement for various frequencies

specimens. The two different lengths are pointed out. As can be seen, the first detected longitudinal eigenmode was for both specimen at about 650 Hz and results in a strain amplitude of 0.06 % and 0.08 %. The way more interesting peak was found at 1465 Hz with a maximal strain amplitude of 0.17 % and for the shorter specimen at 1395 Hz with a strain of almost 0.22 %. This is the respective frequency which is saved internally and is the initial working frequency for the testing. Further it can be seen that a sufficient amplification is already achieved with small voltage amplitudes. After every strain peak there is a sudden decrease of strain. This may not be mistaken as an anti resonance but is derived from the beat frequency. The difference in the resonant frequencies can partially be ascribed to the length of the specimen and so are the higher strains since the specific stiffness decreases with a longer strained length. Another explanation would be a moving fixation with different acting friction forces.
For statistical reasons the diagram shown in figure 5.13 were executed five times and the arithmetic mean value was built. All data sets showed hardly any deviation for every test.
The frequency plot has similarities to the expected answer received from the simulation in chapter 4.3.3 but is obviously not the same. Observing the shorter specimen there are essentially two peaks at 650 Hz and 1495 Hz. The second of them with the desired phase shift to induce sufficient strains into the specimen. Compared to the calculated resonant frequency for these specimen the deviation is 7.3 % and 13.5 % and lies in the expected range. The high detected strains are further a sign of a stiff fixation but low material properties. A large problem which was also encountered was a

considerable vibration of the support structure. Especially the plate where the horn is mounted to, vibrates strongly at the first longitudinal mode and so does the support bracket. With higher frequencies the vibration fades but does not disappear completely so that a noticeable influence on the frequency behaviour has to be considered. It is therefore strongly suggested to mount the vibrating test system onto a more suitable support structure such as a mineral cast or the like.
A test with a specimen from pipe #1 showed similar results but without sudden amplitude decrease after peaks. The resonant frequency lies between 1070 Hz and 1075 Hz which deviates 2.5 % to 2.9 % to the analytical model.
The influence of the vibrating support is also seen as a large problem especially for stiffer arrangements were higher forces and frequencies are acting. Another issue is the stiffness of the spring disc stack which is only analytically approximated. For exacter results and predictions, it is suggested to generate the characteristic spring diagram of the stack experimentally.

5.2.2 Strain During Testing

Knowing the specific frequency answer for the system, first test cycles were started, monitored and saved to file. Testing with such frequencies and recording the data set costs a lot of resources of the computer and the program has to be designed in order to act as fast as possible. However, saving data to file is still a problem and it is difficult to achieve desired datasets. The signal is acquired with 20 kHz which leads to large amounts of data in a short time.
As mentioned, the frequency with the maximal strain amplitude was saved and the program au-

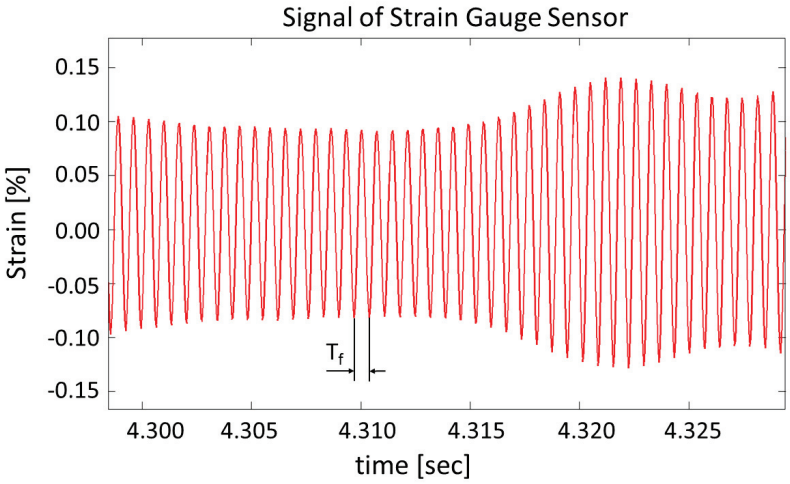

Figure 5.14: Signal of the strain gauge at 1495 Hz

tomatically increased the exciting frequency until the desired frequency is reached. This process is executed with a initial voltage amplitude of 50 V. Once the frequency is reached the program swaps to a PID controller which adjusts the voltage amplitude to generate the predetermined strain. Figure 5.14 shows the strain development at a frequency of 1465 Hz. The pointed out period is approximately $T_f = 0.7 \times 10^{-3}$ sec. The strain amplitude is set to be 0.1 %. There is a slight buckle of the strain amplitude which comes from the slowly working PID controller when data are logged to file. The required voltage amplitude for piezoelectric actuator was in this case approximately 42 V.

As can be seen from this test, the actuator is working well within its operational limits and induces a sufficient strain into the specimen. However, the achieved frequencies lie below the required values which is ascribed to the much lower effective stiffness of specimen or fixation. Another explanation is the strongly vibrating support stand. For reaching the initially expected frequencies it is necessary to guarantee a sufficiently stiff fixation of the specimen and trustful reference values for the stiffness. Further it is advised to mount the testing stand on a stiffer or much heavier structure.
In summary the experiments showed promising results regarding high frequency and induced strain. However, the measuring system has to be reconsidered and adjusted very well to receive representable results. The strain gauges on the other hand delivered good results but are restricted in their life and their band width but are a good compromise to calibrate the indirect measuring technique.

Chapter 6

Conclusion

In summary it can be said that the development and application of a high frequency testing device is a complex issue. The biggest problems are to find an actuator which can work highly dynamically and has enough power to generate the required stresses and to apply a fast an accurate measuring system. The test facility should be simple, both in structure and in handling. A piezoelectric actuator was chosen to be the best choice to fulfil these requirements. It is important to apply a sufficiently powerful piezoelectric element and to work only within a fracture of its nominal power. That way an early breakage of the actuator, due to fatigue, can be avoided.
Testing with high frequencies is not only a challenge for the test facility but also for the material. Metallic materials do not show a strain rate dependency over wide ranges and can therefore be mounted in high frequency test machines without further concerns. However, FRPs have a more complex behaviour. Their damage mechanisms and their fatigue life depend on various factors.
The occurring loadings in the regarding component of the machine were closely examined. The main problem for estimating stresses of stamping machines is the non-existing information about the occurring stresses or forces. The forces, the ram has to withstand, were estimated from a qualitative force-stroke development and the nominal force of the machine. This loading was then applied on the existing cast iron ram. Since the new CFRP ram can only globally reproduce the exact same properties in stiffness and strength, this approach has to be seen as a suggestion to design the testing signal and has to be repeated once the design of the FRP ram is known.
With this information a load signal for the testing machine was estimated. A sinusoidal loading with a frequency of approximately 2000 Hz proofed to be a good representative of the actual load. Hence the resonant testing facility was developed which should work within that frequency range. There are several problems which occur with resonant test facilities. Especially for CFRP, where the stiffness of the material systems can vary significantly. The actual testing frequency can vary and a comparison of two different materials will be difficult. The test stand was designed to attach additional weights so that a similar frequency can be found for every material system.
A suitable shape of the specimen was found to be a pipe. Several properties like heat transfer, buckling or fibre scatter generally had a better behaviour with a pipe shaped specimen compared to the standard coupon fatigue specimen. Varying the wall thickness and the strained length of the specimen is an easy option to adjust parameters like natural frequency, heat transfer or achievable strain.
Heating of the specimen is another problem which occurs with high frequency testing of high damped materials like FRPs. FEM simulations were executed with different specimen geometries and it was found that a cooling system is indispensable. To avoid critical heating, two actions

were taken: The test stand was designed with a bore through the entire length in order to press a cooling fluid through it and cool the specimen from the inside. The specimen should also have small wall thicknesses to transfer heat efficiently to the surfaces.
The dimensioning of the test stand was approached first with a mathematical model which represents an excited two-mass system in MATLAB. A parameter study was executed which leads to the conclusion that the excited mass should be small, whereas the counterweight could be heavier to generate sufficient strains. This model was then recreated using a FE analysis which showed similar results. However, to simulate the whole excited test stand is a difficult issue. It is most important to choose the correct boundary conditions and to recreate an exact model of the real life event. Harmonic simulation showed that with a very stiff connection of moving system and support, the support will suffer significant stresses and may start to vibrate. The connection and pre-charging of the piezoelectric element has to be implemented with an elastic element like a disk spring. The support of the test stand should additionally be dimensioned as stiff as possible. That way the two-mass oscillator vibrates in the required frequency ranges and induces all strain energy into the specimen.

Finally the designed testing device was assembled and tested on its functionality. As a measuring system two eddy current sensors were applied which should measure the strain indirectly. However, there were several issues encountered with these sensors as their signal had a lot of noise and they are very fragile. A strain gauge was then applied on the specimen which delivered promising results but still with repetitive noise. For controlling and data acquisition a real time system was used which is able to measure and handle the data fast enough. However, the data saving costs lots of performance resources and the data saving could only be applied in short time frames in order to keep the amount of data in acceptable limits. Further a frequency sweep was executed to analyse the strain answer on the frequency. First tests showed that above 2000 Hz no significant resonant frequencies were found despite the initially expected frequencies were around 2300 Hz. A tension test of the specimen including the fixation showed a much lower stiffness of the specimens than assumed. This could be ascribed to loose fixations but several facts like high induced strain and repeatability for other specimen indicate an inferior material. The highest resonant frequency was found at 1465 Hz and induced sufficient strains into the specimen. A big issue which appeared during testing is the vibration of the support structure. This problem has to be solved using a stiffer or much heavier support unit. Initial tests showed a sufficient induced strain into the specimen, however the system was overlaid with a strong beat frequency which can be ascribed to either a structural problem or a software problem and has to be observed very closely. Most of the beat frequency could be balanced with a PID controller.
The testing machine showed promising results but there are several issues which must be encountered more closely like the specimen fixation and a more stable support stand. However the tests so far showed that the testing principle works well and can be used as a fast and appropriate way to test the VHCF region of CFRP.

List of Figures

Bibliography

[1] M. Orth, M. Butz, and C. Gaier. "Entwicklung einer Methode zur Betriebsfestigkeitsanalyse von Strukturbauteilen aus CFK unter Zuhilfenahme verschiedener statischer Versagenskriterien". In: *40. Tagung des DVM-Arbeitskreises Betriebsfestigkeit* (2013).

[2] Bryan Harris. *Fatigue in Composites*. Woodhead Publishing Limited, 2003. ISBN: 0-8493-1767-3.

[3] Silvain A. Michel, Rolf Kieselbach, and Hans Jörg Martens. "Fatigue strength of carbon fibre composites up to the gigacycle regime (gigacycle-composites)". In: *International Journal of Fatigue* (2006).

[4] Theodore Nicholas. *High cycle fatigue a mechanics of materials perspective*. Amsterdam: Elsevier, 2006, 641 S. ISBN: 0-08-044691-4 978-0-08-044691-2.

[5] Anastosias P. Vassilopoulos and Thomas Keller. *Fatigue of Fiber-reinforced Composites*. Springer, 2011. ISBN: 978-1-84996-180-6.

[6] Nadim Ganam. *Auswirkungen des Herstellungsprozesses auf die Ermüdungseigenschaften von Kohlenstoffendlosfaserverbunden für den Stanzautomatenbau*. 2014.

[7] E.K. Gamstedt and R. Talreja. "Fatigue damage mechanisms in unidirectional carbon-fibre-reinforced plastics". In: *Journal of Materials Science* (1999).

[8] W.J. Cantwell and J.Morton. "The Impact resistance of composite materials - a review". In: *Composites* (1991).

[9] Joachim Rösler, Harald Harders, and Matrin Bäker. *Mechanisches Verhalten der Werkstoffe*. Vol. 4. Auflage. Springer Vieweg, 2012. ISBN: 978-3-8348-1818-8.

[10] Manfred Flemming and Siegfried Roth. *Faserverbundbauweisen Eigenschaften mechanische, konstruktive thermische, elektrische, ökologische, wirtschaftliche Aspekte*. Berlin: Springer, 2003, 615 S. ISBN: 3-540-00636-2.

[11] S. T. S. Al-Hassani and A.S. Kaddour. "Strain Rate Effects on GRP, KRP and CFRP Composite Laminates". In: *Key Engineering Materials* (1998).

[12] Jacob Aboudi. *Mechanics of Composite Materials*. Studies in Applied Mechanics. Elsevier, 1991. ISBN: 0-444-88452-1.

[13] Gregoire Lepoittevin. "Composite Laminates with Integrated Vibration Damping Treatments". Thesis. 2012.

[14] W. Stark. "Investigation of the curing behaviour of carbon fibre epoxy prepreg by Dynamic Mechanical Analysis DMA". In: *Polymer Testing* 32 (2012).

[15] Atsushi Hosoi, Yoshihiko Arao, and Hirokazu Karasawa. "High cycle fatigue characteristics of quasi isotropic CFRP laminates". In: *Advanced Composite Materials* 16 (2012).

[16] Ahid D. Nashif, David I. G. Jones, and John P. Henderson. *Vibration Damping*. New York: Wiley and Sons, 1985. ISBN: 978-0-471-86772-2.

[17] R. Chandra, S. P. Singh, and K. Gupta. "Damping Studies in fiber-reinforced composites - a review". In: (1999).

[18] Sondipon Adhikari. *Structural Dynamic Analysis with Generalized Damping Models*. Wiley, 2014. ISBN: 978-1-84821-670-9.

[19] R.D. Adams and D.G.C. Bacon. "Effect of Fibre Orientation and Laminate Geometry on the Dynamic Properties of CFRP". In: *Journal of Composite Materials* 7 (1973).

[20] R. D. Adams and M. R. Maheri. "Dynamic Flexural Properties of Anisotropic Fibrous Compoiste Beams". In: *Composite Science and Technology* 50 (1993).

[21] R. G. Ni, D. X. Lin, and R. D. Adams. "The dynamic properties of carbon glass fiber sandwich-laminated composites: theoretical, experimental and economic considerations". In: *Journal of Composites* 15 (1984).

[22] R.G. Ni and R.D. Adams. "The Damping and Dynamic Moduli of Symmetric Laminated Composite Beams - Theoretical and Experimental Results". In: *Journal of Composite Materials* 18 (1994).

[23] D.X. Lin, R.G. Ni, and R.D. Adams. "Prediction and Measurement of the Vibrational Damping Parameters of Carbon and Glass Fibre-Reinforced Plastics Plates". In: *Journal of Composite Materials* 18 (1984).

[24] Sondipon Adhikari. *Structural Dynamic Analysis with Generalized Damping Models: Analysis*. 2014. ISBN: 978-1-84821-521-4.

[25] Paul A. Tipler and Gene Mosca. *Physik für Wissenschaft und Ingenieure*. Heidelberg: Spektrum Akademischer Verlag, 2009. ISBN: 978-3-8274-1945-3.

[26] David I. G. Jones. *Handbook of Viscoelastic Vibration Damping*. Wiley and Sons, 2001. ISBN: 0 471 49248 5.

[27] Monica Carfagni, Edoardo Lenzi, and Marco Pierini. *The Loss Factor as a Measure of Mechanical Damping*. Conference Paper. 1998.

[28] Deborah Chung. *Carbon Fiber Composites*. Butterworth-Heinemann, 1994. ISBN: 978 008 0500 737.

[29] Z. Zhang and G. Hartwig. "Low-temperature viscoelastic behavior of unidirectional carbon composites". In: *Cryogenics* 38 (1997).

[30] B.S. Ben, B.A. Ben, and K. Adarsh. *Damping measurement in composite materials using combined finite element and frequency response method*. Conference Paper. 2013.

[31] ASTM D3039/D3039M. "Standard Test Method for Tensile Properties of Polymer Matrix Composite Materials". In: West Conshohocken, PA: ASTM International, 2014.

[32] Jose Daniel D. Melo and Donald W. Radford. "Time and Temperature Dependence of the Viscoelastic Properties of CFRP by Dynamic Mechanical Analysis". In: *Composite Structures* 70 (2004).

[33] Till Julian Adam, Peter Horst, and Paul Lorsch. "Experimental Investigation of VHCF of Polymer Composites: Two Alternative Approaches". In: *Materials Testing* (2012).

[34] Hajime Kishi, Manabu Kuwata, and Satoshi Matsuda. "Damping Properties of Thermoplastic Elastome Interleaved Carbon Fiber-Reinforced Epoxy Composites". In: *Composite Science and Technology* 64 (2004).

[35] Tim A. Osswald and Georg Menges. *Material science of polymers for engineers*. 3rd. Munich: Hanser Publishers, 2012, 595 S. ISBN: 978-1-56990-524-1.

[36] M.-H.R. Jen and C.H. Lee. "Strength and life in thermoplastic composite laminates under static and fatigue loads. Part I: Experimental". In: *International Journal of Fatigue* (1998).

[37] Ramesh Talreja and Chandra Veer Singh. *Damage and Failure of Composite Materials*. Cambridge University Press, 2012. ISBN: 978-0-521-81942-8.

[38] A.Puck and H.Schürmann. "Failure Analysis of FRP Laminates by Means of Physically Based Phenomenological Models". In: *Composite Science and Technology* 58 (1998).

[39] Imad A. Al-Hmouz. "The Effect of Loading Frequency and Loading Level on the Fatgiue Behavior of Angle-Ply Carbon/PEEK Thermoplastic Composites". Thesis. Concordia University Montreal, 1997.

[40] Tamer Sinmazcelik, A. Armagan Arici, and Volkan Günay. "Impact-fatigue behaviour of unidirectional carbon fibre reinforced polyetherimide (PEI) composites". In: *J Mater Sci* 41 (2005).

[41] P. Raju Mantena, Richa Mann, and Chandrasekhar Nori. "Low-Velocity Impact Response and Dynamic Characteristics of Glass-Resin Composites". In: *Journal of Reinforced Plastics and Composites* (2001).

[42] Donald C. Hylton. *Understanding Plastics Testing*. Carl Hanser Verlag, 2004. ISBN: 1-56990-366-2.

[43] J.P. Casas-Rodrigez, I.A. Ashcroft, and V.V. Silberschmidt. "Damage in adhesively bonded CFRP joints: Sinusoidal and impact-fatigue". In: *Composites Science and Technology* (2008).

[44] R.O. Ochola, K. Marcus, and G.N. Nurick. "Mechanical behaviour of glass and carbon fibre reinforced composites at varying strain rates". In: *Composite Structures* (2003).

[45] M.V. Hosur, J. Alexander, and U.K. Vaidya. "High strain rate compression response of carbon/epoxy laminate composites". In: *Composite Structures* (2001).

[46] Amos Gilat, Robert K. Goldberg, and Gary D. Roberts. "Experimental study of strain-rate-dependent behavior of carbon/epoxy composite". In: *Composite Science and Technology* (2002).

[47] ISO 13003:2003. "Fibre-reinforced plastics - Determination of fatigue properties under cyclic loading conditions". In: Geneva, CH: ISO, 2003.

[48] D. Backe, T.B. Helfen, and U. Rabe. *Ultrasonic Fatigue Testing Combined with Online Nondestructive Testing for Carbon Fiber Reinforced Composites*. USA: John Wiley & Sons, 2012, p.855–p.862. ISBN: 9781118357002.

[49] M.Gude, W.Hufenbach, and I.Koch. "Fatigue testing of carbon fibre reinforced polymers under VHCF loading". In: *Materials Science Engineering* (2013).

[50] Jill M. Morgan and Walter W. Milligan. "A 1 kHz Servohydraulic Fatigue Testing System". In: *High Cycle Fatigue of Structural Materials* (1997).

[51] Stefanie Stanzl-Tschegg. "Very high cycle fatigue measuring techniques". In: *International Journal of Fatigue* (2012).

[52] Claude Bathias and Paul C. Paris. *Gigacycle Fatigue in Mechanical Practice*. Dekker, 2005. ISBN: 0-8247-2313-9.

[53] Claude Bathias. "Piezoelectric fatigue testing machines and devices". In: *International Journal of Fatigue* (2006).

[54] C. Fischer, R. Wagner, and A. Friedmann. "Piezoelectric Driven Testing Facilities to Research the Very High Cycle Fatigue Regime". In: *Materials Testing* (2012).

[55] Noliac® A/S 2011. Web Page. 2014. URL: `www.noliac.com/Default.aspx?ID=679`.

[56] Piezomechanik® GmbH. *Einstieg in die Piezoaktorik*. Catalog. 2010.

[57] Yung-Li Lee. *Fatigue testing and analysis (theory and practice)*. Amsterdam: Elsevier, 2005. ISBN: 0-7506-7719-8.

[58] Horst Czichos, Tetsuya Saito, and Leslie Smith. *Springer Handbook of Materials Measurement Methods*. Springer, 2006. ISBN: 978-3-540-20785-6.

[59] Gang Tao and Zihui Xia. "A non-contact real-time strain measurement and control system for multiaxial cyclic/fatigue tests of polymer materials by digital image correlation method". In: *Polymer Testing* 24 (2005).

[60] Stefan Heinz, Frank Balle, and Stefan König. *Bringing Ultrasonic Fatigue to Light*. Electronic Article. 2011.

[61] Bruderer® AG. *Technical Report*. 2014.

[62] Thomas Portmann. *Vorrichtung für den Massenausgleich bei mittels Kurbeltrieb angetriebenen Maschinen*. Vol. DE2534626 A1. DE19752534626. 1976.

[63] Waldemar Hellwig and Matthias Kolbe. *Spanlose Fertigung Stanzen*. 10th ed. Springer Vieweg, 2012. ISBN: 978-3-8348-1802-7.

[64] ASTM D3410/D3410M-03. "Standard Test Method for Compressive Properties of Polymer Matrix Composite Materials with Unsupported Gage Section by Shear Loading". In: West Conshohocken, PA: ASTM International, 2003.

[65] M. Freitas, L. Reis, and V. Anes. "Design and Assembly of an Ultrasonic Fatigue Testing Machine". In: *Anales de Mecanica de la Fractura* 1 (2011).

[66] Verein Deutscher Ingenieure. *VDI Wärmeatlas*. 40468 Düsseldorf: VDI e.V., 2013. ISBN: 978-3-642-19980-6.

[67] Anton Schweizer. Web Page. 2014. URL: `http://www.schweizer-fn.de/`.

[68] Inc. © 1994-2014 The MathWorks. Web Page. 14.11.2014. URL: http://ch.mathworks.com/help/ident/ug/what-are-state-space-models.html.

[69] Wikibooks. Web Page. 2014. URL: http://en.wikibooks.org/wiki/Control_Systems/State-Space_Equations.

[70] Herbert Wittel et al. *Roloff/Matek Maschinenelemente*. Berlin: Springer Viehweg, 2013. ISBN: 978-3-658-02327-0.

[71] W. Beitz and K.-H. Küttner. *DUBBEL Taschenbuch für den Maschinenbau*. Berlin: Springer, 1995. ISBN: 3-540-52381-2.

[72] Karl Hoffmann. *Eine Einfürung in die Technik des Messens mit Dehnungsmessstreifen*. Darmstadt: Hottinger Baldwin Messtechnik AG, 1987.